ABSTRACT

SYSTEMS SCIENCE

EPHRAIM, DANIEL E. M.S. GEORGIA INSTITUTE TECHNOGOLY, 1994

B.ME. GEORGIA INSTITUTE OF TECHNOLOGY, 1990

M.S. ATLANTA UNIVERSITY, 1987

B.S. MOREHOUSE COLLEGE, 1985

MODELING ELECTRODEPOSITED $Ni_{80}Fe_{20}$ AND THE ELECTROLYTES BOUNDARY CONDITIONS' INFLUENCE ON THE MECHANICAL PROPERTIES

Advisor: Dr. David R. Veazie

Dissertation date: May 2009

A Micro-electro-mechanical system (MEMS) gas turbine generator is currently under development. This device uses electrodeposited $Ni_{80}Fe_{20}$ (thin film) as a structural material in the high speed rotating micro-generator used to convert mechanical energy to electrical energy. For structural applications, the materials' mechanical properties are vital for the design. However, for electrodeposited $Ni_{80}Fe_{20}$, currently, there is not any published data regarding its mechanical properties.

Therefore, the goal of this research is to model the mechanical properties of electrodeposited $Ni_{80}Fe_{20}$ as a function of three critical electrolytes variables: agitation, current density, and temperature. In achieving this goal, a typical off-the-shelf nickel iron electroplating solution was used to fabricate the $Ni_{80}Fe_{20}$ test

specimens. A 2^k Factorial Analysis and Design of Experiments was used to identify the critical variables and boundary conditions, and a new Micro/Nano Testing System was designed and developed to measure the mechanical properties.

Finally, a linear regression analysis was conducted to model Young's Modulus and Ultimate Strength as a function of the three critical electrolytes variables.

MODELING ELECTRODEPOSITED $Ni_{80}Fe_{20}$ AND THE ELECTROLYTES BOUNDARY CONDITIONS' INFLUENCE ON THE MECHANICAL PROPERTIES

A DISSERTATION

SUBMITTED TO THE FACULTY OF CLARK ATLANTA UNIVERSITY

IN PARTIAL FULFILLMENT OF THE REQUIREMENTS FOR

THE DEGREE OF DOCTOR OF PHILOSOPHY

BY

DANIEL E. EPHRAIM

DEPARTMENT OF ENGINEERING

ATLANTA, GEORGIA

MAY, 2009

ACKNOWLEDGEMENTS

This research was made possible by the support from the High Performance Polymers and Composite (HiPPAC) Center at Clark Atlanta University, Army Research Laboratory (ARL), and the Collaborative Technology Alliance (CTA). I would like to thank Dr. Eric Mintz for his support; Brian Shonkwiler, Keithan Hillman, and Dr. Yeun-Ho Joung for their support and assistance. I would like to thank my committee members: Dr. Peter Molnar, Dr. Conrad Ingram, Dr. Lebone Moetie, and Dr. Duane Cooper for their support, advice and encouragement. I would like to express my gratitude and thank you to my advisor, Dr. David Veazie without whom none of this would have been possible. Dr. Veazie provided invaluable assistance with every step of this process. Again, thank you Dr. Veazie. Finally, I would be remised, if I did not mention my family. My wife, Frances and daughters: Amari Danika Ephraim, and Amber Daniece Ephraim, for being there and providing me ongoing support and encouragement to continue.

TABLE OF CONTENTS

ACKNOWLEDGEMENTS ii

TABLE OF CONTENTS iii

LIST OF FIGURES vi

LIST OF TABLES xv

1 Introduction 1

1.1 MEMS Gas Turbine Engine 2

1.2 Accomplishments 3

1.3 Project Leaders 4

1.4 MEMS Magnetic Generator 7

1.5 Accomplishments 7

1.6 Project Leaders 11

1.7 Electrodeposited Nickel Iron 11

2 Literature Review 16

2.1 Electrodeposition 16

2.2 Electroplated NiFe 17

2.3 Material Properties: Bulk versus Electroplated 19

2.4 Current Density and Agitation 20

2.5 Electrodeposition Baths 24

2.6 Pitting 28

2.7 pH Levels 28

2.8 Deposit Thickness 28

2.9 Current Efficiency 32

2.10 Magnetic Properties 33

2.11 Mechanical Properties 34

2.12 Testing 35

2.13 References 39

3 Experimental Procedures 46

3.1 Fabrication 46

3.1.1 Wafer Preparation Protocol 46

3.1.2 Electroplating Protocol 52

3.2 Testing 57

3.2.1 Mechanical Properties Testing Protocol 57

3.2.2 Data Acquisition Protocol 61

4 Statistical Analysis 68

4.1 Preliminary Study 68

4.2 Statistical Model: Young Modulus 85

4.3 Regression Model and Response Surface for Young Modulus 107

4.4 Young Modulus' Plots as a Function of the Boundary Conditions .. 111

4.5 Results Young Modulus: Design-Expert Software 115

4.6 Design-Expert Plots: Young Modulus 118

4.7 Statistical Model: Ultimate Strength 131

4.8 Regression Model and Response Surface for Ultimate Strength 150

4.9 Ultimate Strength's Plots as a Function of the Boundary Conditions 153

4.10 Results Ultimate Stress: Design-Expert Software 158

4.11 References 173

5 Discussion and Conclusion 174

5.1 Young Modulus' Plots 176

5.2 Ultimate Strength's Plots 180

5.3 Surface Grain Profile and Electrodeposition's Uniformity 185

5.4 Conclusion 208

5.5 Reference 210

LIST OF FIGURES

Figure 1-1 MEMS gas turbine engine prototype 5

Figure 1-2 Cross-Section through a 9-layer MEMS gas turbine engine prototype 5

Figure 1-3 Engine packaged with fuel 6

Figure 1-4 Array of compressors on a wafer demonstrating the batch fabrication nature of MEMS 6

Figure 1-5 First-generation generator and power electronics driven by an integrated air turbine, powering a PDA at 5 V and 2.5 W 8

Figure 1-6 Second-generation genitor and power electronics driven by an external air turbine, powering a bank of LEDs 9

Figure 1-7 Electroplated stator from the second-generation generator 9

Figure 1-8 Permanent-magnet rotor 10

Figure 1-9 Heavy Rotor Schematic using NdFeB permanent magnet material laminated in the Silicon Hub with electro-deposited NiFe 12

Figure 2-1 Typical electroplating setup with constant current 17

Figure 2-2 The effect of current density and electrolyte agitation on deposit composition for the family of sulfamate/chloride electrolytes 22

Figure 2-3 The effect of current density and electrolyte agitation on plating efficiency for the family of sulfamate/chloride electrolytes 23

Figure 2-4 B-H curves for $Ni_{80}Fe_{20}$ 24

Figure 2-5 B-H curves for electroplated materials 25

Figure 2-6 Mechanical Testing System (MTS) with Laser Extensometer first generation tensile testing system used at CAU 36

Figure 2-7 Advanced Micro-Nano Test System 37

Figure 2-8 Advanced Micro-Nano Test System with Atomic Force Microscope 37

Figure 2-9 Measurement system calibration using clip on extensometer, strain gage, and laser extensometer 38

Figure 3-1 Plasma Enhanced Chemical Vapour Deposition (PECVD) 47

Figure 3-2 The PECVD has two chambers, each capable of holding six wafers 48

Figure 3-3 The DC Sputter (Georgia Tech Clean Room) 49

Figure 3-4 CEE Model 100CB Spinner/ Hotplate 50

Figure 3-5 Specimen design mold 51

Figure 3-6 The CAU Electroplating setup with constant current source 53

Figure 3-7 The anode consists of a nickel alloyed bar—98% pure nickel—is connected to the positive terminal of the power supply 54

Figure 3-8 A Si wafer containing five electrodeposited NiFe test specimens 56

Figure 3-9 EDS (Energy Dispersive Spectrometer) composition printout for electroplated NiFe 58

Figure 3-10 Actual NiFe test specimen; and schematic drawing of a dog-bone shape NiFe test specimen depicting dimensions 59

Figure 3-11 Schematic of CAU Micro/Nano Scale Testing System 60

Figure 3-12 An actual failed NiFe test specimen depicted in the Micro/Nano Scale Testing System 61

Figure 3-13 Laser Extensometer aligned along test specimen 62

Figure 3-14 Laser Extensometer setup display buttons 63

Figure 3-15 Dasylab Application setup and display 64

Figure 3-16 Test specimen aligned with laser…gauge length is the distance between the two metallic tape strips 65

Figure 3-17 Actual stress-strain curve for a NiFe test specimen. All three curves represent the same specimen—two uploads and finally load to failure 67

Figure 4-1 The X-ray diffraction pattern of electroplated $Ni_{80}Fe_{20}$ film, as deposited, after annealed at 500 °C and 700 °C 69

Figure 4-2 AFM micrograph of electroplated $Ni_{80}Fe_{20}$ as deposited (4x4 μm^2) ... 70

Figure 4-3 AFM micrograph of electroplated $Ni_{80}Fe_{20}$ after annealed at 500°C for 5 hours (3.0 x 3.0 μm^2) 71

Figure 4-4 The effect of current density and electrolyte agitation on deposit composition for the family of sulfamate/chloride electrolytes 73

Figure 4-5 The effect of current density and electrolyte agitation on plating efficiency for the family of sulfamate/chloride electrolytes 74

Figure 4-6 Large $Ni_{80}Fe_{20}$ dog-bone test specimen 75

Figure 4-7 MTS Full Load tensile Testing System with large dog-bone test specimen 75

Figure 4-8 Stress-Strain Curves for $Ni_{80}Fe_{20}$ preliminary using the MTS testing system and large dog-bone test specimens 77

Figure 4-9 Advanced Micro-Nano Scale Test System 79

Figure 4-10 Schematic of CAU's Micro/Nano Scale Testing System; and the Micro/Nano Scale Testing System, developed CAU, along with an Atomic Force Microscope (AFM) 79

Figure 4-11 Schematic of new design dog-bone test specimen; and actual smaller dog-bone test specimen 80

Figure 4-12 Measurement system calibration using clip on extensometer, strain gage, and laser extensometer 81

Figure 4-13 Ultimate Strength as a function of thickness 83

Figure 4-14 Stress strain curve of $Ni_{80}Fe_{20}$ baseline condition: Agitation = 300 rpm; Temperature = 25°C; and Current Density = 10 mA/cm^2 84

Figure 4-15 Treatment combinations in the 2^3 design 87

Figure 4-16 2^3 Factorial Design Treatment Combinations Cube for Young Modulus 88

Figure 4-17 Young Modulus' Main Effect of Agitation (A) 93

Figure 4-18 Young Modulus' Main Effect of Temperature (T) 94

Figure 4-19 Young Modulus' Main Effect of Current Density (C) 96

Figure 4-20 Young Modulus' Agitation-Temperature (AT) interaction 98

Figure 4-21 Young Modulus' Agitation-Current Density (AC) interaction 100

Figure 4-22 Young Modulus' Temperature-Current Density (TC) interaction 101

Figure 4-23 Young Modulus' Agitation-Temperature-Current Density (ATC) interaction 102

Figure 4-24 Young Modulus with varying agitation (A) and temperature (T); and constant current density (C = 5.0 A/cm^2) 111

Figure 4-25 Young Modulus with varying agitation (A) and temperature (T); and constant current density (C = 7.5 A/cm^2) 111

Figure 4-26 Young Modulus with varying agitation (A) and temperature (T); and constant current density (C = 10.0 A/cm^2) 112

Figure 4-27 Young Modulus with varying agitation (A) and current density (C); and constant temperature (T = 50 Deg C) 112

Figure 4-28 Young Modulus with varying agitation (A) and current density (C); and constant temperature (T = 37.5 Deg C) 113

Figure 4-29 Young Modulus with varying agitation (A) and current density (C); and constant temperature (T = 25 Deg C) 113

Figure 4-30 Young Modulus with varying temperature (T) and current density (C); and constant agitation (A = 300 rpm) 114

Figure 4-31 Young Modulus with varying temperature (T) and current density (C); and constant agitation (A = 150 rpm) 114

Figure 4-32 Young Modulus with varying temperature (T) and current density (C); and constant agitation (A = 0 rpm) 115

Figure 4-33 Normal Probability Plot of Residuals for Young Modulus 118
Figure 4-34 Residuals verses Predicted Plot for Young Modulus 119
Figure 4-35 Predicted vs. Actual Value Plot for Young Modulus 120
Figure 4-36 Box-Cox Plot for Power Transforms—Young Modulus 121
Figure 4-37 2D Desirability Plot for Young Modulus as a function of agitation and temperature—current density is fixed at 5.0 mA/cm^2 122
Figure 4-38 One Factor Plot of Young Modulus (E) as a function of agitation (A) 123
Figure 4-39 One Factor Plot of Young Modulus (E) as a function of Temperature (B) 124
Figure 4-40 One Factor Plot of Young Modulus (E) as a Current Density C) 125
Figure 4-41 Two Factor Interaction of Young Modulus Plot as a function of agitation (A) and temperature (T) 126
Figure 4-42 Two Factor Interaction Plot of Young Modulus as a function agitation (A) and current density (C) 127
Figure 4-43 Two Factor Interaction Plot of Young Modulus as a function of temperature (T) and current density (C) 128
Figure 4-44 3D Surface Plot of Young Modulus as function of agitation and temperature 129
Figure 4-45 Young Modulus 3D surface Plot as function of agitation and temperature 130
Figure 4-46 Treatment combinations in the 2^3 design 131
Figure 4-47 Treatment combinations in the 2^3 design with σ_{ult} values 132
Figure 4-48 Ultimate Stress' Main Effect of Agitation (A) 137
Figure 4-49 Ultimate Stress' Main Effect of Temperature (T) 138
Figure 4-50 Ultimate Stress' Main Effect of Current Density (C) 139
Figure 4-51 Ultimate Stress' Agitation-Temperature (AT) interaction 142
Figure 4-52 Ultimate Stress' Agitation-Current Density (AC) interaction 143
Figure 4-53 Ultimate Stress' Temperature-Current Density (TC) interaction. 144

Figure 4-54 Ultimate Stress' Agitation-Temperature-Current Density (ATC) interaction 145

Figure 4-55 Ultimate Strength with varying agitation (A) and temperature (T) ... 153

Figure 4-56 Ultimate Strength with varying agitation (A) and temperature (T) ... 153

Figure 4-57 Ultimate Strength with varying agitation (A) and temperature (T) ... 154

Figure 4-58 Ultimate Strength with varying agitation (A) and current density (C) 154

Figure 4-59 Ultimate Strength with varying agitation (A) and current density (C) 155

Figure 4-60 Ultimate Strength with varying agitation (A) and current density (C) 155

Figure 4-61 Ultimate Strength with varying temperature (T) and current density (C) 156

Figure 4-62 Ultimate Strength with varying temperature (T) and current density (C) 156

Figure 4-63 Ultimate Strength with varying temperature (T) and current density (C) 157

Figure 4-64 Normal Probability Plot of Residuals for Ultimate Strength 160

Figure 4-65 Plot of Residual vs. Predicted for Ultimate Strength 161

Figure 4-66 Predicted vs. Actual Value Plot for Ultimate Strength 162

Figure 4-67 External Studentized Residual Plot for Ultimate Strength 163

Figure 4-68 Box-Cox Plot for Power Transforms—Ultimate Strength 164

Figure 4-69 One Factor Plot of Ultimate Strength Plot as a function of agitation 165

Figure 4-70 One Factor Plot of Ultimate Strength as a function of temperature 166

Figure 4-71 One-Factor Plot of Ultimate Strength current density 167

Figure 4-72 Two-Factors Interaction Plot of Ultimate Strength Plot as a function of agitation and temperature 168

Figure 4-73 Two-Factors Interaction Plot of Ultimate Strength Plot as a function agitation and current density 169

Figure 4-74 Two-Factors Interaction Plot of Ultimate Strength as a function of current density and temperature 170

Figure 4-75 3D Surface Desirability Plot of Ultimate Strength as a function of agitation and temperature. Current density are fixed at 10.0 A/cm^2 171

Figure 4-76 3D Surface Desirability Plot of Ultimate Strength as a function of agitation and temperature. Current density is fixed at 5.0 A/cm^2 172

Figure 5-1 Comparison of Young Modulus as a function of temperature and agitation with constant current density 177

Figure 5-2 Comparison of Young Modulus as a function of agitation and current density with constant temperature 178

Figure 5-3 Comparison of Young Modulus as a function of temperature and current density with constant agitation 179

Figure 5-4 Comparison of Ultimate Strength as a function of agitation and temperature with constant current density 182

Figure 5-5 Comparison of Ultimate Strength as a function of agitation and current density with constant temperature 183

Figure 5-6 Comparison of Ultimate Strength as a function of temperature and current density with constant agitation 184

Figure 5-7a SEM pictures depicting surface grain profile for $Ni_{80}Fe_{20}$; boundary conditions: (0 rpm/50°C/10 A/cm^2), and (0 rpm/50°C /5 A/cm^2) 187

Figure 5-7b Histograms displaying the distribution of gray values and sizes for $Ni_{80}Fe_{20}$ for boundary conditions: (0 rpm/50°C/10 A/cm^2), and (0 rpm/50°C /5 A/cm^2) 188

Figure 5-7c Gray Value Plots versus distances for $Ni_{80}Fe_{20}$ for boundary conditions: (0 rpm/50°C/10 A/cm^2), and (0 rpm/50°C /5 A/cm^2) 189

Figure 5-8a SEM pictures depicting surface grain profile for $Ni_{80}Fe_{20}$; boundary conditions: (0 rpm/50°C/10 A/cm^2), and (0 rpm/25°C /10 A/cm^2).....191

Figure 5-8b Histograms displaying the distribution of gray values and sizes for $Ni_{80}Fe_{20}$ for boundary conditions: (0 rpm/50°C/10 A/cm^2), and (0 rpm/25°C /10 A/cm^2).....192

Figure 5-8c Gray Value Plots versus distances for $Ni_{80}Fe_{20}$ for boundary conditions: (0 rpm/50°C/10 A/cm^2), and (0 rpm/25°C /10 A/cm^2) ...193

Figure 5-9a SEM pictures depicting surface grain profile for $Ni_{80}Fe_{20}$; boundary conditions: (0 rpm/50°C/5 A/cm^2), and (100 rpm/25°C /10 A/cm^2).....195

Figure 5-9b Histograms displaying the distribution of gray values and sizes for $Ni_{80}Fe_{20}$ for boundary conditions: (0 rpm/50°C/5 A/cm^2), and (100 rpm/25°C /10 A/cm^2).....196

Figure 5-9c Gray Value Plots verse distances for $Ni_{80}Fe_{20}$ for boundary conditions: (0 rpm/50°C/5 A/cm^2), and (100 rpm/25°C /10 A/cm^2).....197

Figure 5-10a SEM pictures depicting surface grain profile for $Ni_{80}Fe_{20}$; boundary conditions: (0 rpm/50°C/10 A/cm^2), and (100 rpm/25°C /10 A/cm^2).....198

Figure 5-10b Histograms displaying the distribution of gray values and sizes for $Ni_{80}Fe_{20}$ for boundary conditions: (0 rpm/50°C/10 A/cm^2), and (100 rpm/25°C /10 A/cm^2).....199

Figure 5-10c Gray Value Plots versus distances for $Ni_{80}Fe_{20}$ for boundary conditions: (0 rpm/50°C/5 A/cm^2), and (100 rpm/25°C /10 A/cm^2).....200

Figure 5-11a Surface uniformity for boundary condition: (A/T/C) = (0 rpm/50 deg C/10 mA/cm^2) 202

Figure 5-11b Surface uniformity for boundary condition: (A/T/C) = (0 rpm/50 deg C/5 mA/cm^2) 203

Figure 5-11c Surface uniformity for boundary condition: (A/T/C) = (0 rpm/25 deg C/5 mA/cm^2) 204

Figure 5-11d Surface uniformity for boundary condition:
(A/T/C) = (100 rpm/25 deg C/10 mA/cm^2) 205

Figure 5-11e Surface uniformity for boundary condition:
(A/T/C) = (0 rpm/25 deg C/10 mA/cm^2) 206

Figure 5-12 Stator Die – Plated Laminations – Frontside 207

LIST OF TABLES

Table 2-1 Bath Composition/Properties of Electroplated Iron Deposited 26

Table 3-1 80-20 Nickel plating solution.....55

Table 4-1 The X-ray diffraction data of bulk $Ni_{80}Fe_{20}$, electroplated NiFe film, as deposited, after annealed at 500°C and 700°C 69

Table 4-2 Young's Modulus (E) and Ultimate Stress (σ_{ult}) values for preliminary test specimen. 76

Table 4-3 $Ni_{80}Fe_{20}$ Specimens test matrix for 2^3 Factorial Analysis DOE 82

Table 4-4 The Analysis of Variance Table for the Three-Factor Fixed Model ...86

Table 4-5a Measured Young Modulus (E) values and standard deviation for each test case.....89

Table 4-5b Algebraic Sign for Calculating Effects in the 2^3 Design, with measured Young Modulus (E) values.....90

Table 4-6 Agitation-Temperature (AT) Interaction Calculation.....97

Table 4-7 Effect Estimate Summary for Young Modulus E.....105

Table 4-8 Measured for Young Modulus' (E) values at the boundary conditions.....106

Table 4-9 Design-Expert Software Printout for Response Variable Young Modulus... 115

Table 4-10a Measured σ_{ult} values and standard deviation for each test case.....133

Table 4-10b Sign for Calculating Effects in the 2^3 Design.....134

Table 4-11 Agitation-Temperature (AT) Interaction Calculation.....141

Table 4-12 Effect Estimate Summary for Ultimate Strength σ_{ult}.....148

Table 4-13 Ultimate Strength (σ_{ult}) from Experiment 149

CHAPTER 1

INTRODUCTION

The Power and Energy eight-year research effort is intended to demonstrate an operating microfabricated gas turbine engine and electric generator. These devices would provide proof-of-concept of the capabilities of Power MEMS (Micro Electrical Mechanical Systems); and demonstrate the feasibility of this technology evolving into a micro-gas turbine generator in a package measuring a few cubic centimeters. Logistic fueled power systems would be a minimal logistical burden while extending the time and range of operations.

This proof-of-concept power MEMS will demonstrate that a micro-gas-turbine generator may do the following:

1) Decrease the mass of the Soldier power systems by 2-4 times in the near term and up to 10 times in the longer term.
2) Reduce the logistics burden by eliminating the battery logistics.

Reduce the life-cycle cost of the Soldier power by an order of magnitude or more. The evolution of Power MEMS technology creates new challenges. One of these challenges is the mechanical properties of thin film materials used in power MEMS. In particular, this research focuses on the mechanical properties of electrodeposited $Ni_{80}Fe_{20}$. Electrodeposited $Ni_{80}Fe_{20}$ is a thin-film material used in power MEMS (high speed magnetic generator). The mechanical properties of electrodeposited $Ni_{80}Fe_{20}$

differ substantially from that of bulk nickel iron. There is not any published data on the mechanical properties; and unlike bulk nickel iron whose mechanical properties are a function of volume, the mechanical properties of electrodeposited $Ni_{80}Fe_{20}$ are driven by the electrolytes' boundary conditions.

The mechanical properties of electrodeposited $Ni_{80}Fe_{20}$ are vital to the success of Power MEMS; it is the mechanical properties that determine the structural integrity of the device. Therefore, the focus of this research is the mechanical properties of electrodeposited $Ni_{80}Fe_{20}$ and how these properties are influenced by the electrolytes' boundary conditions. Recent developments and ongoing research in Power MEMS are discussed in section 1.1 through 1.6.

1.1 MEMS Gas Turbine Engine

A MEMS gas turbine generator is under development. This device will serve as a battery replacement providing 10 to 20 W of electric power from a 5 cubic centimeter engine with a mass of about 10 grams (excluding the fuel and fuel tank). The overall efficiency of this micro-scale engine is constrained by its size and micro-fabrication capabilities, but its performance relative to batteries will still be impressive. The MEMS gas turbine generator system (including fuel and fuel tank) will weigh 5-10 times less than current batteries at an equivalent energy level. This weight reduction is possible because the gas turbine is a fueled system benefiting from the high energy content of hydrocarbon fuels. The power and energy density of this device will significantly reduce the load soldiers carry. This engine will showcase the feasibility of a MEMS gas turbine by demonstrating self-sustaining

operation by the end of the program. Self-sustaining operation is considered a major milestone for the program.

1.2 Accomplishments:

Models were developed, verified, and then combined into an overall engine system model. The model integrates couplings between the different subsystems, critical for accurate representation of system performance. The model highlighted several issues related to the MEMS gas turbine that are atypical.

As speed increases in a typical gas turbine, its power outpaces compressor power and viscous loss. As a result, net power also increases. In a MEMS gas turbine with lower efficiency turbomachinery (due to fabrication constraints and scale) and limited thermal isolation, as speed increases compressor power outpaces turbine power because increases in viscous loss results in substantial increases in heat transfer to the compressor. This detrimentally impacts compressor performance. Increased speed does not necessarily increase net power in the MEMS gas turbine. The model was used to explore and understand the engine operational characteristics. Optimization runs were performed to maximize net power and minimize fabrication complexity. The design is consistent with fabrication capabilities and self-sustaining operation.

The MEMS engine is arguably the most complex MEMS device ever built. To manage risk, our development philosophy is one of evolution, minimizing the number of process steps required in a new device. The gas turbine engine is similar in design to the successful turbocharger device described elsewhere. The engine

contains two major differences critical for engine operation. First is an additional layer in the rotor, consisting of a small diameter shaft that increase the thermal isolation between the compressor and turbine—the compressor performance is severely reduced by heat transfer from the turbine. Short loop process tests demonstrated this technology. Second is placing the compressor and turbine blades on separate wafer levels from their supporting disks. This produces uniform height blades that substantially reduce the imbalance in the rotor, a necessity for stable high speed rotation. The cost is an increased number of wafers and bonds required; thereby, increasing its complexity. This technology has been demonstrated in a build of a high-speed MEMS bearing test device.

The design model and fabrication process results were incorporated into an engine design of ten wafer levels. The design was translated into photolithography masks used by the MIT micro-fabrication facility to lay out the engine patterns on silicon wafers. Twenty-eight (28) photolithography masks were drawn and fabricated. The result is the fabrication of the first ever build of a self-sustaining MEMS gas turbine engine (see Figures 1-1 through 1-4).

1.3 Project Leaders:

This project involved several institutions, which are listed below:

Professor Alan Epstein, Massachusetts Institute of Technology

Professor Mark Allen, Georgia Institute of Technology

Professor David Veazie, Clark Atlanta University

Professor Reza Ghodssi, University of Maryland

Professor Brad Lehman, Northeastern University

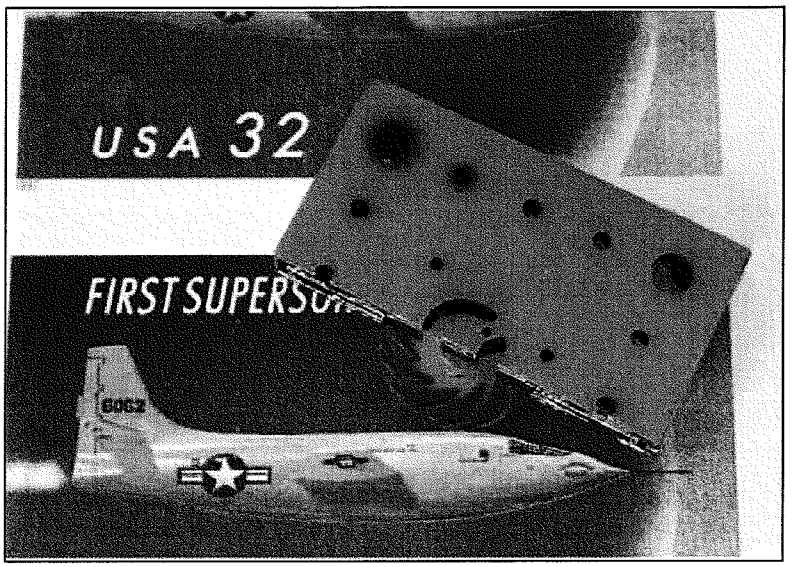

Figure 1-1: MEMS gas turbine engine prototype.

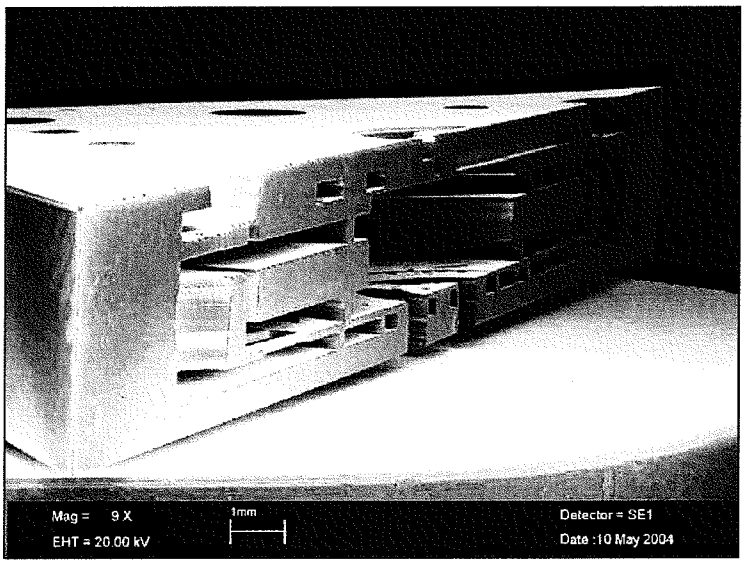

Figure 1-2: Cross-Section through a 9-layer MEMS gas turbine engine prototype. (Courtesy of Bernard Chih-Hsun Yen, MIT)

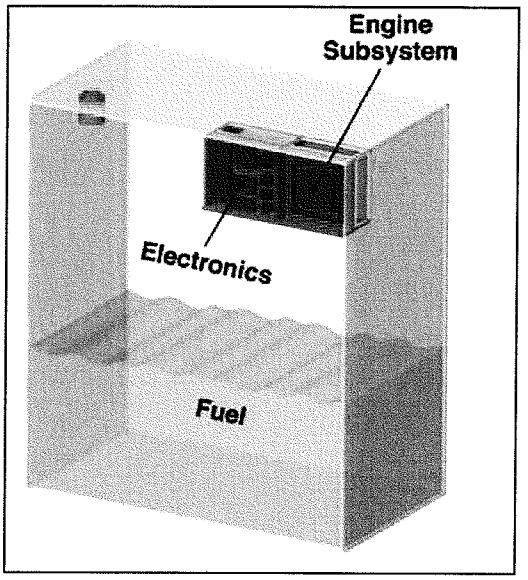

Figure 1-3: Engine packaged with fuel. Due to its very high power density, the MEMS engine volume is negligible relative to the fuel volume.

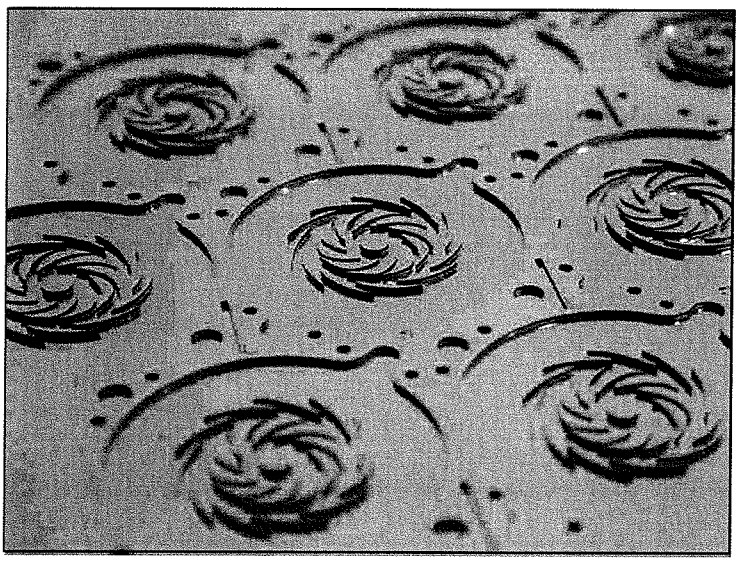

Figure 1-4: Array of compressors on a wafer demonstrating the batch fabrication nature of MEMS.

1.4 MEMS Magnetic Generator

Small-scale permanent-magnet synchronous motors and generators are under development. These machines, operating at or above the multi-watt power level, are fabricated from bonded stacks of silicon wafers using a combination of standard MEMS silicon processing, and electroplating of integrated magnetic materials and thick conductors. Their fabrication is batch implemented, enabling low-cost high volume production. Scaling their size to the centimeter range of Power MEMS, the machines operate with current densities 100 times larger than conventional machines at very high speeds. The large current densities result in power densities above 10^7 W/m^3 with a power output near 10 W, a 10-fold improvement in power density over conventional large-scale machines. When operated as motors, the machines serve as coolant fuel pumps, or air handlers. When operated as generators, the machines serve as electric power sources for soldiers, autonomous sensors, or robots.

The magnetic motors and generators described here are designed to be integrated with the MEMS gas turbines. Their size, shape and operating speed matches that of the gas turbines, and they share the same materials and fabrication processes. Attention has been paid to the thermal design of the gas turbines to use the requisite magnetic materials at suitably low temperatures.

1.5 Accomplishments

The primary accomplishment is the development and demonstration of high-power-density magnetic motors and generators operating in the 10 watt range. These machines have been demonstrated as generators. For example, Figure 1-5 shows a

first-generation generator with its power electronics powering a PDA. The generator and the conventional air turbine that drives it are not visible inside the package; the power electronics; however, are visible. The turbine and generator operate near 200,000 rpm. The electrical power that they produce is conditioned by the power electronics and delivered to the PDA at 5 V and approximately 2.5 W with a pneumatic-to-electrical efficiency more than 40%. Figure 1-6 shows the operation of a second-generation generator with its power electronics lighting a bank of LEDs. This system has generated nearly 10 W of power at 350,000 rpm with efficiency above 50%; Figures 1-7 and 1-8 show close-up views of the electroplated stator and permanent-magnet rotor.

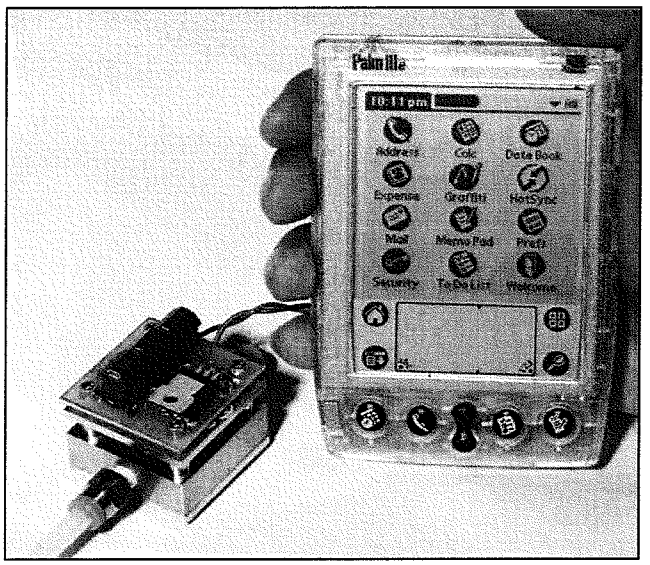

Figure 1-5: First-generation generator and power electronics driven by an integrated air turbine, powering a PDA at 5 V and 2.5 W. (Power and Energy)

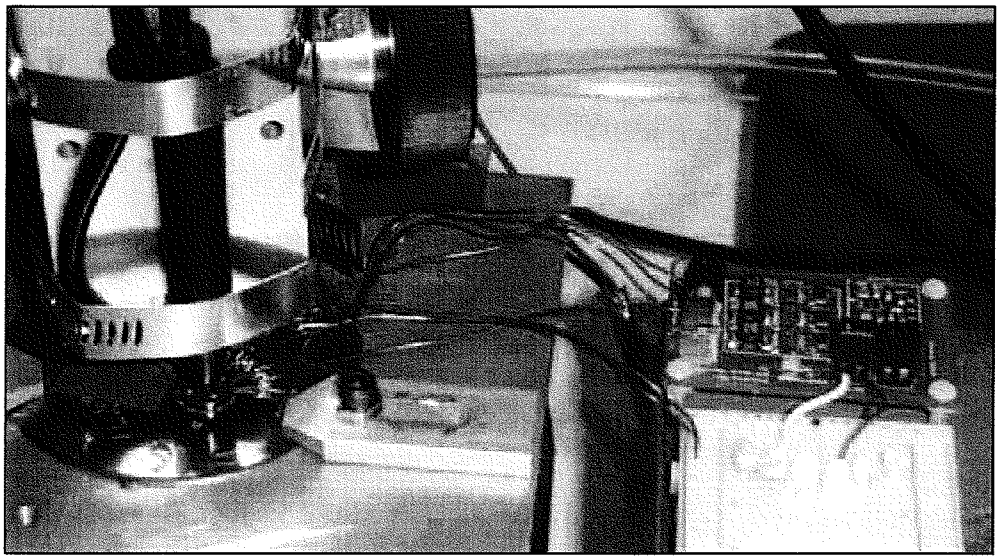

Figure 1-6: Second-generation generator and power electronics driven by an external air turbine, powering a bank of LEDs. (Power and Energy)

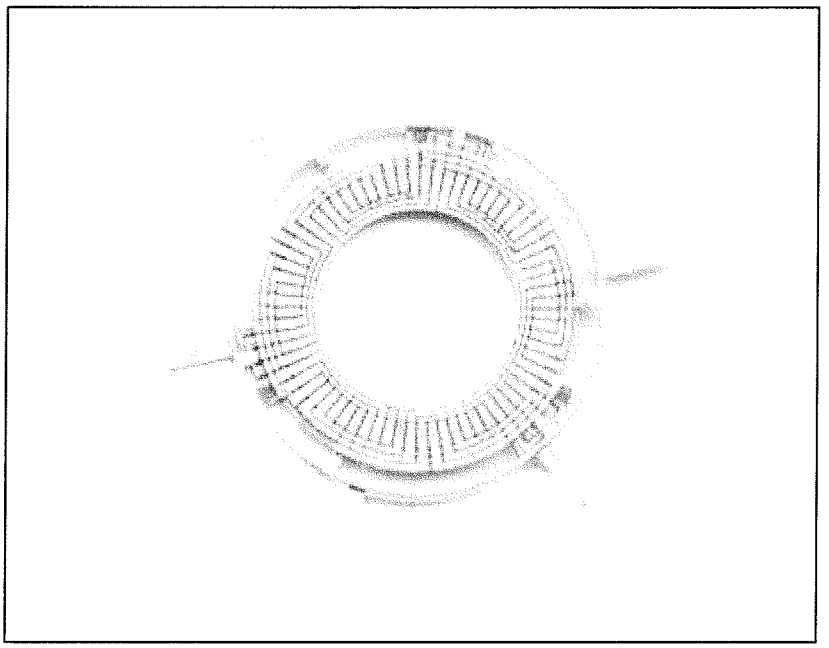

Figure 1-7: Electroplated stator from the second-generation generator. (Courtesy of Bernard Chih-Hsun Yen, MIT)

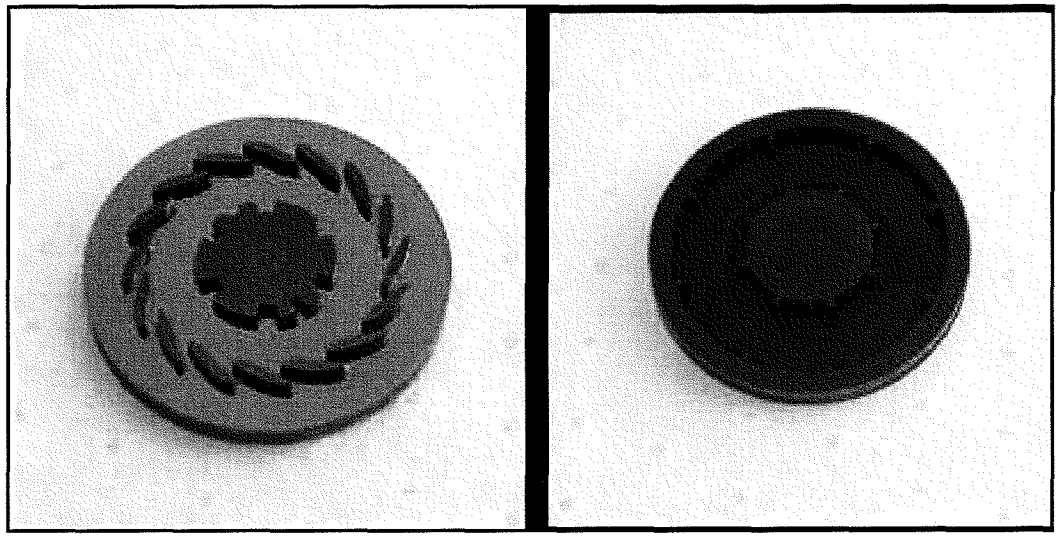

Figure 1-8: Permanent-magnet rotor (left) top view, and (right) bottom view. (Courtesy of Bernard Chih-Hsun Yen, MIT)

A variety of multi-disciplinary technological advances underlie the successful demonstrations of the generator systems described above. Models of the mechanical, electromechanical, thermal and electrical behavior of the permanent-magnet synchronous generator systems have been developed, experimentally verified and used for optimized design. Mechanical and magnetic material properties have been measured, at elevated temperatures where necessary, to support the modeling and design efforts. Electroplating fabrication processes for high-aspect-ratio and high-density laminated magnetic cores and multi-layered windings have been developed. It is with these fabrication processes that the windings and cores can be integrated into the silicon structure of the generator body. The models reflect the capabilities of these fabrication processes. Power electronics tailored to the characteristics of the generator have been designed and demonstrated. Air bearings capable of supporting

the relatively heavy rotors of the magnetic generator have been redesigned based on a newly established micro-gas bearing theory and past experience in successfully spinning silicon-based micro turbines at tip speeds near 370 m/s. The fabrication and testing of heavy rotor bearing test devices are underway and will form a first-of-its-kind demonstration of supercritical, high-speed operation of multi-layer compound rotors necessary to enable MEMS based magnetic generators. Finally, power electronics and optimal control algorithms have been devised to operate the turbine generator while charging advanced batteries. Such controls will be most useful for soldier systems.

1.6 Project Leaders:

This project involved several institutions, which are listed below:

Professor Mark Allen, Georgia Institute of Technology

Professor David Veazie, Clark Atlanta University

Professor Alan Epstein, Massachusetts Institute of Technology

Professor Brad Lehman, Northeastern University

1.7 Electrodeposited Nickel Iron

Initially, the proposed magnetic material for the Power MEMS generator was electrodeposited NiFe; composition 80% Ni and 20% Fe. However, it has since been discovered that permanent magnet materials offer significant improvements over electrodeposited magnetic materials. These improvements include an even larger air gap between rotor and stator, eliminating air losses in the machine, higher efficiency, simpler operation, and most importantly, easier fabrication. Because of this, the

Georgia Institute of Technology-Clark Atlanta University-Massachusetts Institute of Technology (GT-CAU-MIT) team decided to use permanent magnet materials to replace the electrodeposited magnetic materials—NiFe. The permanent magnet materials suggested include the NdFeB permanent magnet.

Electrodeposited NiFe is very important to the magnetic generator. Although, Neodymium Iron Boron (NdFeB) is the permanent magnet material of choice; electrodeposited NiFe is used as the back iron material; used to fill the cavities between the silicon and permanent magnet, and laminate the permanent magnet inside the silicon hub. This function is illustrated in Figure 1-9.

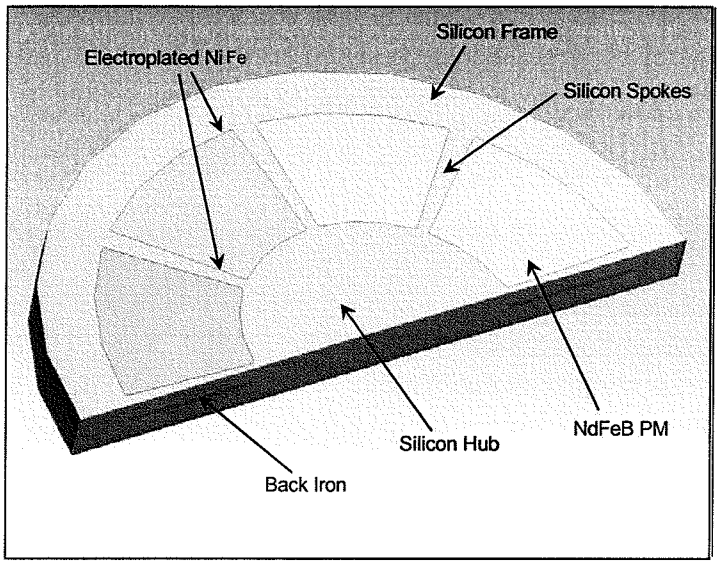

Figure 1-9: Heavy Rotor Schematic using NdFeB permanent magnet material laminated in the Silicon Hub with electro-deposited NiFe. (Courtesy of Bernard Chih-Hsun Yen, MIT)

As a result, electrodeposited nickel iron is a vital material in the Power MEMS Generator. Although, NiFe has excellent magnetic and electrical properties,

the mechanical properties of electrodeposited NiFe have not been studied extensively. Hence, this research will focus on how the electrolytes' boundary conditions influence the mechanical properties of electrodeposited $Ni_{80}Fe_{20}$. The process for achieving the objective is as follows:

1) Design a 2^k Factorial Analysis and Design of Experiments for the critical electrolyte boundary conditions which affect the mechanical properties of electrodeposited $Ni_{80}Fe_{20}$.
2) Conduct Regression Analyses to model the mechanical properties as a function of the critical electrolytes' boundary conditions.
3) Fabricate electrodeposited $Ni_{80}Fe_{20}$ test specimens for mechanical, magnetic, and composition testing.
4) Conduct experiments of test specimens to validate regression analysis models.

In Chapter 2, the results of the literature review were discussed; various electrolytes' boundary conditions were examined; and the most critical surfaced driven boundary conditions were selected. The three critical external electrolytes' boundary conditions selected were: (1) Current density, (2) Temperature, and (3) Agitation. In keeping with the theory of a 2^k Factorial Design Analysis, each external boundary conditions were evaluated at two values: (1) high or maximum value (denoted as upper bound), and (2) low or minimum value (denoted as a lower bound). The objectives were to determine statistically, how these external electrolytes' boundary conditions influence the mechanical properties of electrodeposited NiFe,

and to model the mechanical properties influence as a function of these external electrolytes boundary conditions.

A Factorial Design Analysis (FDA) approach was used for statistical computation and design. A FDA is a between-participants design analysis that includes more than one independent variable. This design has the advantage over the simple randomize design in that you can test the effect of more than one independent variable and the interactive effect of the various independent variables. The FDA is broken down into main and interaction effects.

The main effect is an outcome that is a consistent difference between levels of a factor. An interaction effect is when one factor is a function of or dependent upon another factor. The main effects are produced by the independent variable; whereas, the interaction effects occurs when the effect of one independent variable depends on the level of the other independent variables being considered.

Therefore, the three specific advantages to using a FDA in experimentation rather than the classical methods are:

(1) Efficiency/economy—requires fewer participants and retains the same degree of accuracy.

(2) Comprehensiveness—in additional to analyzing the effect of a single factor, FDA enables us to analyze the effect of the interactions as well.

(3) Wider inductive basis—allows for a broader interpretation of results, i.e. the conclusions are based on an experiment having many independent

factors and these factors have been tested under a broader range of conditions than if only one variable had changed at a time.

In Chapter 3, the experimental procedures are discussed: the fabrication process for the silicon wafer and seed layer; the fabrication of the electrodeposited nickel iron; the mechanical tensile test procedure; and the calculation of the mechanical properties. In Chapter 4, preliminary studies for Young Modulus and Ultimate Strength are analyzed and discussed; a DOE test matrix is identified and a 2^k Factorial Statistical Analysis is conducted, analyzed, and mathematical models describing how the electrolytes' boundary conditions influence the mechanical properties is derived. Finally, in Chapter 5 the results obtained in Chapter 4 are discussed and SEM pictures depicting surface conditions are compared.

CHAPTER 2

LITERATURE REVIEW

In this Chapter, previous works were examined in an effort to obtain data regarding the electrical and magnetic properties of electrodeposited $Ni_{80}Fe_{20}$, and to provide insight concerning the surface-driven factors (electrolytes' boundary conditions) that influence the mechanical properties. In Chapter 3, these critical electrolytes' boundary conditions are used to fabricate $Ni_{80}Fe_{20}$ test specimens and obtain the mechanical properties as a function of the critical electrolytes' boundary conditions; and in Chapter 4, mathematical models describing the mechanical properties behavior as it relates to these critical electrolytes' boundary conditions. The results are discussed in Chapter 5.

2.1 Electrodeposition

Electrodeposition is the process used in electroplating; where electroplating is the process of using electrical current to reduce metal cations—an atom or group of atoms carrying a positive charge—in a solution and coat a conductive object with a thin layer of metal; Dufour [1] .

The primary application of electroplating is to deposit layer(s) of a metal having some desired property (example, abrasion and wear resistance, corrosion protection, lubricity, improvement of aesthetic qualities, magnetic, etc.) onto a surface lacking that property. Also electroplating is used to build up thickness on undersized parts. This research focuses on electroplating to fabricate the magnetic permalloy $Ni_{80}Fe_{20}$.

The part to be plated is the cathode of the circuit; the anode is made of the metal to be plated on the part. Both components are immersed in a solution called an "Electrolyte" containing one or more dissolved metal salts as well as other ions that permit the flow of electricity. A rectifier supplies a direct current to the cathode causing the metal ions in the electrolyte solution to lose their charge and plate onto the cathode. As the electrical current flows through the circuit, the anode slowly dissolves and replenishes the ions in the bath. A typical setup of an electroplating bath is shown in Figure 2-1.

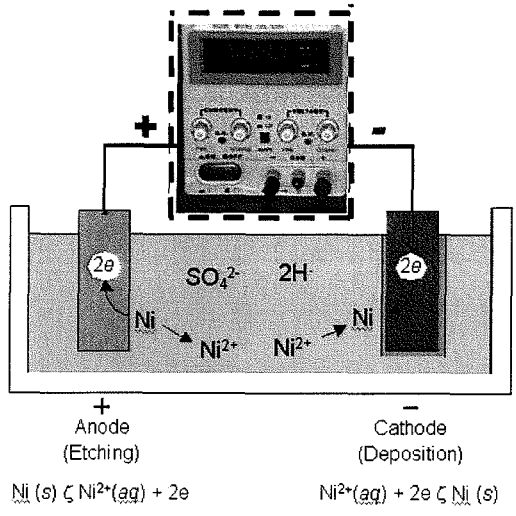

Figure 2-1: Typical electroplating setup with constant current.

2.2 Electroplated NiFe

Electroplating has been a process of major significance in the fabrication of thin-film recording heads, which are important components in magnetic recording hardware. The development of electroplating processes for nickel-iron alloys, such as

$Ni_{80}Fe_{20}$, enabled thin-film recording heads to become technologically viable. With the introduction of thin-film inductive heads and, later, magnetoresistive (MR) heads, the disk-drive field has been able to sustain rapid growth, Andricasos [2]. Magnetic microactuators and inductors such as solenoids, valves, and cantilevers are fabricated using electrodeposited Permalloy ($Ni_{81}Fe_{19}$), Leith [3].

The development of micromachined magnetic devices has relied primarily on the use of nickel-iron permalloy ($Ni_{80}Fe_{20}$). Permalloy is used in a number of applications since it has good soft magnetic properties, high permeability, high magnetoresistive effect, low magnetostriction, stable high frequency operation, and excellent mechanical properties, Taylor [4]. In hard disk magnetic recording heads, permalloy is widely used for magnetoresistive sensors and flux guiding elements, Mallinson [5]. Devices such as magnetic separators, Liakopoulos [6]; micropumps, Zhang [7]; magnetic micromotors, Wagner [8], Ahn [9], and Guckel [10]; inductors, Ahn [11]; switches, Wright [12]; and microrelays, Taylor [13]; have also been fabricated using permalloy as the magnetic material as well as moving members. Permalloy microstructures have been used as flux guides for sensitivity improvement of magnetotransistors, Schneider [14] and as a ferromagnetic core in mircofluxgate sensors, Choi [15]. These structures can be integrated with complementary metal oxide semiconductor (CMOS) circuitry on a single chip. Electroplated nickel iron was a key magnetic material under consideration for the high-speed micro-rotor disc for the magnetic generator; however due the significant power improvement generated by permanent magnet Neodymium Iron Boron (NdFeB), precision laser cut

NdFeB (formed in annulus "pie" pieces) is the material of choice for the high-speed micro-rotor disc; whereas electrodeposited NiFe is used as the backing material and the material to secure and fill the permanent magnet inside the silicon hub.

2.3 Material Properties: Bulk versus Electroplated

Electrochemical processes including electrodeposition and electroless deposition are well-suited to fulfill the requirements of high yield and cost effective processes. Electrochemical processes have many advantages, such as:

- precisely controlled near room temperature operation
- low energy requirements
- rapid deposition rates
- capability to handle complex geometries
- low cost
- simple scale-up with easily maintained equipment

In addition, the properties of materials can be ''tailored'' by controlling solution compositions and deposition parameters. However, the properties of thin films, particularly electroplated thin films, often differ substantially from their bulk counterparts. As a result, the bulk material properties often do not predict material properties of electroplated thin films, Chung [16]. Since the material properties of thin film/electroplated materials can differ from that of bulk materials at the small scales—scales at which individual MEMS devices are configured—thus causing the material properties behavior to be more influenced by surface-driven effects than by volume or bulk effects.

Leith [17] states that electrodeposited NiFe is very sensitive to electrolyte mixing; the effects of current density, electrolyte agitation, and Ni^{+2}/Fe^{+2} content on deposit composition and plating current efficiency heavily influence the material properties. Leith also states that the magnetic, mechanical, and corrosion properties of NiFe electrodeposits are dictated by a number of factors including metallurgical structure (e.g., grain size, growth orientation) and alloy composition. In turn, these parameters are affected by processing variables such as plating bath chemistry, pH, and temperature as well as the applied current density and electrolyte mixing conditions at the cathode surface.

Therefore in considering MEMS' application such as the high speed micro-generator; in which electroplated NiFe is considered--because of its excellent magnetic properties—an investigation of its mechanical properties must be conducted since these properties can not be derived from the bulk material properties.

2.4 Current Density and Agitation

Leith [18] states that while bath chemistry, pH, and temperature can usually be controlled, significant variations in current density and electrolyte mixing often occur during plating (especially in patterned molds), leading to nonuniformities in deposit composition. Deposition of NiFe alloys with predictable properties, therefore, depends in large part on understanding the effects of electrode polarization and electrolyte mixing on the composition of the deposit.

Using a sulfamate/iron chloride bath suitable for high rate electrodeposition of NiFe alloys; Leith showed the inter-dependence of current density, agitation,

efficiency, and material composition. The average composition of each alloy was calculated from the stripping data using the relationship

$$X_{Fe} = \frac{2}{N}\frac{Q_{R,S}}{Q_{D,S}}, \text{ where} \qquad 2\text{-}1$$

X_{Fe} ≡ average mole fraction iron in the deposit

$Q_{R,S}$ ≡ is the total charge at the ring during stripping

$Q_{D,S}$ ≡ is the total charge at the disk during stripping

N ≡ N is the collection efficiency of the RRDE ($N = 0.217$)

RRDE ≡ rotating ring-disk electrode

and the plating current efficiency, ε_p, for deposition of each alloy was determined from coulombic measurements using the relationship

$$\varepsilon_P = \frac{Q_{D,S}}{Q_{D,P}}, \text{ where} \qquad 2\text{-}2$$

$Q_{D,P}$ = is the total charge on the disk during plating

Figure 2-2 shows the Iron molar concentration as a function of agitation and current density. Figure 2-3 shows the plating efficiency as a function of agitation and current density.

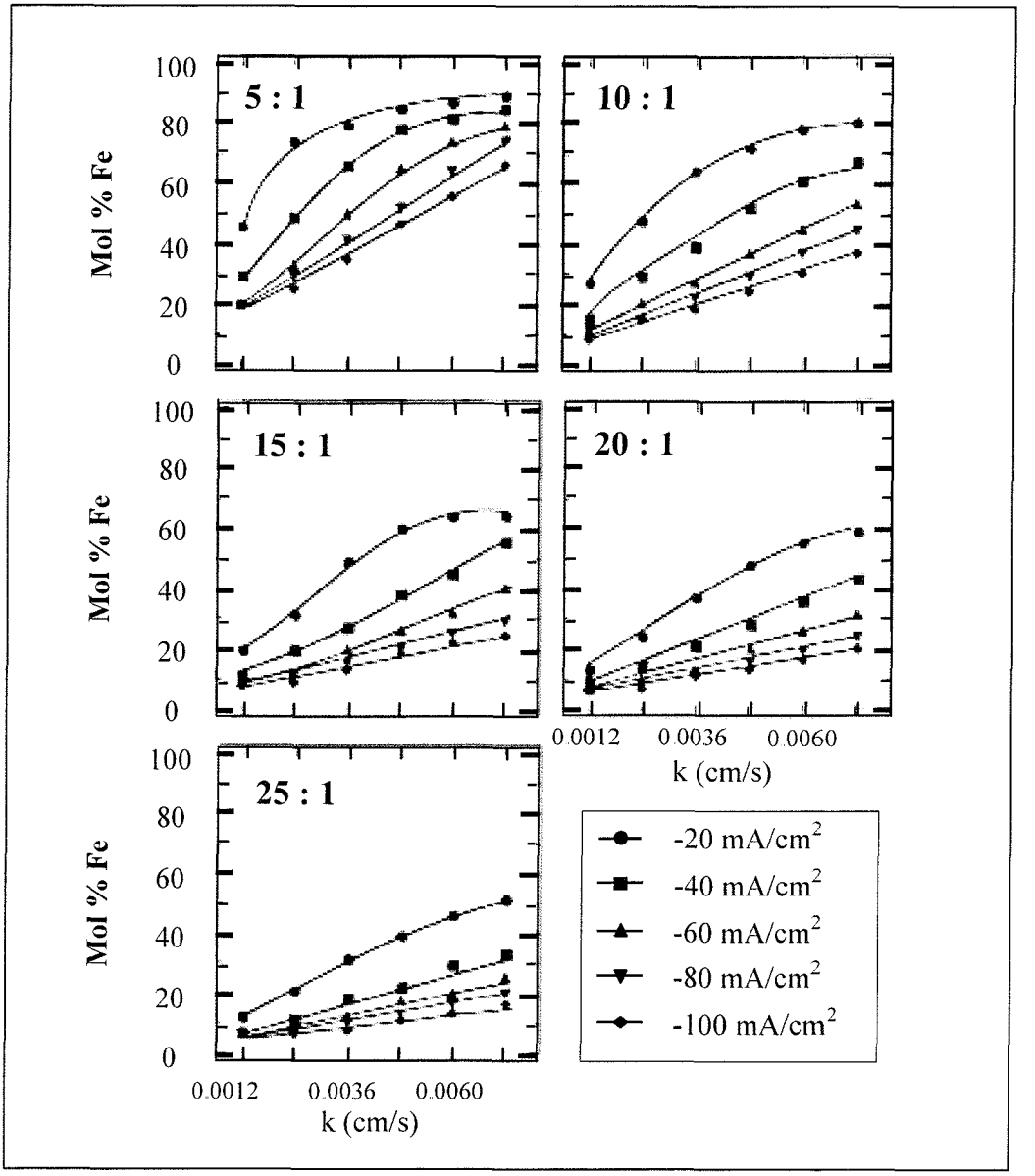

Figure 2-2: The effect of current density and electrolyte agitation on deposit composition for the family of sulfamate/chloride electrolytes. The dissolved Ni^{+2}:Fe^{+2} molar concentration ratio in the five baths varies from 5:1 to 25:1 as indicated; Leith [19].

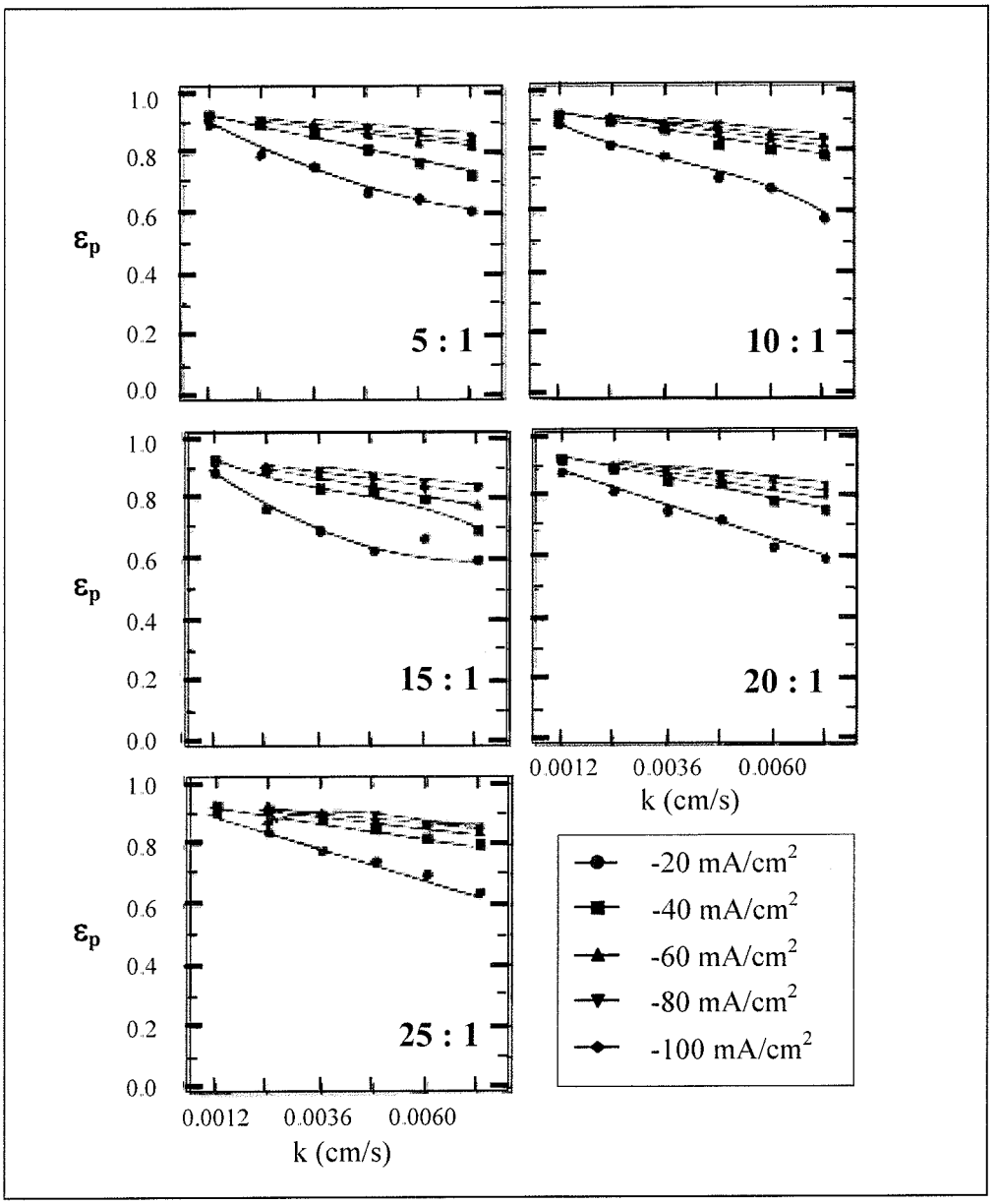

Figure 2-3: The effect of current density and electrolyte agitation on plating efficiency for the family of sulfamate/chloride electrolytes. The dissolved Ni^{+2}:Fe^{+2} molar concentration ratio in the five baths varies from 5:1 to 25:1 as indicated; Leith [20].

2.5 Electrodeposition's Baths

As previously discussed, the electroplated bath's chemistry is crucial to the material properties of the material. The alloy used in this research is electroplated NiFe—one of the proposed material considered for the high speed micro-generator. The magnetic properties of electroplated NiFe have been will documented by Judy [21], and Guckel [22]. Figure 2-4 shows the applied magnetic field on $Ni_{95}Fe_5$ and $Ni_{80}Fe_{20}$.

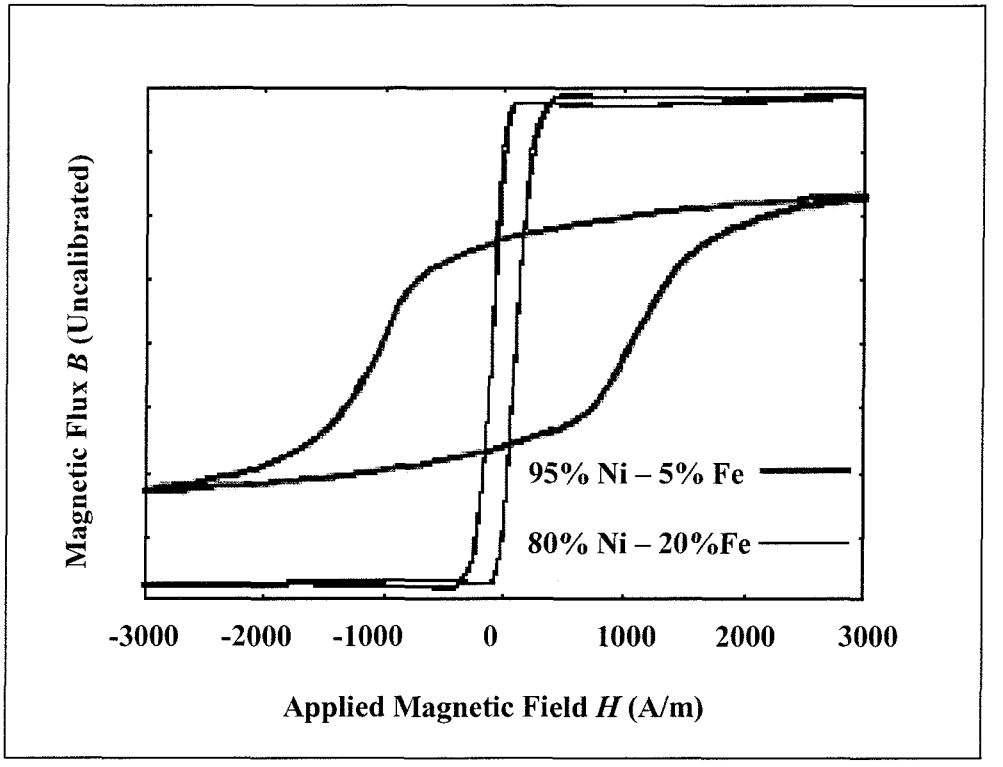

Figure 2-4: B-H Curves for $Ni_{80}Fe_{20}$. The wide *B-H* loop represents the nickel-rich NiFe (95% Ni and 5% Fe) which was used in the devices described in this paper. The narrow *B-H* loop represents Permalloy (80% Ni and 20% Fe) which was deposited during more recent plating attempts. Both loops are for complete films of as-plated material, Judy [23].

The magnetization or B-H curve for electroplated Ni; Ni annealed to 650 °C in nitrogen; Ni annealed to 1100 °C in hydrogen; and $Ni_{78}Fe_{22}$ respectively.

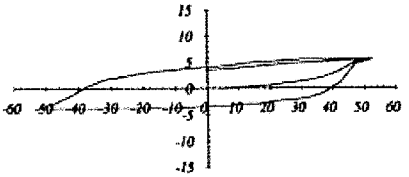

Figure 4a: As-electroplated nickel

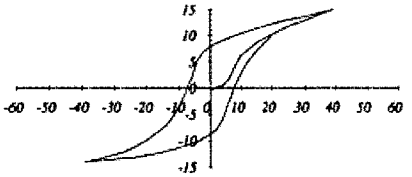

Figure 4b: Electroplated nickel annealed to 650 °C in nitrogen

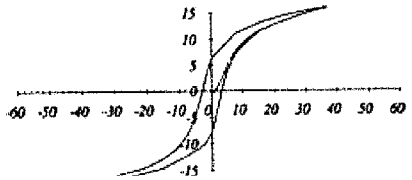

Figure 4c: Electroplated nickel annealed to 1100 °C in hydrogen

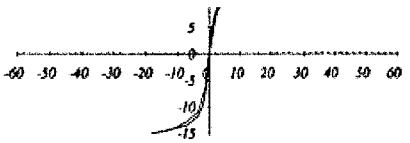

Figure 4d: As-electroplated Ni-Fe (78-22)

Figure 2-5: B-H curves for electroplated materials. The horizontal scale indicates the applied H field in Oersteds and the vertical scale is un-calibrated magnetic flux density B, Judy [24].

There are several NiFe bath's chemistries ranging from the sulfamate based used by Christenson [25], and Leith [26] to the Watts based used by Chung [27]. The objective of this research is to identify a metal alloy with excellent magnetic properties, describe and model its mechanical properties as a function of the bath's parameters—in particular, $Ni_{80}Fe_{20}$.

Tables 2-1 and 2-2 show various iron baths—from Watts to Sulfate—and known mechanical properties associated with the bath.

Table 2-1: Bath Composition/Properties of Electroplated Iron Deposited

	Bath Composition	pH	Temperature (°C)	Current Density (A dm^{-2})	Tensile Strength (Kg mm^{-2})	Elongation (%)	Hardness	Coercive Force
Iron	Sulfate bath	3.4	20	0.5			263	
	$Fe(NH_4)_2(SO_4)_2$	3.4	20	2.0			354	
	Macnaughton [1]	4.4	19	0.5			182	
		4.4	41	2.0			240 (Brinell)	
	Chloride bath, $FeCl_2$ ($120-150\ g\ L^{-1}$ as Fe^{2+}) Subramanyan [2]	3.5-4.7	100-106	400	50-56	5-15		9.5-11.0 (Oe)
	Chloride bath	0-3	86	20	45	2.1		19.5
	$FeCl_2 \cdot 4H_2O$: $400\ g\ L^{-1}$		96	10	42	3.33		18
	$CaCl_2$: $80\ g\ L^{-1}$		96	20	43	4.67		17.5
	Wetting agent: $2\ ml\ L^{-1}$		96	30	43	5.54		22.5
	Harty [3]		108	20	36	2.67		17.5 (Atm^{-1})

Table 2-1: Bath Composition/Properties of Electroplated Iron Deposited Continued

Bath Composition	pH	Temperature (°C)	Current Density (A dm^{-2})	Tensile Strength (Kg mm^{-2})	Elongation (%)	Hardness	Coercive Force
Chloride bath	0.2-0.4	70	15			450	
$FeCl_2 \cdot 4H_2O$: 465 g L^{-1}			5			300	
H_3BO_3: 38 g L^{-1}			2.5			170	
Kllingenmaier [4]		95	15			150	
			5			150	
			2.5			120	
Chloride bath	0	60	2.0			280	
$FeCl_2 \cdot 4H_2O$: 1.57 mol dm^{-3}	1		2.0			250	
$CaCl_2$: 2.04 mol dm^{-3}	2		2.0			200	
Yoshimura [5]						(Vickers)	
Sulfate-chloride bath	2.5	80	8	46	4.3		
FeSO4·7H2O: 500 g L-1			15	56	5.3		
NaCl: 50 g L-1			27	64	2.7		

The NiFe bath for this research was Watts' based as described by Chung [33].

2.6 Pitting

A highly purified and well-worked iron bath does not usually yield pitted deposits; however, pitting is sometimes encountered. It has been shown that stirring of the solution or mechanical agitation of the cathode may also reduce pitting. A "bumping" type of motion is most effective. Air agitation should not be used because it results in excessive oxidation of iron (II); Schlesinger [34].

2.7 pH Levels

Maintaining control of pH is essential. When operated at pH below 3.5, the acid content of the bath is slowly depleted because the anode efficiency is higher than the cathode efficiency: 100% and 80% to 99%, respectively; Schlesinger [35].

Schlesinger also maintain that iron anodes of high purity, such as wrought iron, or Swedish iron, are preferred, but anodes of steel of cast iron have been used. A high-purity iron anode is necessary to obtain ductile deposits, since a hot chloride bath is easily contaminated by impurities contained in the anode materials. All of these dissolve with high efficiency but produce some insoluble sludge residue that may cause rough deposits.

2.8 Deposit Thickness

Faraday's law—Schlesinger [36]—states that the amount of electrochemical reaction that occurs at an electrode is proportional to the quantity of electric charge Q passed through an electrochemical cell. Thus, if the weight of a product of electrolysis is w, then Faraday's law states that

$$w = ZQ \qquad 2\text{-}3$$

where Z is the *electrochemical equivalent*, the constant of proportionality. Since Q is the product of the current I, in amperes, and the elapsed time t, in seconds,

$$Q = It \qquad 2\text{-}4$$

$$w = Z/I \qquad 2\text{-}5$$

According to the Faraday's law, the production of one gram equivalent of a product at the electrode, W_{eq} in a cell requires 96,487 coulombs. The constant 96,487 is termed the Faraday constant F. The coulomb is the quantity of electricity transported by the flow of one ampere for one second.

The Faraday constant represents one mole of electrons and its value can be calculated from

$$F = N_A e \qquad 2\text{-}6$$

where N_A is Avogadro's number (6.0225×10^{23} molecules mol^{-1}) and e is the charge of a single electron (1.6021×10^{-19} coulombs, C)

$$F = (6.0225 \times 10^{23})(1.6021 \times 10^{-19}) = 96{,}487 \text{ C mol}^{-1} \qquad 2\text{-}7$$

One equivalent, w_{eq} is that fraction of a molar (atomic) unit of reaction that corresponds to the transfer of one electron. For example, w_{eq} for silver is the gram atomic weight of silver, since the reduction of Ag^+ requires one electron. The deposition of copper from a Cu^{2+} salt involves two electrons, and the w_{eq} for Cu is (gram atomic weight of Cu)/2. In general,

$$w_{eq} = \frac{A_{wt}}{n} \qquad 2\text{-}8$$

where A_{wt}, is the atomic weight of metal deposited on the cathode, and n number of electrons involved in the deposition reaction.

From (2-3) and (2-5) it follows that when $Q = 1$ coulomb, or $Q = 1$ ampere second, then

$$w_{Q=1} = Z \qquad 2\text{-}9$$

Thus, the electrochemical equivalent of a metal M, $Z(M)$, is the weight in grams produced, or consumed, by one coulomb (one ampere second). The combination of equations 2-3 and 2-9 yields

$$w = w_{Q=1}\, Q \qquad 2\text{-}10$$

The value of Z, or $w_{Q=1}$, can be evaluated in the following way. Since 96,487 coulombs are required for the deposition of an equivalent of a metal, w_{eq}, from equation 2-3 it follows that

$$w_{eq} = 96{,}487\, Z \qquad 2\text{-}11$$

$$Z = w_{Q=1} = \frac{w_{eq}}{96{,}487} = \frac{w_{eq}}{F} \qquad 2\text{-}12$$

Since $w_{eq} = \frac{A_{wt}}{n}$, equation 2-8,

$$Z = \frac{A_{wt}}{nF} \qquad 2\text{-}13$$

Finally, from (2-3) and (2-13)

$$w = ZQ = \frac{A_{wt}}{nF}Q \qquad 2\text{-}14$$

The deposit thickness may be evaluated by considering the volume of the deposit. Since the volume of the deposit V is the product of the plated surface area, a and thickness (height) h, it follows that $h = {}^{V}\!/_{a}$. The volume of the deposit is related to the weight of the deposit w and the density of the deposit d, by ether relationship defining the density, $d = {}^{w}\!/_{V}$. Thus,

$$h = \frac{V}{a} = \frac{w}{ad} \qquad 2\text{-}15$$

In the case where it is necessary to calculate the time t (second, s) required to obtain the desired deposit thickness h, at a given current density, we introduced the Faraday's law, equation (14) into equation (15)and obtain

$$h = \frac{w}{ad} = \frac{ZQ}{ad} = \frac{ZIt}{ad}cm \qquad 2\text{-}16$$

$$t = \frac{had}{ZI}s \qquad 2\text{-}17$$

Schlesinger [37]

2.9 Current Efficiency

When two or more reactions occur simultaneously at an electrode, the number of coulombs of electricity passed corresponds to the sum of the number of equivalents of each reaction. For example, during deposition of Cu from a solution of cupric nitrate in dilute nitric acid, three cathodic reactions occur: the deposition of Cu (the reduction of cupric ions) and the reduction of both nitrate and hydrogen ions. The current efficiency CE of the jth, process, namely of any one of the simultaneous reactions, is defined as the number of coulombs required for that reaction, Q_j, divided by the total number of coulombs passed, Q_{total}

$$CE = \frac{Q_j}{Q_{total}} \qquad 2\text{-}18$$

An alternative equation defining current efficiency is

$$CE = \frac{w_j}{w_{total}} \qquad 2\text{-}19$$

where w_j is the weight of metal j actually deposited and w_{total} is that which would have been deposited if all the current had been used for deposition the metal j, Schlesinger [38].

Also, Schlesinger states that mechanical agitation of the bath makes possible the use of higher current densities and facilitates the formation of a more even deposit. Hence, whereas the mechanical properties are influence by the plating efficiency, the efficiency is control directly by current density and agitation.

2-10 Magnetic Properties

Electrodeposited materials, according Andricasos [39], offers several advantages as a process for magnetic-material deposition: Films can be electroplated with excellent magnetic properties and low stress at high rates of deposition; and plating cells are relatively inexpensive with a large installed manufacturing base. As a material additive process, electroplating allows for easier definition and control of small features such as yokes and pole tips in recording heads. Due to these advantages, electroplated soft magnetic materials such as NiFe and CoNiFe have been widely used as recording head materials for computer hard drive industries.

In the case of magnetic-MEMS/NEMS, the magnetic layer thickness can vary from a few nanometers to a few millimeters depending on the applications. Magnetic thin films must also have good adhesion, low-stress, corrosion resistance, and be thermally stable with excellent magnetic properties; Myung [40].

Myung also states that permalloy (81%Ni–19%Fe alloy) and nickel have thus far found the most utility in magnetic-Micro Electro-Mechanical Systems (MEMS), because the technologies necessary for depositing and micromachining them have been well-developed previously by the data storage industry. MEMS devices such as microactuators, sensors, micromotors, and frictionless microgears require the use of both hard and soft magnetic materials because electromagnetically actuated MEMS are more stable for high force and large actuation gap applications. Moreover, they are less susceptible to malfunction when subjected to adverse environments such as dust and humidity, and can be actuated with low-

cost voltage controllers; Judy [41], Judy [42], Judy [43], Ahn [44], Liakopoulos [45], and Chin [46].

2-11 Mechanical Properties

Sharpe [47] states that tensile tests have the advantage of uniform stress and strain fields, which is why they are used to determine mechanical properties at larger scales. However, they have disadvantages at smaller scales in that larger forces are required and specimen gripping may be difficult.

Johnson [48] compares bending and tension tests and notes that the former requires small forces and produce large displacements, whereas the latter require large forces with correspondingly small displacements. Bending, resonant, and membrane or bulge tests are inverse methods of determining mechanical properties. A simple or sophisticated model of a test structure is constructed, and independent stimulus is applied, and a response is measured. The parameters in the model are adjusted until the predicted response is sufficiently close to the result. For example, in simple Euler bending of a cantilever beam, the displacement, δ, is given by the familiar $PL^3/3EI$ where P is the applied force, L is the length of the beam, I is the area moment of inertia, and E is the desired Young's modulus. One measures d for a known P and computes E. There are two challenges in extracting mechanical properties of MEMS materials in this manner:

1. It is sometimes difficult to know the boundary conditions. Test specimens are likely released by an etching process, which may vary slightly among

specimens. The supporting boundaries are typically of a similar material with roughly the same thickness and stiffness.

2. The stress state at the point of failure can be very complicated. This is not so much an issue in determining modulus; one can match the shape of the test structure to a simple model. But, even in a simple cantilever beam test structures, failure occurs at stress concentrations. The effect of the size of the highly stressed region and stress gradient in it complicates matters, particularly for brittle materials.

Sharpe [49] states that tensile testing is not easy. Specimen preparation can be expensive and time-consuming. Gripping and alignment are fraught with potential errors.

2-12 Testing

Sharpe [50] states that there are three main challenges in testing small and thin specimens:

(1) Specimen preparation and handling

(2) Specimen gripping and pulling

(3) Strain measurement during the test

Metallic thick Ni film was tested at Johns Hopkins University for strain measured using an interferometric strain/displacement gage (ISDG); Lavan [51]. More experiments on materials/structures were recently reviewed by Sharp, Srikar and Spearing on various types of mechanical tests at the microscale—bend, resonance, Nanoindentation, and tension, etc; Sharpe [52] and Srikar [53]. Materials that have been characterized using the microtensile test include single crystal silicon, Yi [54]; polysilicon, Tsuchiya [55]; aluminum, Haque [56];

nickel, Rud [57] and Huang [58]. However, a complete set of experiments on NiFe alloy films has not been published.

The first generation tensile testing system used by Clark Atlanta University (CAU) is shown in Figure 2-6. The challenges experienced by CAU—using the MTS—were similar to those discussed by Sharpe listed above. As a result, the CAU team designed and constructed a new advance measurement system for characterizing and measuring thin-films. The measurement system designed and constructed was the Micro-Nano Test System (MNTS) shown in Figure 2-7. This system utilizes an atomic force microscope to measure displacement, i.e. strain, shown in Figure 2-8.

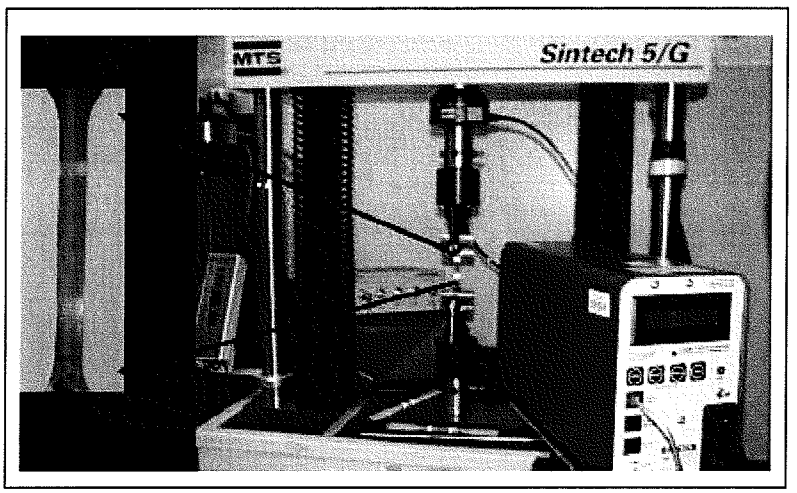

Figure 2-6: Mechanical Testing System (MTS) with Laser Extensometer...first generation tensile testing system used at CAU.

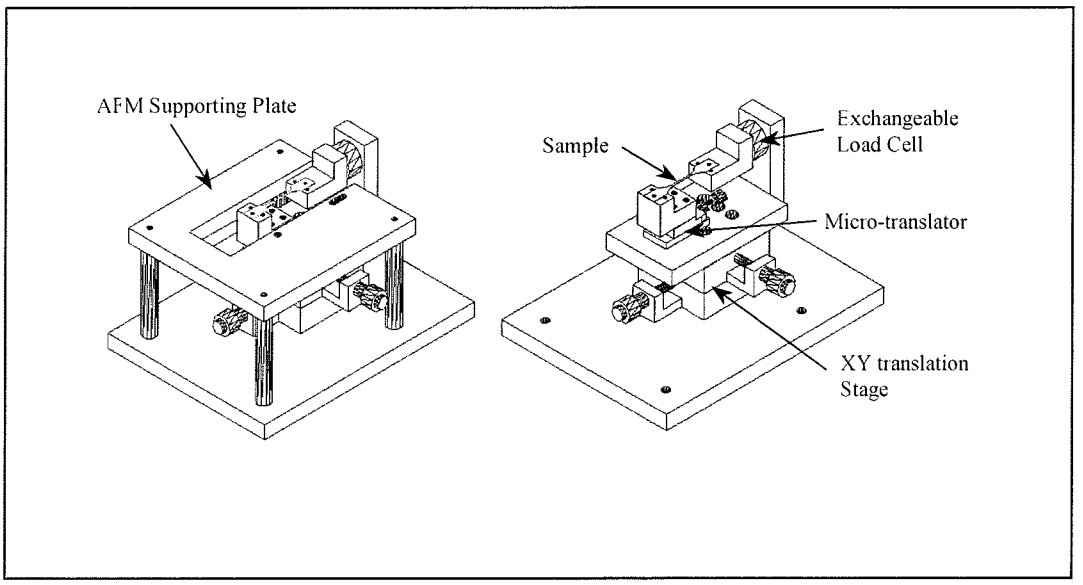

Figure 2-7: Advanced Micro-Nano Test System—Atomic Force Microscope (AFM) not shown.

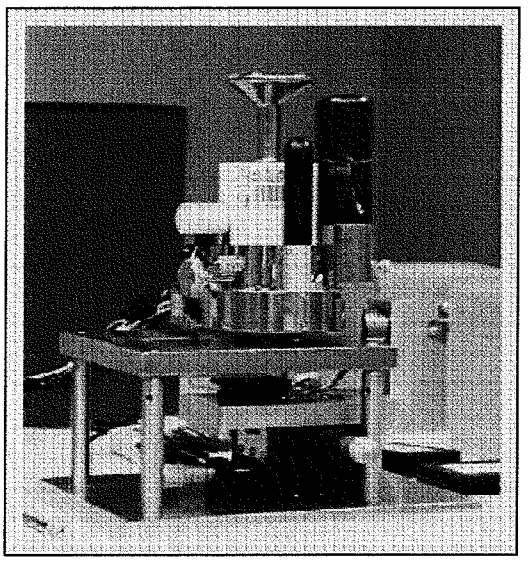

Figure 2-8: Advanced Micro-Nano Test System with Atomic Force Microscope

The Clark Atlanta University Team conducted tension studies of free standing electroplated NiFe (80/20) films of 10~30 micron thick at room temperature. The microstructures and crystalline structures of the electroplated NiFe were also studied as a function of various fabrication and annealing conditions, which can be correlated to the changes in thermal-mechanical properties. Calibration results of the advance MNTS is shown in Figure 2-9.

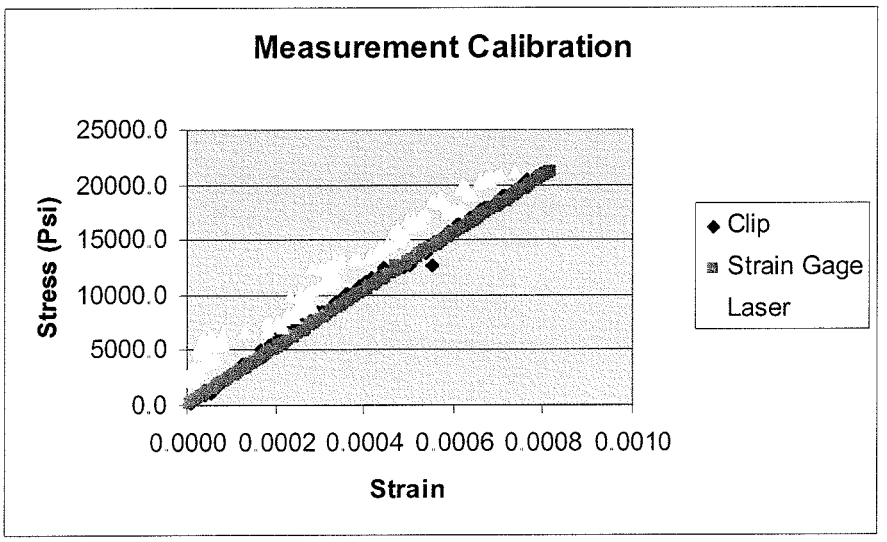

Figure 2-9: Measurement system calibration using clip on extensometer, strain gage, and laser extensometer.

The advantages of the new advance MNTS are:

- Direct Load/Displacement (Stress/Strain) Measurement
- Material Independency
- Adaptability to different geometries
- In-situ measurement
- Straight-forward data interpretation

2-13 References

[1] M. Schlesinger and M. Paunovic , *Modern Electroplating*, 4th Ed, p. 473, 2000

[2] P. C. Andricacos and N. Robertson, Future directions in electroplated materials for thin-film recording heads research, IBM Journal rd 425

[3] S. D. Leith, S. Ramli, and D. T. Schwartz, "*Characterization of Ni_xFe_{1-x} (0.10 < x < 0.95) Electrodeposition from a Family of Sulfamate-Chloride Electrolytes", Journal of Electrochemical Society,* ***146*** *(4), pp. 1431-1435 (1999)*

[4] W. P. Taylor, M. Schneider, H. Baltes, and M. G. Allen, *A NiFeMo Electroplating Bath for Micromachined Structures,* Electrochemical and Solid-State Letters, **2,** (12) 624-626 (1999)

[5] J. Mallinson, *Magneto-Resistive Heads-Fundamentals and Applications,* Academic Press, New York (1996)

[6] T. M. Liakopoulos, J. W. Choi, and C. H. Ahn, in *Proceedings of Transducers '97,* p. 485 (1997)

[7] W. Zhang and C. H. Ahn, in *Proceedings of the Solid State Sensor and Actuator Workshop,* p. 94 (1996)

[8] B. Wagner, M. Kreutzer, and W. Benecke, in *Proceedings of the IEEE Microelectromechanical Systems Workshop,* p. 183, IEEE, Piscataway, New Jersey (1992)

[9] C. H. Ahn, Y. J. Kim, and M. G. Allen, in *Proceedings of the IEEE Microelectromechanical Systems Workshop,* p. 1, IEEE, Piscataway, NJ (1993)

[10] H. Guckel, K. J. Skrobis, T. R. Christenson, J. Klein, S. Han, B. Choi, E. G. Novell, and T. W. Chapman, in *Proceedings of Transducers '91* (1991)

[11] C. H. Ahn, Y. J. Kim, and M. G. Allen, in *Proceedings of Tansducers '93,* p. 70(1993)

[12] J. A. Wright and Y. C. Tai, in *Proceedings of the Twelfth IEEE International Conference on Micro Electro Mechanical Systems,* p. 594, IEEE, Piscataway, NJ (1999)

[13] W. P. Taylor, M. G. Allen, and C. R. Dauwalter, in *Proceedings of the Solid State Sensor and Actuator Workshop,* p. 231 (1996)

[14] M. Schneider, R. Castagnetti, M. G. Allen, and H. Baltes, in *Proceedings of the IEEE Microelectromechanical Systems Workshop,* p. 151, IEEE, Piscataway, NJ (1995)

[15] S. Choi, S. Kawahito, Y. Matsumo, M. Ishida, and Y. Tadokoro, *Sens. Actuators A,* **55**, 121 (1996)

[16] C. Chung and M. Allen., "Measurement of Mechanical Properties of Electroplated Nickel-Iron Alloys," ASME International Mechanical Engineering Congress and Exposition. 1996

[17] S. D. Leith, S. Ramli, and D. T. Schwartz, "*Characterization of Ni_xFe_{1-x} (0.10 < x < 0.95) Electrodeposition from a Family of Sulfamate-Chloride Electrolytes", Journal of Electrochemical Society, **146** (4), pp. 1431-1435 (1999)*

[18] S. D. Leith, S. Ramli, and D. T. Schwartz, "*Characterization of NixFe1-x (0.10 < x < 0.95) Electrodeposition from a Family -Chloride Electrolytes", Journal of Electrochemical Society, **146** (4), pp. 1431-1435 (1999)*

[19] S. D. Leith, S. Ramli, and D. T. Schwartz, "*Characterization of Ni_xFe_{1-x} (0.10 < x < 0.95) Electrodeposition from a Family of Sulfamate-Chloride Electrolytes", Journal of Electrochemical Society,* ***146*** *(4), pp. 1431-1435 (1999)*

[20] S. D. Leith, S. Ramli, and D. T. Schwartz, "*Characterization of Ni_xFe_{1-x} (0.10 < x < 0.95) Electrodeposition from a Family of Sulfamate-Chloride Electrolytes", Journal of Electrochemical Society,* ***146*** *(4), pp. 1431-1435 (1999)*

[21] H. Guckel, T.R. Christenson, K. Skrobis, J. Klein, and M. Karnowsky, "*DESIGN AND TESTING OF PLANAR MAGNETIC MICROMOTORS FABRICATED BY DEEP X-RAY LITHOGRAPHY AND ELECTROPLATING",* Presented at the 7th International Conference on Solid State Sensors and Actuators, Japan, 13-15 May 1993

[22] H. Guckel, K. J. Skrobis, T. R. Christenson, J. Klein, S. Han, B. Choi, E. G. Novell, and T. W. Chapman, in *Proceedings of Transducers '91* (1991)

[23] J. W. Judy, R. S. Muller, and H. H. Zappe, "*Magnetic Microactuation of Polysilicon Flexure Structures"*, JOURNAL OF MICROELECTROMECHANICAL SYSTEMS, VOL. 4, NO. 4, DECEMBER 1995.

[24] H. Guckel, T.R. Christenson, K. Skrobis, J. Klein, and M. Karnowsky, "*DESIGN AND TESTING OF PLANAR MAGNETIC MICROMOTORS FABRICATED BY DEEP X-RAY LITHOGRAPHY AND ELECTROPLATING",* Presented at the 7th International Conference on Solid State Sensors and Actuators, Japan, 13-15 May 1993

[25] T. R. Christenson, T. E. Buchheit, D. T. Schmale, and R. J. Bourcier , *"Mechanical and metallographic characterization of LIGA fabricated nickel and 80%Ni-20%Fe Permalloy"*, Materials Research Society, 518, p. 185-190, (1998)

[26] S. D. Leith, S. Ramli, and D. T. Schwartz, *"Characterization of Ni_xFe_{1-x} (0.10 < x < 0.95) Electrodeposition from a Family of Sulfamate-Chloride Electrolytes", Journal of Electrochemical Society, **146** (4), pp. 1431-1435 (1999)*

[27] C. Chung and M. Allen., "Measurement of Mechanical Properties of Electroplated Nickel-Iron Alloys," ASME International Mechanical Engineering Congress and Exposition. 1996

[28] D. J. Macnaughton, J. *Iron Steel Inst.* (London), **109**, 409 (1924)

[29] P. K. Subramanyan and W. M. King, *Plating Surf. Finish.*, **69** (2), 48 (1982)

[30] S. F. Harty, J. A. McGeough, and R. M. Tulloch, Surf. Tech., **12**, 39 (1081)

[31] O. J. Kllingenmaier, *Plating*, **61**, 741 (1974)

[32] S. Yoshimura, S. Yoshihara, T. Shirakashi, and E. Sato, *Trans. Inst. Met. Finish.*, **73** (1), 31 (1995)

[33] C. Chung and M. Allen., "Measurement of Mechanical Properties of Electroplated Nickel-Iron Alloys," ASME International Mechanical Engineering Congress and Exposition. 1996

[34] M. Schlesinger and M. Paunovic , *Modern Electroplating*, 4th Ed, p. 473, 2000

[35] M. Schlesinger and M. Paunovic , Modern Electroplating, 4th Ed, p. 472, 2000

[36] M. Schlesinger and M. Paunovic , *Modern Electroplating*, 4th Ed, pp. 13-14, 2000

[37] M. Schlesinger and M. Paunovic , *Modern Electroplating*, 4th Ed, p. 15-16, 2000

[38] M. Schlesinger and M. Paunovic , *Modern Electroplating*, 4th Ed, p. 15, 2000

[39] P. C. Andricacos and N. Robertson, Future directions in electroplated materials for thin-film recording heads research, IBM Journal rd 425

[40] N.V. Myung, D. –Y. Park, B. –Y. Yoo, Paulo T. A. Sumodjo, *Development of Electroplated Magnetic Materials for MEMS,* Journal of Magnetism and Magnetic Materials 265, pp. 189-198, (2003)

[41] J.W. Judy, R.S. Muller, H.H. Zappe, IEEE J. Microelectromech. Syst. 4, p. 162, (1995)

[42] J.W. Judy, R.S. Muller, Sensors Actuators (Physical A), A, 53, p. 392, (1996)

[43] J.W. Judy, R.S. Muller, IEEE J. Microelectromech. Syst. 6, p. 249, (1997)

[44] C.H. Ahn, M.G. Allen, IEEE Trans. Ind. Electron. 45, p. 866, (1998)

[45] T.M. Liakopoulos, M. Xu, C.H. Ahn, Technical Digest Solid-State Sensor and Actuator Workshop, Vol. 19, Hilton Head Island, SC, USA, (1998)

[46] T.S. Chin, J. Magn. Magn. Mater. 209, p. 75 (2000)

[47] W. N. Sharpe, Jr., "*Tensile Testing at the Micrometer Scale (Opportunities in Experimental Mechanics)*", Experimental Mechanics: Tensile Testing at the Micrometer Scale, **43**, 228-237 (2003)

[48] G. T. Johnson, R. T. Howe, "*Material Characterization for MEMS: a Comparison of Uniaxial and Bending Tests*", Proceeding of the SPIE, **3874**, 94-101,(2000)

[49] W. N. Sharpe, Jr., "*Tensile Testing at the Micrometer Scale (Opportunities in Experimental Mechanics)*", Experimental Mechanics "Tensile Testing at the Micrometer Scale, **43**, 228-237, (2003)

[50] W. N. Sharpe, Jr., and A. McAleavey "*Tensile Properties of LIGA Nickel*", Proc. SPIE **3512**, 130–7, (1998)

[51] D.A. Lavan, W.N. Sharpe, "Tensile testing of Microsamples," Experimnental Mechanics, **39**, 210-216 (1999)

[52] W. N. Sharpe, Jr., "Murry Lecture Tensile Testing at the Micrometer scale: Opportunities in Experimental mechanics", Experimental Mechanics, **43**, 228-237 (2003)

[53] V.T. Srikar and S. M. Spearing, "a Critical Review of Microscale Mechanical Testing Methods Used in the Design of Microelectromechanical Systems", Experimental Mechanics, **43**, 238-247 (2003)

[54] T. Yi, L. Li, and C.J. Kim, "Microscale Material Testing of Single Crystalline Silicon: Process Effects on Surface Morphology and Tensile Strength", Sensors, and Actuators, **A83**, 172-178 (2000)

[55] T. Tsuchiya, O. Tabata, J. Sakata, and Y. Taga, "Specimen Size Effect on Tensile Strength of Surface-Micromeachined Polycrystalline Silicon Thin Films," Journal of Microelectromechnicsal System, **7** (1), 106-113 (1998)

[56] M.A. Haque and M.T.A. Sif, "In-Situ Tensile Testing of Nanoscale Specimens in SEM and TEM," Experimental Mechanics, **42** (1), 123-128 (2002)

[57] J. A. Rud, D., Josell, F. Spaepen, and A.L. Greeer, "A New Method for Tensile Testing of Thin Films," Journal of Material Research, **8** (1), 112-117 (1993)

[58] H. Huang and F. Spaepen, "Tensile Testing of Free-Standing Cu, Ag, and Al Thin Films and Ag/Cu Multilayers," Acta Materialia, **48**, 3216-3269 (2000)

CHAPTER 3

EXPERIMENTAL PROCEDURES

In this chapter the experimental procedures are outlined and discussed. The processes begin by preparing a silicon wafer for the electrodeposition process. Once the silicon wafer has been prepared, five $Ni_{80}Fe_{20}$ dog-boned test specimens are fabricated through a chemical electroplating process; this process is described in section 3.1. In section 3.2, the design and build of the new Micro/Nano Scale Test System is discussed along with the mechanical testing process and the data acquisition. In chapter 4, a 2^k Factorial Statistical Analysis DOE and Regression Analysis are conducted using the data obtained in chapter 3. Mathematical models describing the boundary conditions', used in the chemical electroplating process, influences on the mechanical properties are derived in chapter 4. In chapter 5, surfaces profiles, plating informality, and experimental findings are discussed.

3.1 Fabrication

The fabrication process for the $Ni_{80}Fe_{20}$ test specimens are generated in two fabrication processes: (1) The Silicon Wafer and (2) The actual nickel iron electroplating.

3.1.1 Wafer Preparation

The fabrication procedure for plating NiFe onto a Si wafer:

I. A 4-inch Si wafer is clean using a DI water rinse all dust particles from the face of the wafer. The wafer is then dried using a N_2 gun.

II. Using a Plasma Enhanced Chemical Vapour Deposition (PECVD) machine, a l μm-thick layer of SiO_2 onto the silicon wafer.

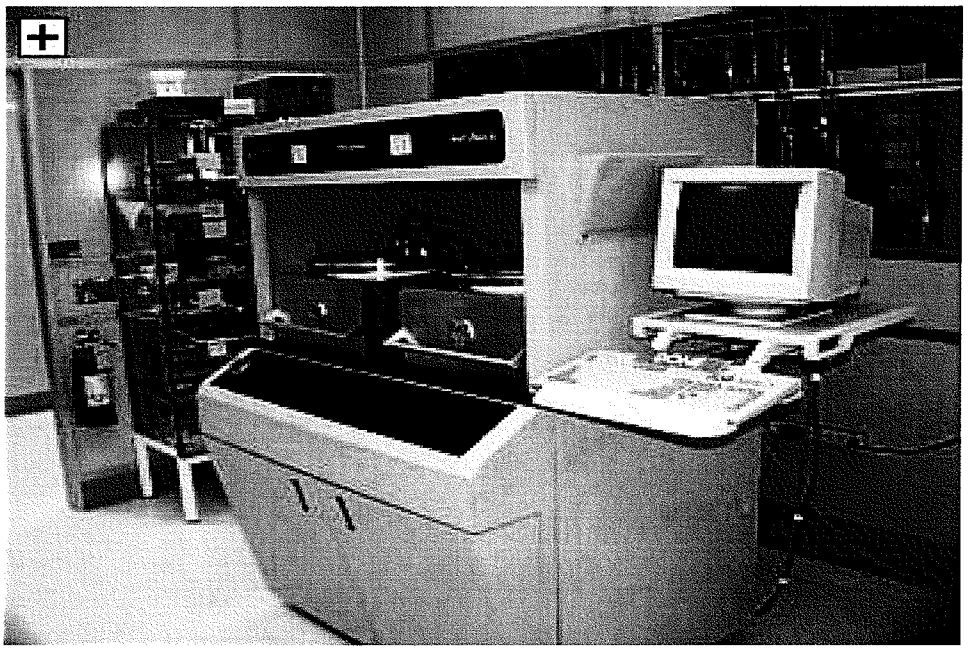

Figure 3-1: Plasma Enhanced Chemical Vapour Deposition (PECVD)—Georgia Tech Clean Room.

Figure 3-2: The PECVD has two chambers, each capable of holding six wafers. One is intended for silicon nitride deposits and the other chamber is intended primarily for silicon dioxide depositions.

III. Using a DC Sputter/Evaporator—a sandwich deposit consisting of Ti/Al/Ti with thickness 300 Å, 1.5μm, and 300 Å respectively, is sputtered onto the SiO_2 silicon wafer.

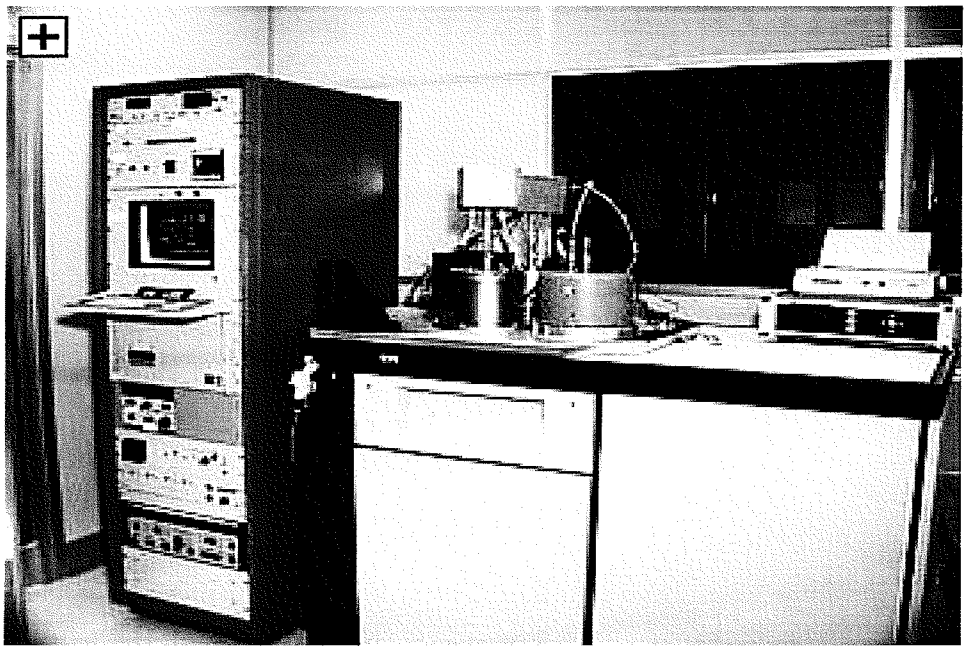

Figure 3-3: The DC Sputter (Georgia Tech Clean Room) consists of an electronic stack and machine housing. It is used to coat samples with metals. The DC Sputter can be used to deposit virtually any metal.

IV. A liquid-form of polymer is placed on the wafer substrate and placed onto a spinner/hotplate, shown in Figure 3-4. The spinner is programmed for 850-rpm/250/10-sec (850-rpm at an accelerated rate of 250-rpm per second for 10 seconds) which uniformly distributes liquid polymer over the entire wafer; resulting in a polymer layer of approximately 50μm thick. To solidify the polymer, the wafer substrate is then baked for 15 minutes at 120°C; in a process is called Negative Resist.

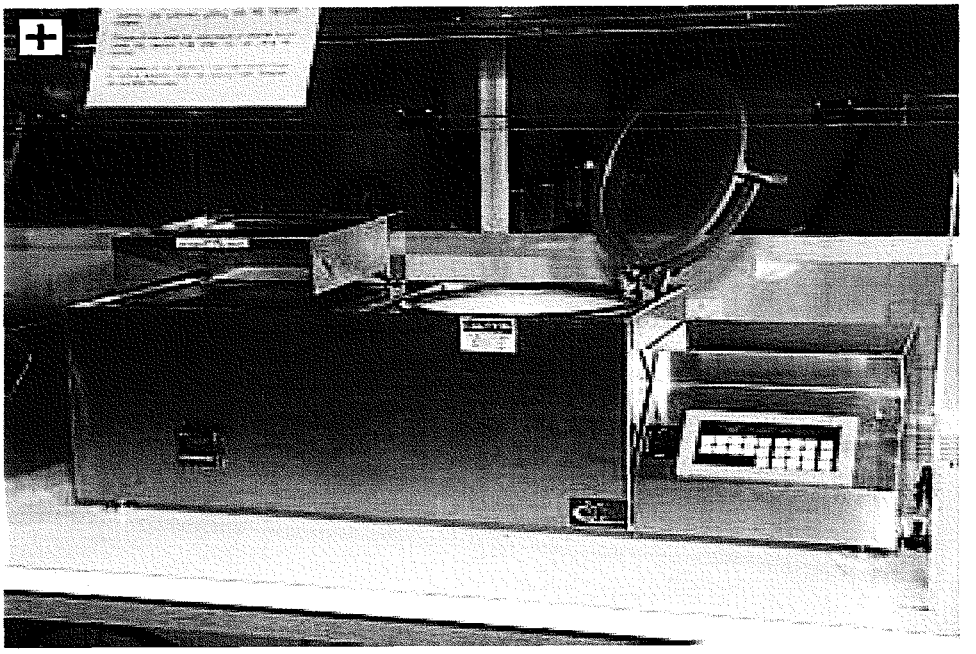

Figure 3-4: CEE Model 100CB Spinner/ Hotplate. Spin coaters are used to distribute photoresist in a thin uniform layer by spinning the substrate. The hotplate is designed for curing photoresist.

V. A mold—containing the designed specimen configuration—is placed over the wafer and exposed to a ultra-violet (UV) light source. The energy flux of this UV-light source is $10mV/cm^2$ for 200 seconds, which is equivalent to 2000 mJ/cm^2. The wafer substrate is then baked for 3 minutes (post-bake). Post-bake allows the polymer to create cross-links that strengthen the polymer.

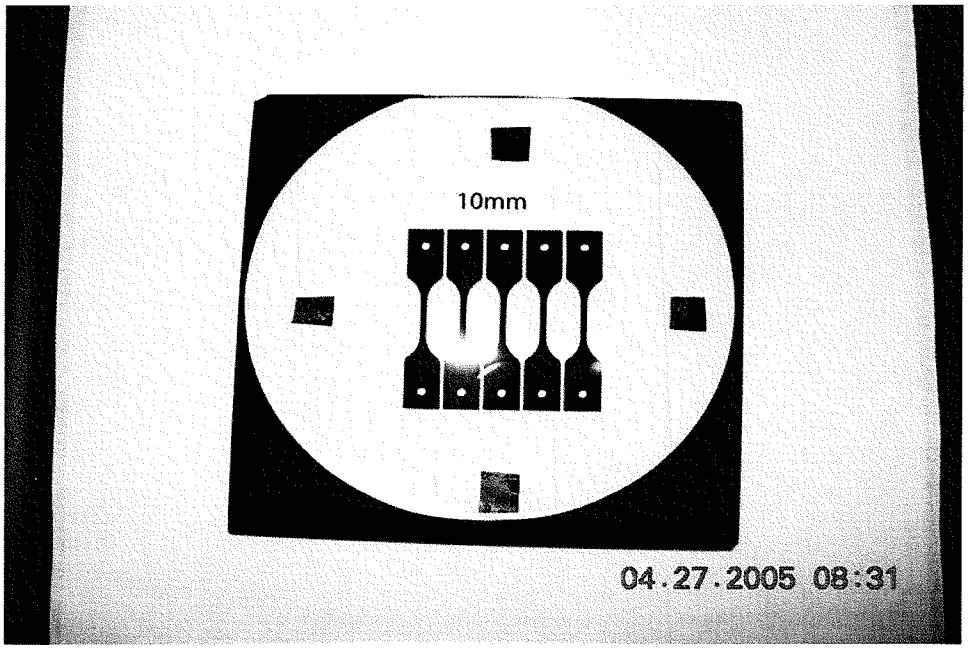

Figure 3-5: Specimen design mold. The mold contains the design for five copper seed layers.

Note that the mask for the mold is designed and developed prior the wafer preparation. Based on the test structures design; an AutoCad drawing is prepared. To ensure a high definition resolution transparency the drawing is printed in the print shop.

VI. After post-baking, the polymer color changes from a reddish brown to a dull gold. The wafer substrate is then placed in a polymer resist solution (Developer RD6) and hand agitated for several minutes to remove residual polymer that was unexposed by the UV-light. The wafer substrate is then examined under a microscope, ensuring that all unexposed polymer residue has been removed. Now the wafer substrate is ready for electroplating.

3.1.2 Electroplating Protocol

I. A silicon wafer substrate, containing five dog-bone shaped specimen seed layers, is washed with DI water and air-dried using compressed nitrogen.

II. The silicon wafer substrate is attached to a Plexiglas plate, which is used to support the silicon wafer and to prevent electroplating on the back of the substrate.

III. The negative terminal of the power supply is connected to the silicon wafer substrate—seed layers (cathode); and the positive terminal of the power supply is connected to a nickel alloyed bar (anode).

Note: The typical electroplating cell consists of the anode, cathode, aqueous-metal solution, and a power supply. In the simplified example shown in Figure 3-7, the sacrificial anode is made of nickel, the cathode is made of another conductive material—in our case copper, and the aqueous-metal solution consists of nickel (Ni^{2+}), hydrogen (H^{+}), and sulfate ions (SO_4^{2-}). When the power supply is turned on, the positive ions in the solution are attracted to the negatively biased cathode. The nickel ions that reach the cathode gain electrons and are deposited, or plated onto the surface of the cathode (copper seed layer) forming the electro-deposit. Simultaneously, nickel is electrochemically etched from the nickel anode, to produce ions for the aqueous solution and electrons for the power supply. Hydrogen ions that also gain electrons from the cathode form bubbles of hydrogen gas. The formation of hydrogen gas is undesirable since it lowers the plating efficiency (i.e., only a fraction

of the total current is used to form the electro-deposit) and the bubbles can obstruct the deposition of the intended electro-deposit.

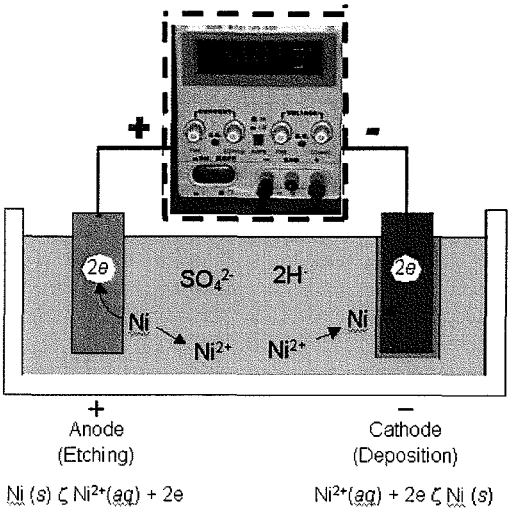

Figure 3-6: The CAU Electroplating setup with constant current source.

IV. The electrical leads are sealed with tape to prevent shorting out the electrical circuit; the anode (nickel alloyed bar), and cathode (test specimen seed layers) are then place in an iron electrolyte solution approximately 3.5 cm apart.

Note: The iron electrolyte solution is chemically designed to cultivate a nickel iron alloy—composition: 80% nickel and 20% iron by weight—onto the copper seed layer of the silicon wafer substrate.

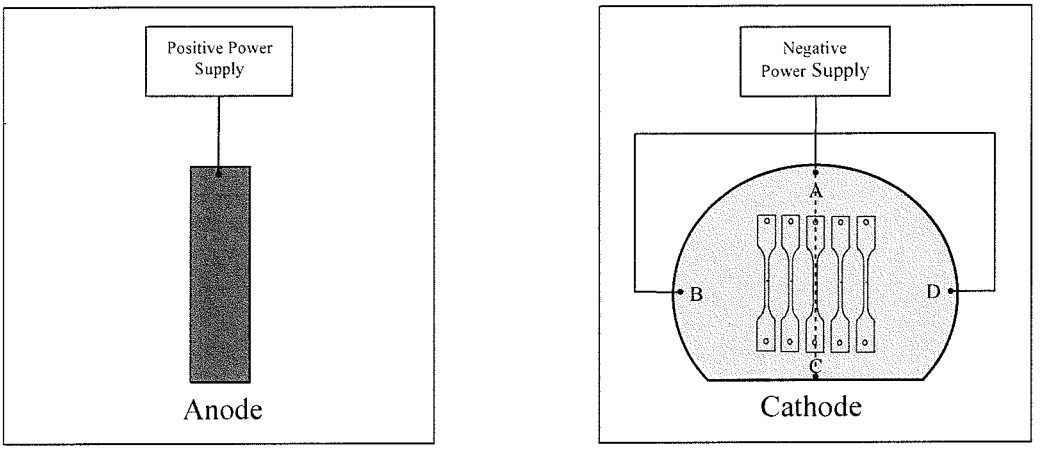

Figure 3-7: The anode consists of a nickel alloyed bar—98% pure nickel—is connected to the positive terminal of the power supply. The cathode consists of a silicon wafer substrate—containing five dog-bone shaped specimen seed layers—connected to the negative terminal of the power supply. The electrical lead is connected only at the top of the nickel alloyed bar.

To fabricate the microstructures by electroplating, a conductive plating base or seed layer (in our case, sputtered nickel) and a means to pattern the electro-deposit (photolithography#5 and #6) are needed. Typically, the electro-deposit is patterned by an additive process (selective deposition) instead of a subtractive process (etching). Since the localized electro-deposition rate is proportional to the localized current density, a uniform current density over the entire seed layer is needed to obtain an electro-deposit having a uniform thickness. To achieve selective deposition, however, portions of the seed layer are covered with an insulating masking material that makes the current density in its proximity non-uniform. The nickel plating solution is shown in Table 3-1.

Table 3-1: 80-20 Nickel plating solution.

Nickel Plating Solution	
Material	**Quantity**
Nickel Sulfate	200 g/L
Nickel Chloride	5 g/L
Boric Acid	25 g/L
Ferrous Sulfate	8 g/L
Saccharin	3 g/L

Conditions: T = 25 – 50 °C, current density = 5 – 10 mA/cm^2, and agitation = 0 – 300 rpm duty cycle

V. The cathode and anode remain in the iron electrolyte solution (nickel iron bath) under a constant current, bath temperature, and agitation for approximately four hours. At the end of the four hours, five nickel iron test specimens between 25 μm and 75 μm thick—depending on the plating parameters—are cultivated on the copper seed layers of the silicon wafer.

Figure 3-8: A Si wafer containing five electrodeposited NiFe test specimens.

VI. The wafer is then prepared for chemical etching to remove the test specimens:

a. First, the wafer is rinsed and dried using DI-water and compressed nitrogen respectively.

b. Second, the wafer is placed in 100% acetone to remove the remaining polymer layer from the wafer; rinsed and dried again used DI-water and compress nitrogen.

c. Third, after the polymer layer has been removed, the wafer is then placed in a blue etching solution to remove the copper seed layer from the wafer; and repeat cleaning.

VII. The aluminum and titanium layers are etched from the wafer with 10% HF (Hydrofluoric) acid solution—the HF etching process takes approximately five hours—the results are five nickel iron dog-bone test specimens.

VIII. The five dog-bone test specimens are then rinsed and dried using DI water and compressed nitrogen; they are now ready for mechanical testing.

3.2 Testing

Once the test specimens have been fabricated, samples are submitted to verify the chemical composition of the material. The test specimens are to contain 80% nickel and 20% iron. Randomly, the surface profile of the test specimens is examined for uniformity. Finally, testing is conducted to determine the mechanical properties of the test specimens.

3.2.1 Mechanical Properties Testing Protocol

Prior to mechanical testing, random NiFe specimens are selected and test for material composition. The desired composition is 80% Ni and 20% Fe.

I. Using a Noran EDS (Energy Dispersive Spectrometer) System, an analysis is conducted to determine the exact composition of the alloy.

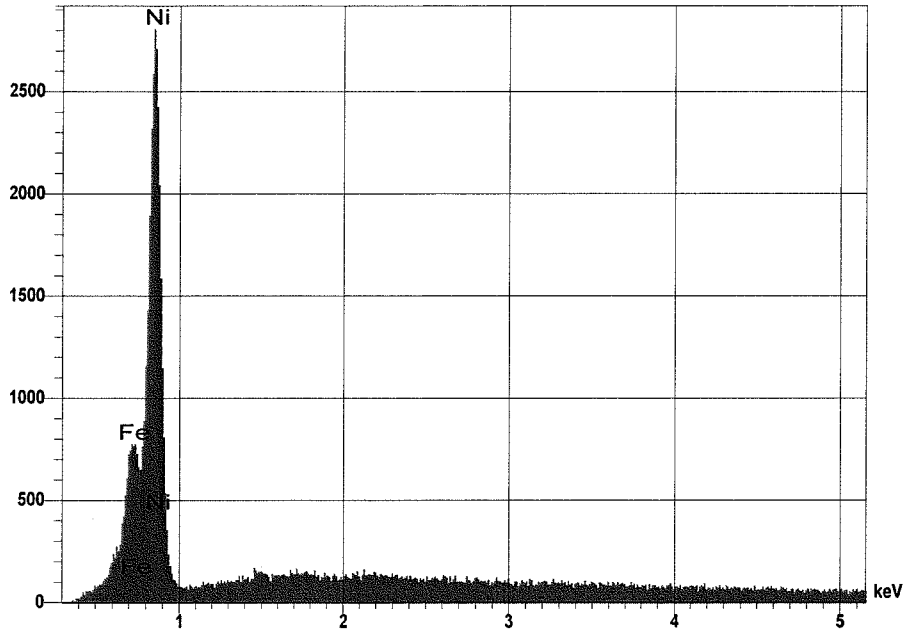

SpectraPlus Report

Elt	XRay	Int	Error	K	Kratio	W%	A%
Fe	Ka	129.0	1.4665	0.2099	0.2147	18.23	18.99
Ni	Ka	309.0	2.2694	0.7901	0.8083	81.77	81.01
Total				1.0000	1.0230	100.00	100.00

Figure 3-9: EDS (Energy Dispersive Spectrometer) composition printout for electroplated NiFe.

I. The thickness of the NiFe test specimen is measured—by hand using a micrometer—at three distinct locations along the gauge length. If the three measured thickness are within 10% of each other, then the gauge thickness is the arithmetic average of the three measurements. Otherwise, two additional measurements are taken.

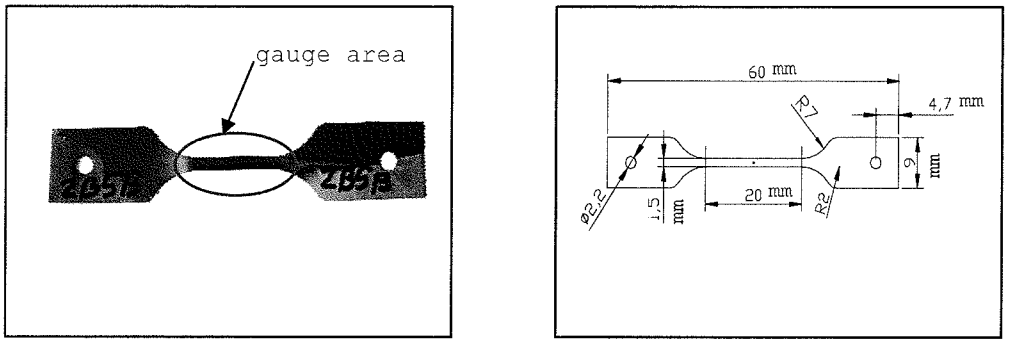

Figure 3-10: Actual NiFe test specimen; and schematic drawing of a dog-bone shape NiFe test specimen depicting dimensions.

III. Mechanical Tensile tests are conducted using a Micro/Nano-Scale Mechanical Testing System that was designed and built at Clark Atlanta University (CAU). The test specimen is placed in the specimen holder slot on the Micro/Nano Scale Mechanical Testing System, and clamped down by the three screws on both sides. The micro translator is adjusted to remove all the excess slack from the test specimen.

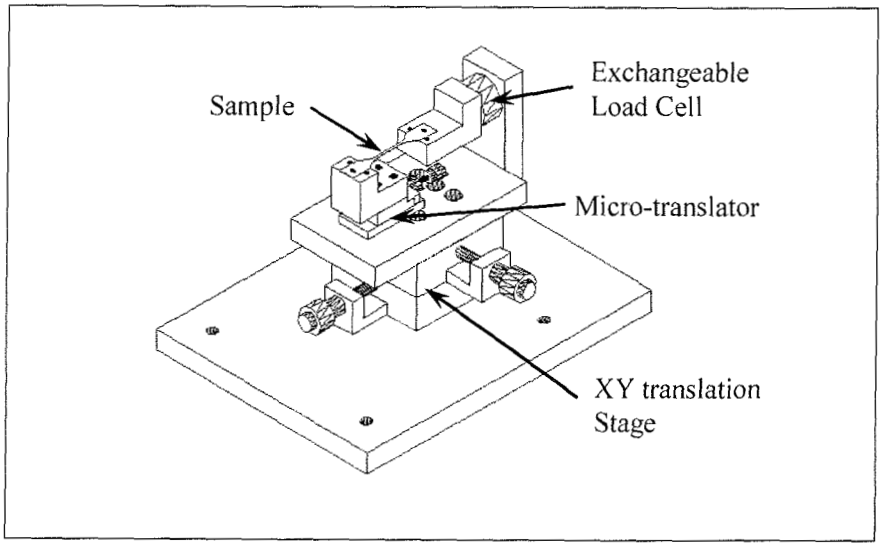

Figure 3-11: Schematic of CAU Micro/Nano Scale Testing System.

IV. The specimen is loaded linearly, up to approximately ten pounds, and then unloaded. This loading/unloading process is repeated two times, and the third time the test specimen is loaded until failure.

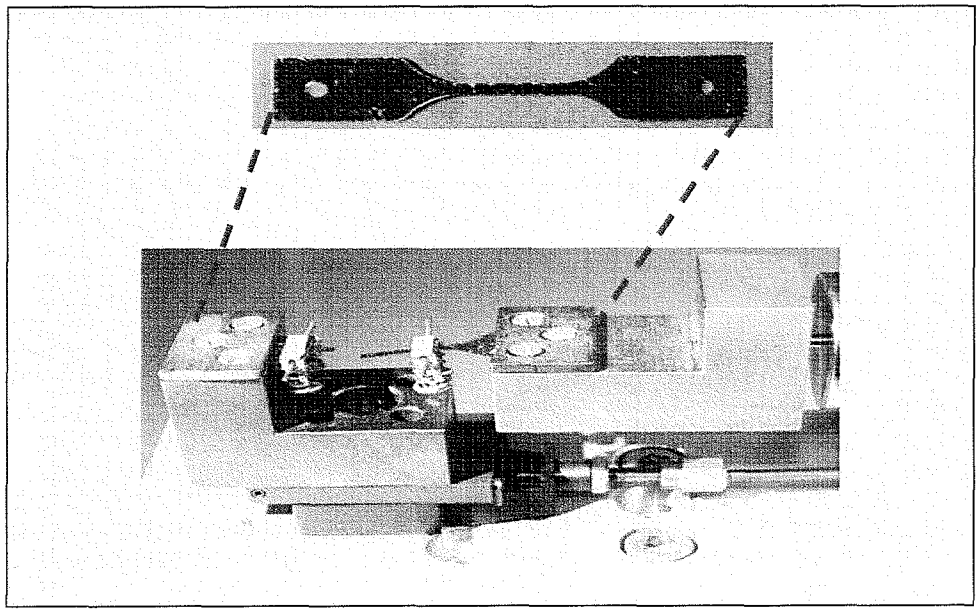

Figure 3-12: An actual failed NiFe test specimen depicted in the Micro/Nano Scale Testing System.

3.2.2 Data Acquisition

The Micro/Nano Mechanical Testing System, along with a laser extensometer provides inputs into a Dasylab software application package that records load verses strain. The Micro/Nano Mechanical Testing System transmits the load in the form of volts; and the laser extensometer is responsible for capturing the strain. The stress verses strain curves are calculated from this data.

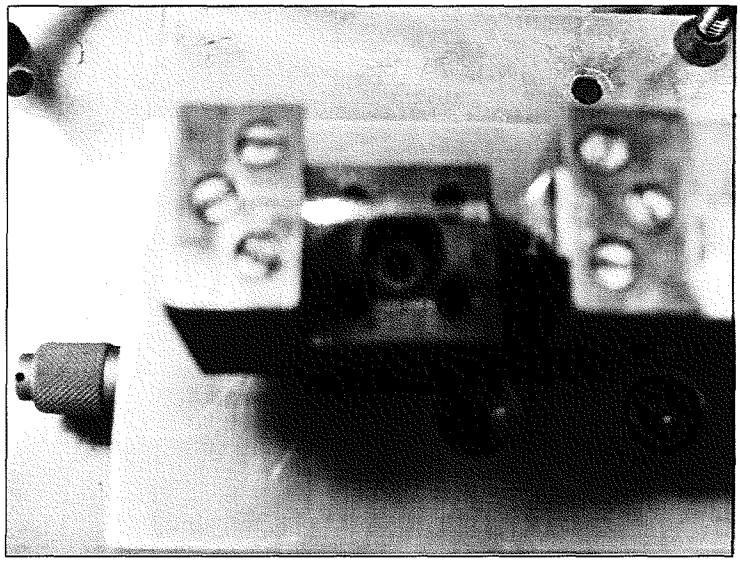

Figure 3-13: Laser Extensometer aligned along test specimen.

I. Set the distance between the laser extensometer face plate and the specimen surface should be between 12 and 15 inches—304 and 381 millimeters respectively.

II. Connect the laser extensometer to the modem by attaching the phone cable to the extensometer analog port and then to the modem box.

III. Set the laser extensometer parameters: scroll down to the desired parameters and (holding the scroll and select buttons simultaneously) holding the select buttons until all desired parameters are selected.

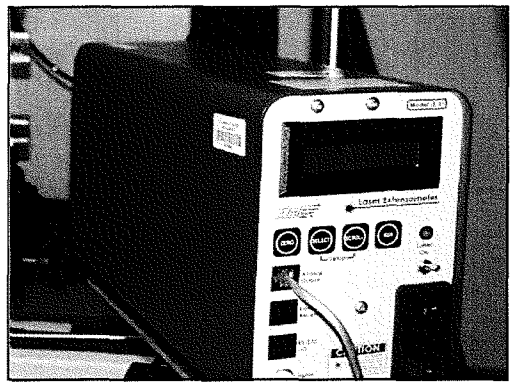

Figure 3-14: Laser Extensometer setup display buttons.

Note: For our setup, all measurements are in millimeters; target distance is equivalent to measured distance; and 5 volts equals 2 millimeters.

IV. Press run to load and record the chosen perimeters.

Dasylab Application Setup

I. Open the cell monitor of Dasylab; select the 100 lb load cell from the file menu and click play.

II. Verify initial display for calibration. The load should read zero and the displacement reading should corresponds the reading on the laser extensometer.

Note: If initial display is incorrect; then check the following:

i. Grounding of the system; ground the motor by attaching alligator clips to the metal mount of the Micro/Nano-Scale Testing System and the metal plate of the extensometer (this should reduce load to pretension load).

ii. Tension of the test specimen; remove all slackness from the specimen by adjusting the micro-translator.

III. Create data file and specimen name by selection module write00 button; create folder and specimen's name. The Dasylab Application setup is now complete.

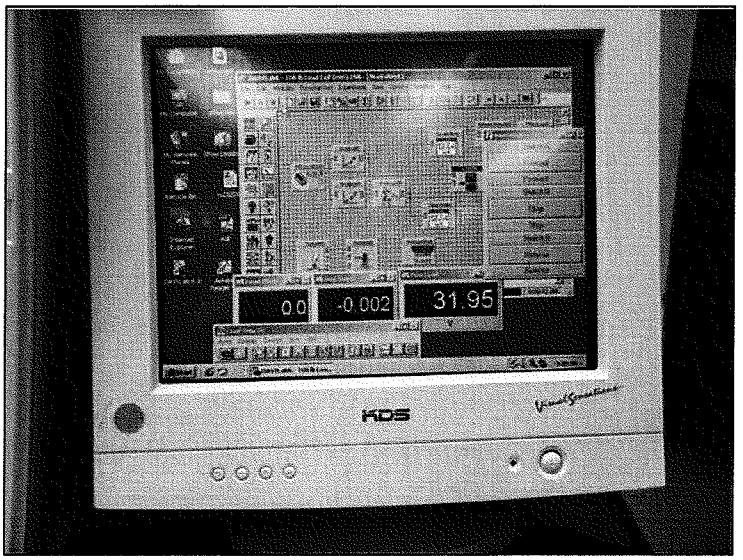

Figure 3-15: Dasylab Application setup and display.

I. Zero out the extensometer by pressing the zero-button on the extensometer.

II. Obtain the specimen gauge length by pressing the zero-button again on the laser extensometer. This is the distance between the two metallic tape strips placed on the specimens), the gauge length should be between 7 and 10 mm.

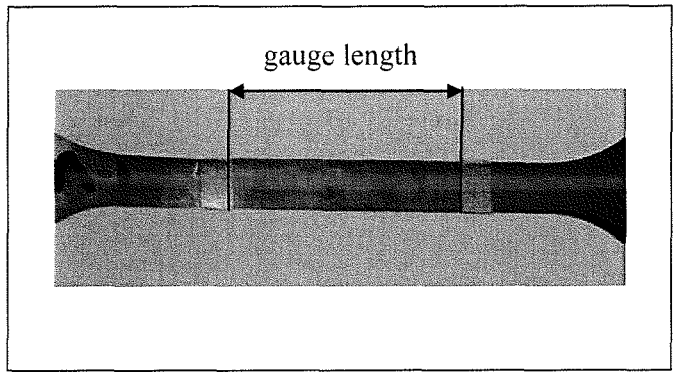

Figure 3-16: Test specimen aligned with laser...gauge length is the distance between the two metallic tape strips.

III. Initialize the displacement to zero; this is achieved by pressing the zero-button of the laser extensometer again (three times).

Note: If this number is negatively large, or has large fluctuation then minor adjustments need to be made to the extensometer positioning or specimen.

IV. Begin the loading by pressing play. The initial load shown should be small—represents the applied pretension load—the displacement value should correspond to the extensometer reading.

Note: The displacement value should not fluctuate very much and if displacement value equals 2.99 then the saturation point has been reached—test specimen must be re-taped to reduce the distance between the two metal strips (gauge length).

V. Increase tension loading to approximately 10 lb (pressing forward/stop on Dasylab application).

VI. Reverse load back down to zero (pressing reverse/stop on Dasylab application)—this corresponds to first load; repeat this process (also rename specimen to correspond to each upload).

VII. Finally, load test specimen to failure.

VIII. Calculation: when calculating the Young's Modulus (E), select the three distinct uploading for the specimen. Identify the linear section in the graphs that are the same for the three loadings; calculate the slope for the three graphs; take average to obtain the Young's Modulus.

Note:

1. Strain, $\varepsilon = \Delta l/l$,
2. Stress, $\sigma = F/A$,
3. Young Modulus, $E = \sigma\varepsilon$
4. Young Modulus, $E = \Delta\sigma/\Delta\varepsilon$

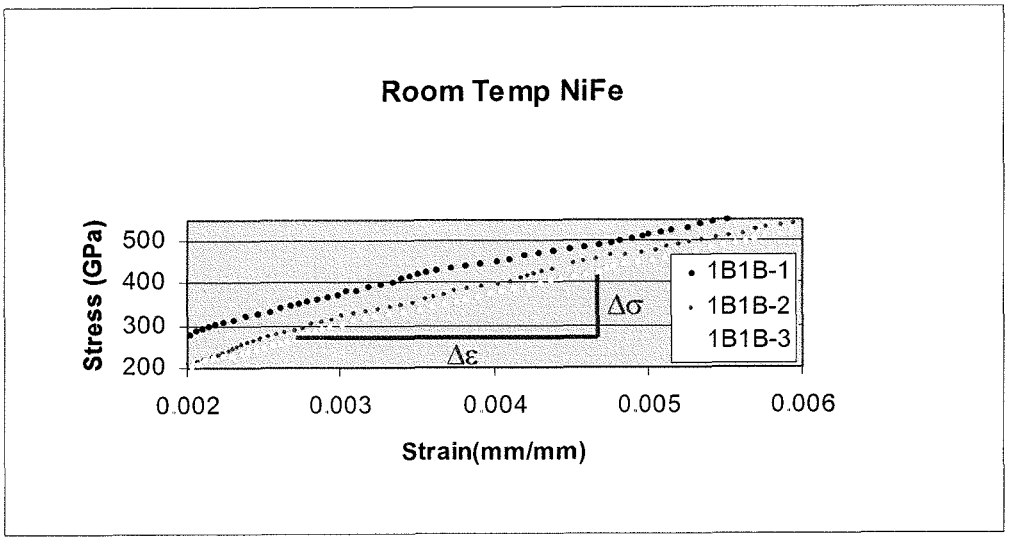

Figure 3-17: Actual stress-strain curve for a NiFe test specimen. All three curves represent the same specimen—two uploads and finally load to failure. E is the slope = $\Delta\sigma/\Delta\varepsilon$.

CHAPTER 4

STATISTICAL ANALYSIS

4.1 Preliminary Study

A magnet is used in a generator to convert the mechanical energy into electrical energy. For the MEMS generator a material having magnetic properties and the flexibility to fabricate into complex geometries is required. Electro-deposited $Ni_{80}Fe_{20}$ material has these characteristics. However, there are not any published data regarding the mechanical properties of $Ni_{80}Fe_{20}$.

In this research, X-Ray Diffraction (XRD) was utilized to examine the crystalline structure and residual stresses in electroplated metal films; the X-ray diffraction data of the $Ni_{80}Fe_{20}$ films as deposited, annealed at 500 and 700°C are shown in Figures 4-1 and 4-2. The change of d-spacing between these materials demonstrates that the inherent stress changes among the materials. The change of full width half maximum (FWHM) and the shifting of the peaks demonstrated the change of dislocation densities and grain size. Due to the limitation of the current setup on the X-ray detector, no intrinsic stresses in the film have been quantified. Since there is no standard process design and fabrication (PDF) data for the $Ni_{80}Fe_{20}$, extensive research is needed to study the crystalline structures of this material and the corresponding crystalline structure and inherent stress level of the electroplated $Ni_{80}Fe_{20}$ films, Xue [1].

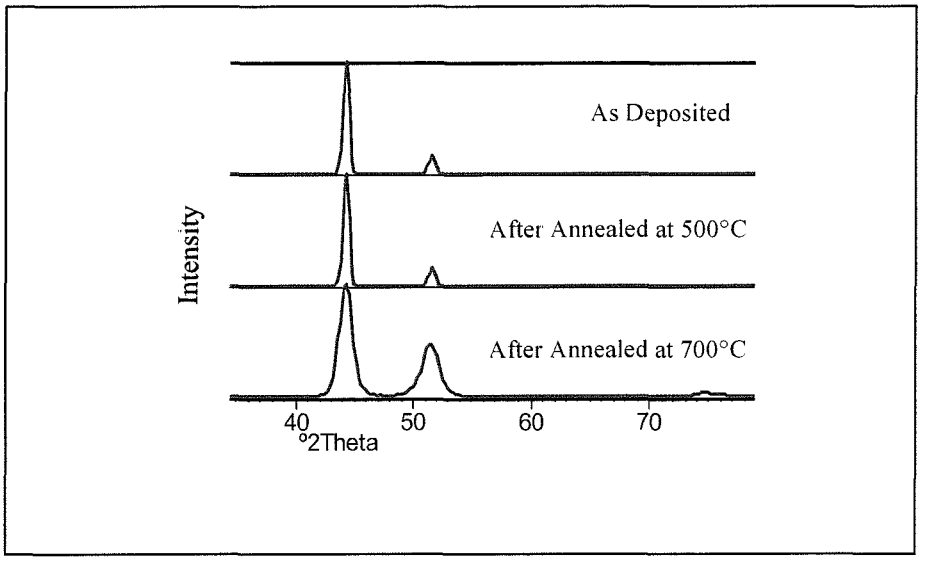

Figure 4-1: The X-ray diffraction pattern of electroplated $Ni_{80}Fe_{20}$ film, as deposited, after annealed at 500 °C and 700 °C.

Table 4-1: The X-ray diffraction data of bulk $Ni_{80}Fe_{20}$, electroplated NiFe film, as deposited, after annealed at 500°C and 700°C.

	Pos. [°2Th.]	FWHM [°2Th.]	d-spacing [Å]	Rel. Int. [%]
Bulk $Ni_{80}Fe_{20}$	43.8611	0.9840	2.06419	100.00
	51.3926	1.1808	1.77799	75.32
	75.4181	1.2000	1.25937	13.05
As Deposited	44.0075	0.5904	2.05766	100.00
	51.2934	0.7872	1.78119	16.08
	75.5442	0.7200	1.25758	0.15
Annealed at 500°C	43.6604	0.7872	2.07321	100.00
	50.9676	0.9600	1.79033	21.35
Annealed at 700°C	44.1170	1.3776	2.05280	100.00
	51.2136	1.3776	1.78378	38.80
	74.3780	0.9600	1.27439	6.08

Next the surface morphology of $Ni_{80}Fe_{20}$ was investigated. The changes in surface morphology were characterized using an Atomic Force Microscope (AFM). The surface morphology of the electroplated $Ni_{80}Fe_{20}$ films, as deposited and after annealed, is shown in Figures 4-2 and 4-3. The $Ni_{80}Fe_{20}$ film as deposited shows a

smooth surface with regularly distributed spikes extruding out of the surface. The $Ni_{80}Fe_{20}$ films annealed become rough and form huge hillocks on surface. It is believe that the changes in morphology in electroplate $Ni_{80}Fe_{20}$ might be caused by the recrystallization of the film and the release of inherent stresses in the films during annealing.

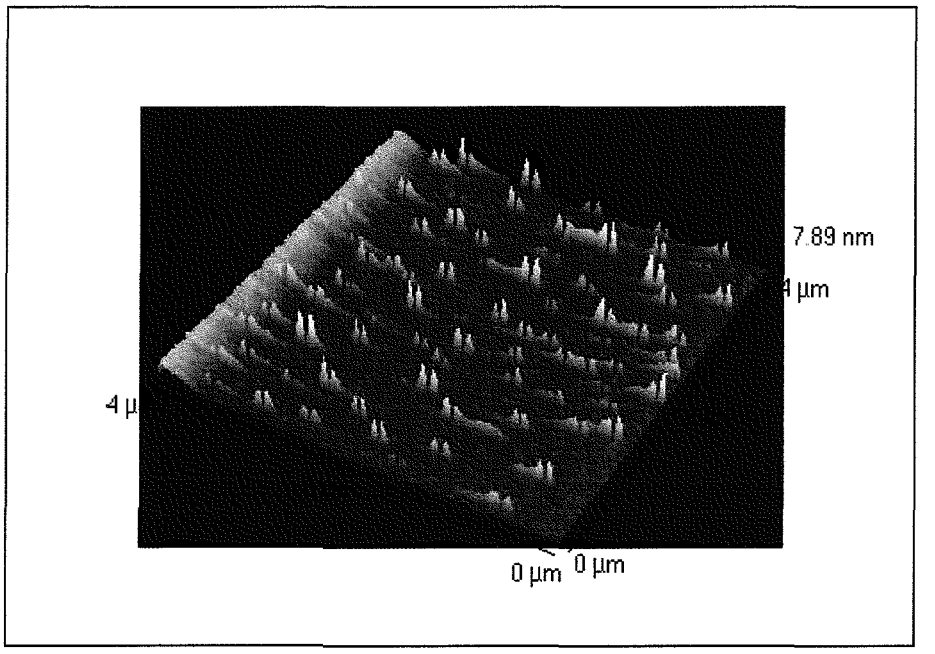

Figure 4-2: AFM micrograph of electroplated $Ni_{80}Fe_{20}$ as deposited (4x4 μm^2).

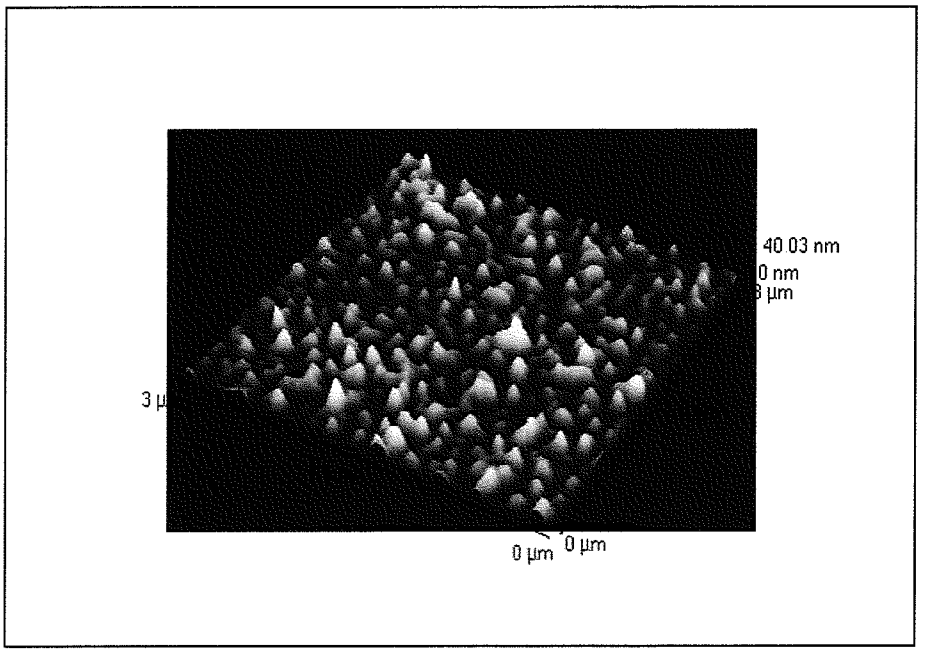

Figure 4-3: AFM micrograph of electroplated $Ni_{80}Fe_{20}$ after annealed at 500°C for 5 hours (3.0 x 3.0 μm^2).

Based on literature review it is well understood that the surface boundary conditions play a vital role in affecting the grain structure which in turns affects the mechanical properties of electrodeposited $Ni_{80}Fe_{20}$. According to Leith, agitation and current density are key electrolyte's boundary conditions influencing the mechanical properties of electrodeposited $Ni_{80}Fe_{20}$; Figures 4-4 and 4-5 show the effect that agitation and current density have on concentration and efficiency. Thus to establish a baseline, preliminary studies of electrodeposited $Ni_{80}Fe_{20}$ was conducted varying only agitation and current density (temperature fixed at room temperature i.e. 25 °C) as the fundamental baseline boundary conditions. The study began by fabricating large $Ni_{80}Fe_{20}$ dog-bone test specimens (shown in Figure 4-6), using CAU's MTS system

shown in Figure 4-7. Test results are shown in Table P1, and the corresponding stress strain curves are shown in Figure 4-8.

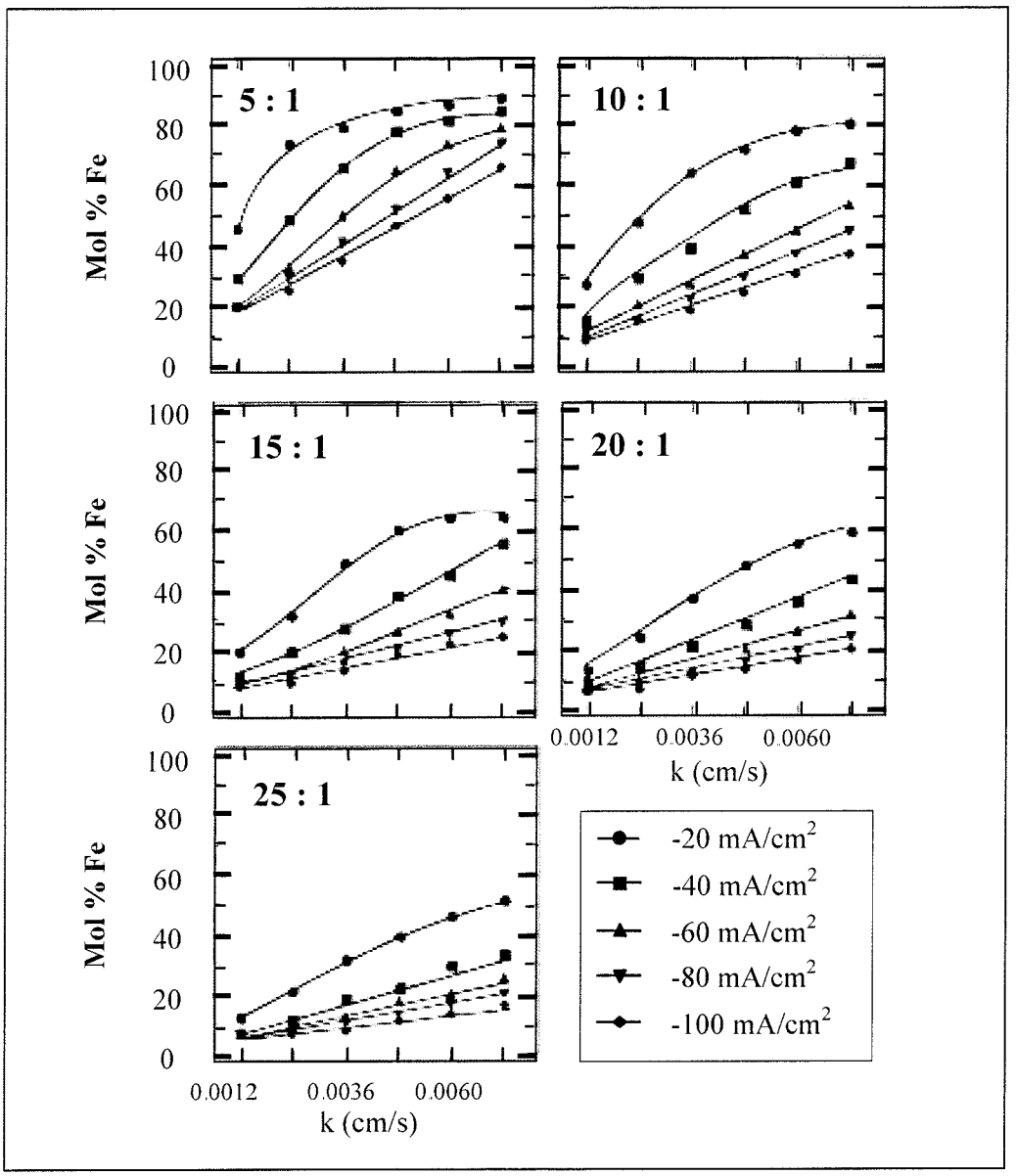

Figure 4-4: The effect of current density and electrolyte agitation on deposit composition for the family of sulfamate/chloride electrolytes. The dissolved Ni^{+2}:Fe^{+2} molar concentration ratio in the five baths varies from 5:1 to 25:1 as indicated; Leith [2].

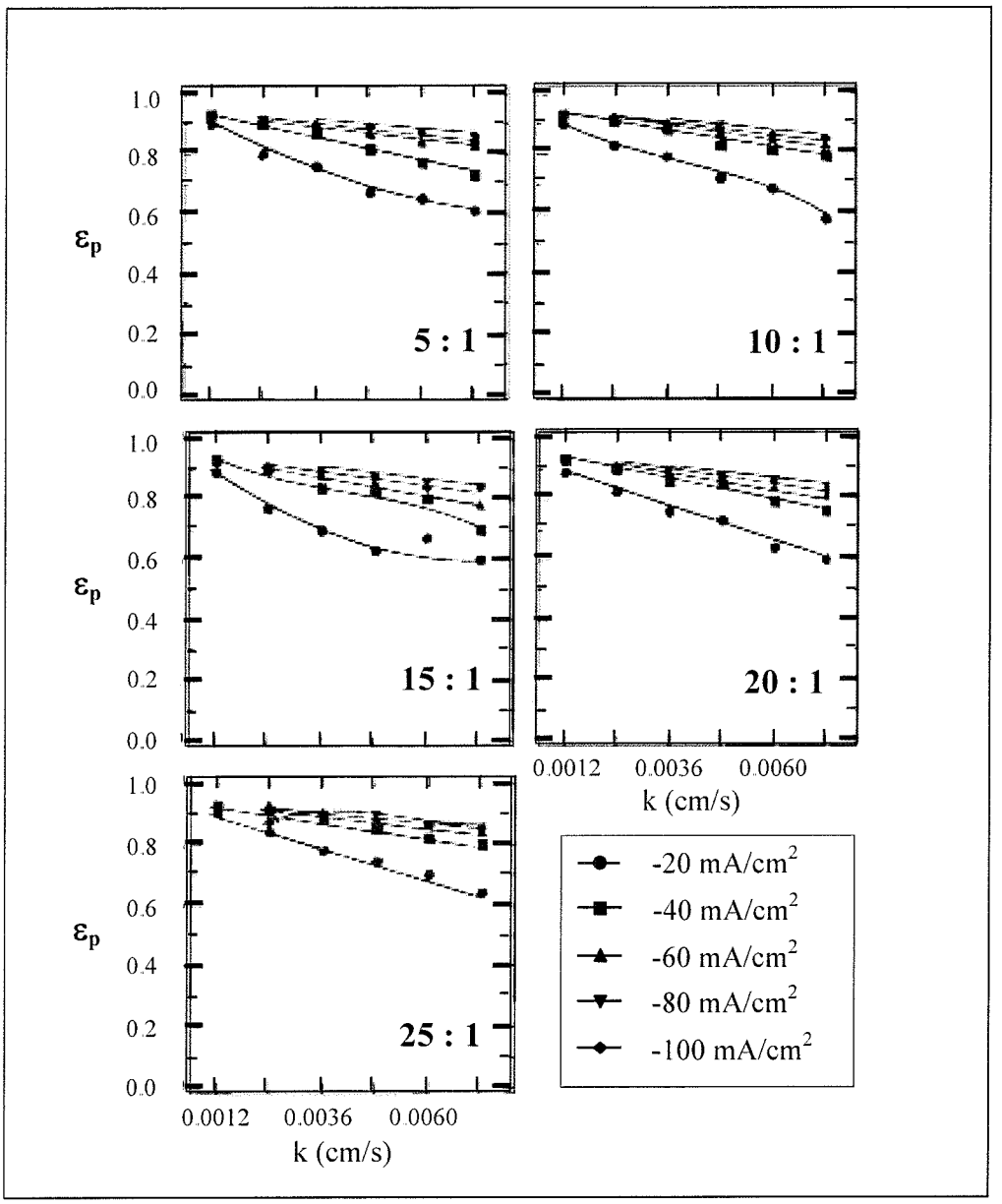

Figure 4-5: The effect of current density and electrolyte agitation on plating efficiency for the family of sulfamate/chloride electrolytes. The dissolved Ni^{+2}:Fe^{+2} molar concentration ratio in the five baths varies from 5:1 to 25:1 as indicated; Leith [3].

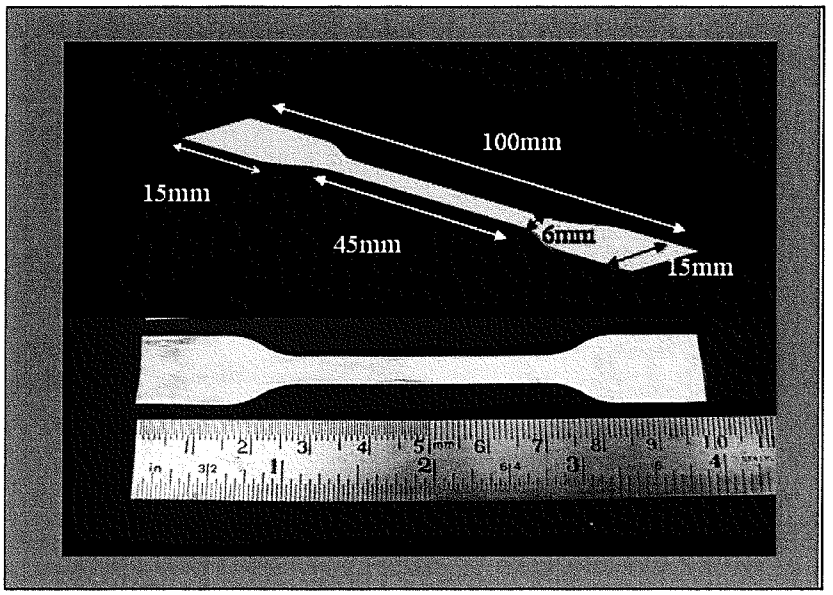

Figure 4-6: Large $Ni_{80}Fe_{20}$ dog-bone test specimen.

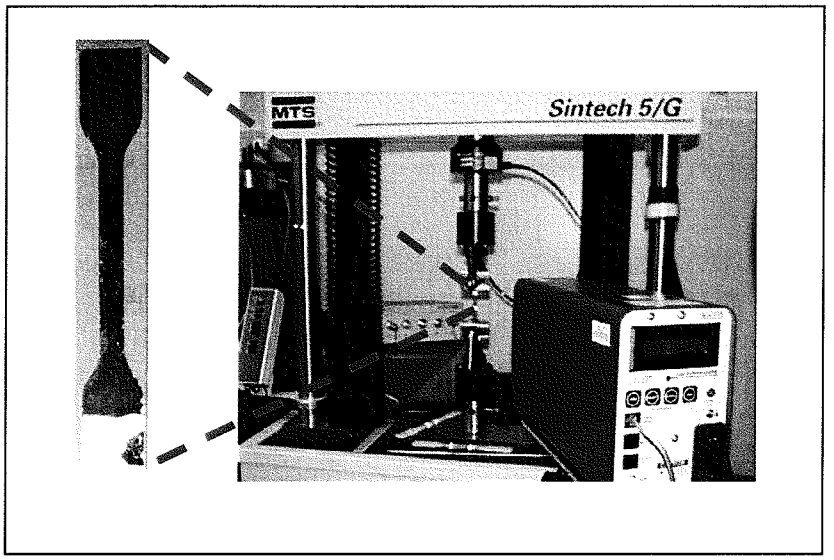

Figure 4-7: MTS Full Load tensile Testing System with large dog-bone test specimen.

Table 4-2: Young's Modulus (E) and Ultimate Stress (σ_{ult}) values for preliminary test specimen. The boundary conditions were: Agitation =300 rpm; Temperature = 25 °C; and current density = 10 mA/cm^2.

Young's Modulus (E)					
A (GPa)	**B (GPa)**	**C (GPa)**	**D (GPa)**	**Mean (GPa)**	**Standard Deviation**
		100.46	109.01	**104.73**	**6.04**
	104.85	111.49	119.32	**111.89**	**7.25**
119.04	94.18	142.62	121.70	**119.39**	**19.84**
Ultimate Stress (σ_{ult})					
A (MPa)	**B (MPa)**	**C (MPa)**	**D (MPa)**	**Mean (MPa)**	**Standard Deviation (MPa)**
		1,541.97	1,743.48	**1,642.73**	**142.50**
	1,325.31	1,723.96	1,768.97	**1,606.08**	**244.19**
1,839.68	1,795.08	1,865.12	1,980.35	**1,870.06**	**79.02**

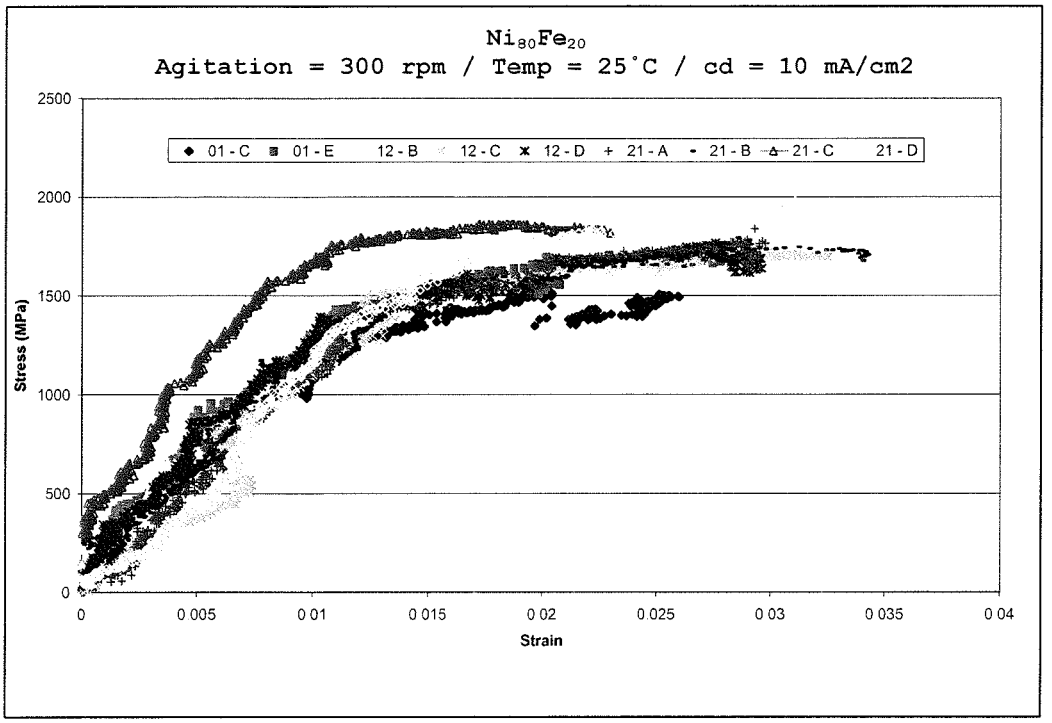

Figure 4-8: Stress-Strain Curves for $Ni_{80}Fe_{20}$ preliminary using the MTS testing system and large dog-bone test specimens.

Typically; large, relative to the $Ni_{80}Fe_{20}$ dog-bone test specimens (see Figure 4-6), are tested on the MTS testing system. There were some challenges in testing $Ni_{80}Fe_{20}$ dog-bone test specimens. Given the size—45 mm gauge-length, 6 mm in width, and ranges from 20 to 80 μm in thickness—meticulous care had to be taken to ensure proper test specimen's alignment was achieved; this care was to ensure that no twisting occurred causing a torsion load to be applied in the testing. In additional, slipping at the specimen's grip area was observed when the applied load achieved 50 lb, notwithstanding raising grip pressure (100 psi) to the limit.

As a result, a Micro-Nano Test Frame (MNTF), shown in Figures 4-9 and 4-10, was developed to enable a tensile load to be applied to a micro-scale specimen, and allow for the monotonic strain measurement within the gage area of the specimen. The micro-nano characterization system provides better load cell resolution (0.001 N at full scale) than the conventional MTS test system. The system allows for ultra-fine load stepping (1/1028 revolution), and provides more accurate gripping of the thin micro-structures with no sample twisting. An additive advantage of the micro-nano characterization system is for the incorporation of micro/nano scale strain measurement with an AFM (Atomic Force Microscope), Huang [4].

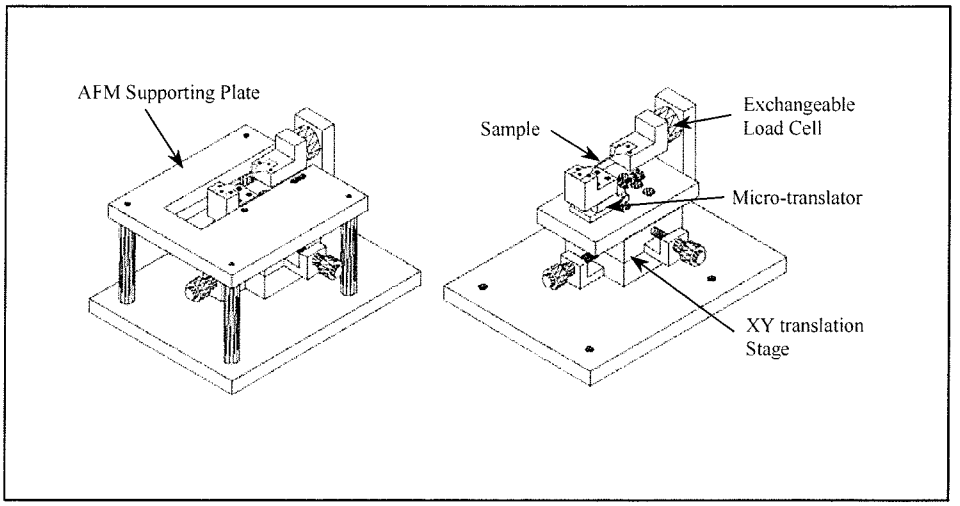

Figure 4-9: Advanced Micro-Nano Scale Test System (atomic force microscope not shown).

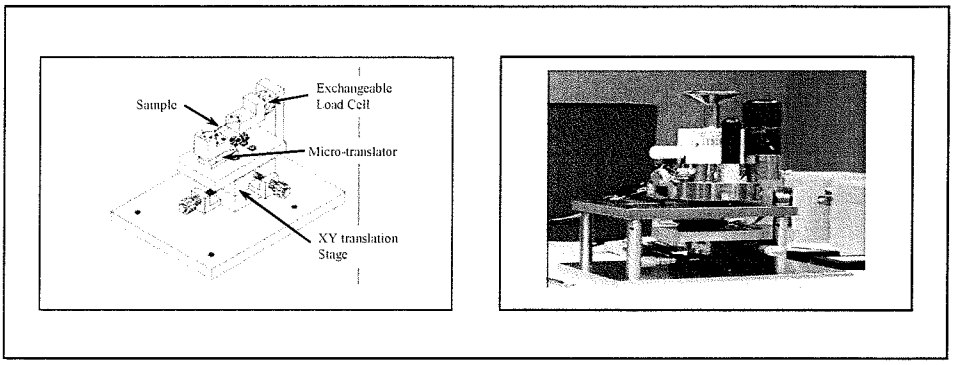

Figure 4-10: (Left) Schematic of CAU's Micro/Nano Scale Testing System; (right) Micro/Nano Scale Testing System, developed CAU, along with an Atomic Force Microscope (AFM).

Along with the new advanced micro-nano scale test system, a smaller new design dog-bone test specimen was fabricated. The new dog-bone test specimen has been reduced in size shown in Figure 4-11.

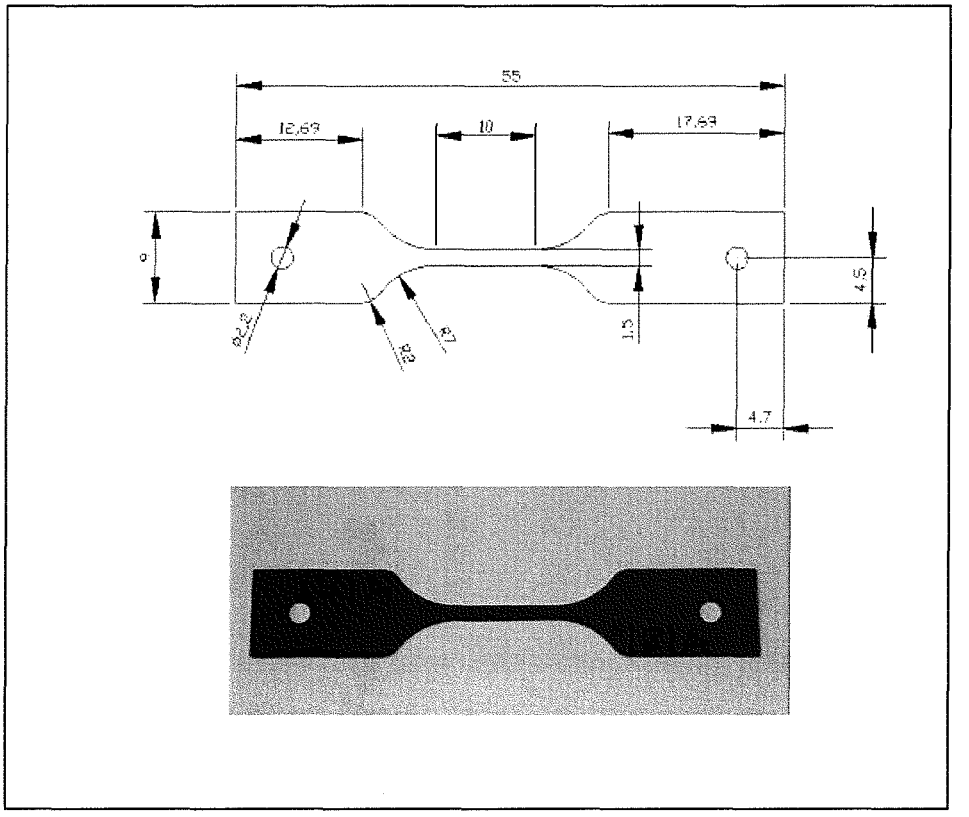

Figure 4-11: (Top) Schematic of new design dog-bone test specimen (all measurements are in mm); (bottom) actual smaller dog-bone test specimen.

The micro-nano scale test system was calibrated using a clip on an extensometer, strain gauge, and laser extensometer, the results are shown in Figure 4-12.

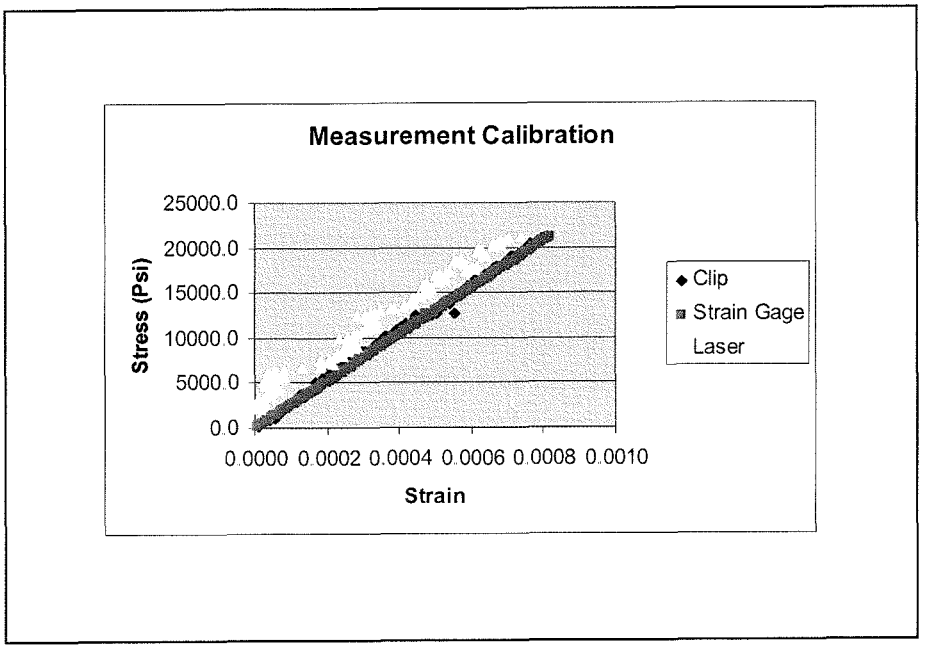

Figure 4-12: Measurement system calibration using clip on extensometer, strain gage, and laser extensometer.

After the advanced micro-nano scale test system was successfully calibrated, the specimen's design test matrix was established, shown in Table 4-3. The baseline condition was chosen to be the case where: Agitation = 300 rpm; Temperature = 25 °C; and Current Density = 10 mA/cm^2.

Figure 4-13 is a plot of ultimate strength (σ_{ult}) as vs. specimen's thickness; and Figure 4-14 is a plot of the baseline condition.

Table 4-3: $Ni_{80}Fe_{20}$ Specimens test matrix for 2^3 Factorial Analysis DOE.

	Current Density (mA/cm^2)		Agitation (RPM)		Temp (deg C)	
Batch	5	10	0	300	25	50
1						
2						
3						
4						
5						
6						
7						
8						

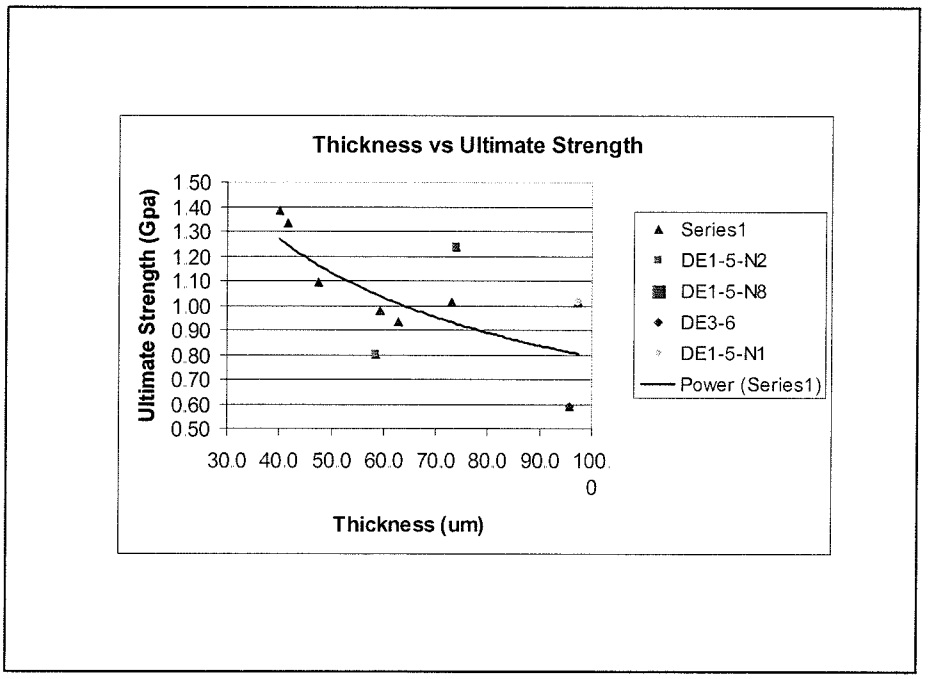

Figure 4-13: Ultimate Strength as a function of thickness.

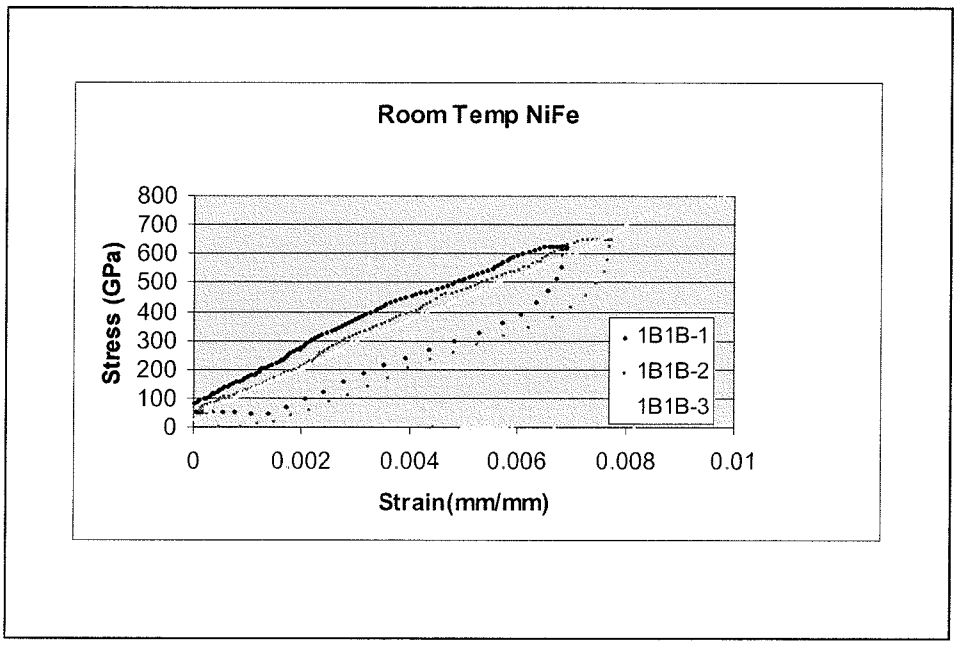

Figure 4-14: Stress strain curve of $Ni_{80}Fe_{20}$ baseline condition: Agitation = 300 rpm; Temperature = 25°C; and Current Density = 10 mA/cm^2.

4.2 Statistical Model

In this study, three independent variables, or boundary conditions, were chosen. The objective was to determine how these boundary conditions influence the mechanical properties of electro-deposited $Ni_{80}Fe_{20}$; in particular, Young Modulus and Ultimate Strength. A three-factor boundary valued, 2^3 factorial analysis Design of Experiment (DOE) was conducted; the general design for three-factor analysis of variance model is given by:

$$E_{ijk} = \mu + \tau_i + \beta_j + \gamma_k + (\tau\beta)_{ij} + (\tau\gamma)_{ik} + (\beta\gamma)_{jk} + (\tau\beta\gamma)_{ijk} + \varepsilon_{ijkl} \begin{cases} i = 1, 2, \ldots, a \\ j = 1, 2, \ldots, b \\ k = 1, 2, \ldots, c \\ l = 1, 2, \ldots, n \end{cases} \quad 4\text{-}1$$

where

μ = the overall mean for the population

τ_i = the treatment effect for level i, due to factor A (current density) and is equal to $\mu_i - \mu$

β_j = the row effect for level j, due to factor B (temperature) and is equal to $\mu_j - \mu$

γ_k = the column effect for level k, due to factor C (agitation) and is equal to $\mu_k - \mu$

$(\tau\beta)_{ij}$ = the effect of the interaction between τ_i and β_j

$(\tau\gamma)_{ik}$ = the effect of the interaction between τ_i and γ_k

$(\beta\gamma)_{jk}$ = the effect of the interaction between β_j and γ_k

$(\tau\beta\gamma)_{ijk}$ = the effect of the interaction among τ_i, β_j, and γ_k

ε_{ijkl} = the effect a random error component

The three factors: agitation (A); temperature (T); and current density (C) were fixed. The analysis of variance is shown in Table 4-4, and the *F*-tests on the main and interactions follow directly from the expected mean squares.

Table 4-4: The Analysis of Variance Table for the Three-Factor Fixed Model

Source of Variation	Sum of Squares	Degrees of Freedom	Mean Square	Expected Mean Square	F_o
A	SS_A	a – 1	MS_A	$\sigma^2 + \frac{bcn\sum \tau_i^2}{a-1}$	$F_o = \frac{MS_A}{MS_E}$
T	SS_T	b – 1	MS_T	$\sigma^2 + \frac{acn\sum \beta_j^2}{b-1}$	$F_o = \frac{MS_T}{MS_E}$
C	SS_C	c – 1	MS_C	$\sigma^2 + \frac{abn\sum \gamma_k^2}{c-1}$	$F_o = \frac{MS_C}{MS_E}$
AT	SS_{AT}	(a – 1)(b – 1)	MS_{AT}	$\sigma^2 + \frac{cn\sum\sum (\tau\beta)_{ij}^2}{(a-1)(b-1)}$	$F_o = \frac{MS_{AT}}{MS_E}$
AC	SS_{AC}	(a – 1)(c – 1)	MS_{AC}	$\sigma^2 + \frac{bn\sum\sum (\tau\gamma)_{ik}^2}{(a-1)(c-1)}$	$F_o = \frac{MS_{AC}}{MS_E}$
TC	SS_{TC}	(b – 1)(c – 1)	MS_{TC}	$\sigma^2 + \frac{n\sum\sum\sum (\tau\beta\gamma)_{ijk}^2}{(a-1)(b-1)(c-1)}$	$F_o = \frac{MS_{TC}}{MS_E}$
ATC	SS_{ATC}	(a – 1)(b – 1)(c – 1)	MS_{ATC}	σ^2	$F_o = \frac{MS_{ATC}}{MS_E}$
Error	SS_{Error}	abc(n – 1)	MS_{Error}		
Total	SS_{Total}	abcn - 1			

The three variables or boundary conditions: agitation (A); temperature (T); and current density (C) each were run at two levels. This design is called a 2^3 factorial design. The levels of the factors are arbitrarily called "low" and "high." There are eight treatment combinations in this design, and are shown geometrically as a cube, see Figures 4-15 and 4-16.

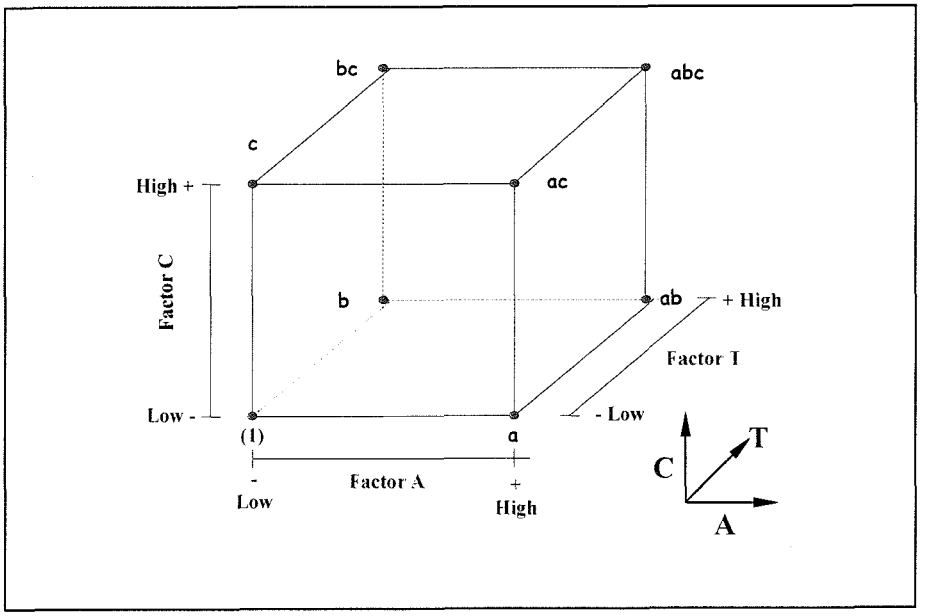

Figure 4-15: Treatment combinations in the 2^3 design.

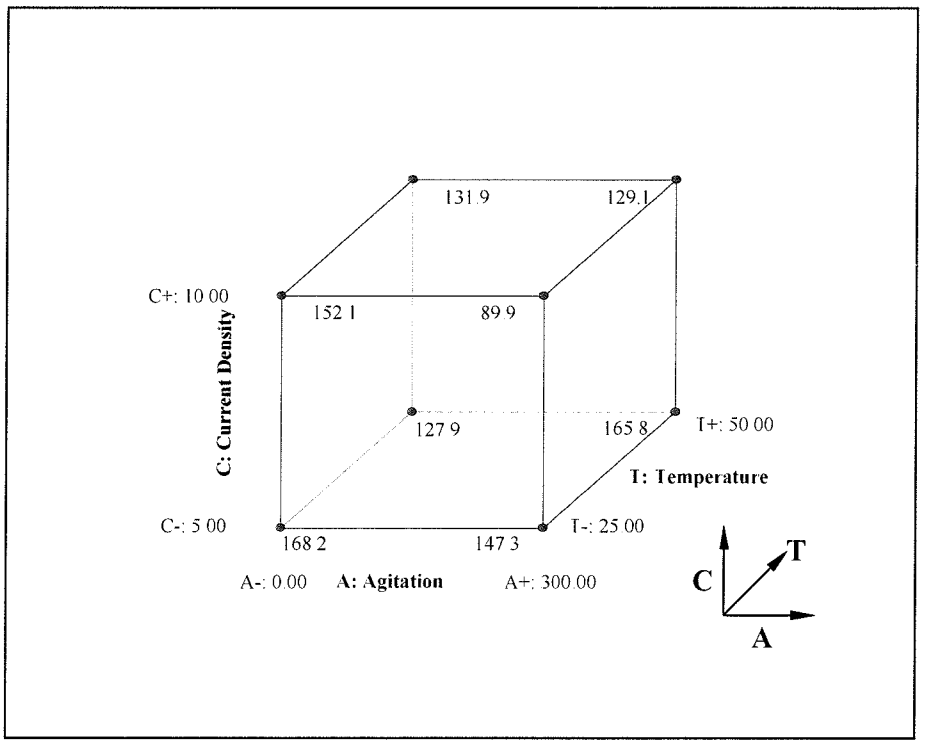

Figure 4-16: 2^3 Factorial Design Treatment Combinations Cube for Young Modulus.

Using the "+ and –" notation (also known as the geometric notation) to represent the low and high levels of the boundary conditions, the eight runs in the 2^3 factorial design are shown in Table 4-5. This is called the design matrix; where the treatment combinations are written in the following order: abc, bc, ac, c, ab, b, a, (1). These symbols also represent the total of all *n* observations taken at that particular treatment combination.

There are seven degrees of freedom between the eight treatment combinations in the 2^3 factorial design analysis. Three degrees of freedom are associated with the main effect: agitation (A), temperature (T), and current density (C). Four degrees of

freedom are associated with the interactions: agitation-temperature (AT); agitation-current density (AC); temperature-current density (TC); and agitation-temperature-current density (ATC). The treatment combinations are shown in Table 4-5b.

Table 4-5a: Measured Young Modulus (E) values and standard deviation for each test case.

Young's Modulus (E)						
Test Specimen	**A (GPa)**	**B (GPa)**	**C (GPa)**	**D (GPa)**	**Mean (GPa)**	**Standard Deviation (GPa)**
1B2		113.96	144.31		**129.1**	**21.5**
1B4	104.52	123.33	158.03	141.63	**131.9**	**23.1**
1B1	91.7	84.6	94.6	88.7	**89.9**	**4.3**
9B1	189.66		114.62		**152.1**	**53.1**
2B6		155.55	176.02		**165.8**	**14.5**
2B8	145.89	123.97	113.78		**127.9**	**16.4**
10B5		160.24	134.44		**147.3**	**18.2**
10B7	175.78	203.92	151.76	141.16	**168.2**	**27.9**

Table 4-5b: Algebraic Sign for Calculating Effects in the 2^3 Design, with measured Young Modulus (E) values.

Treatment Combination	Factorial Effect								
	I	**A**	**T**	**AT**	**C**	**AC**	**TC**	**ATC**	**E**
abc	+	+	+	+	+	+	+	+	**129.135**
bc	+	-	+	-	+	-	+	-	**131.880**
ac	+	+	-	-	+	+	-	-	**89.900**
c	+	-	-	+	+	-	-	+	**152.140**
ab	+	+	+	+	-	-	-	-	**165.785**
b	+	-	+	-	-	+	-	+	**127.880**
a	+	+	-	-	-	-	+	+	**147.340**
(1)	+	-	-	+	-	+	+	-	**168.200**

Next, consider estimating the boundary conditions' main effect. The effect of agitation (A) when temperature (T) and current density (C) are at the low level is given by:

$$[a-(1)]/n \qquad 4\text{-}2$$

Similarly, the effect of agitation when temperature (T) is at high level and current density (C) is at low level is given by:

$$[ab - b]/n \qquad 4\text{-}3$$

Continuing, the effect of agitation (A) when current density (C) is at high level and temperature (T) is at low level is given by:

$$[ac - c]/n \qquad 4\text{-}4$$

Finally, the effect of agitation (A) when both temperature (T) and current density (C) are at high level is given by:

$$[abc - bc]/n \qquad 4\text{-}5$$

Thus, the average effect of agitation (A) is given by:

$$Effect\ of\ Agitation\ or\ A = \overline{E}_{A^+} - \overline{E}_{A^-} \qquad 4\text{-}6$$

or it can be computed as the average of equations 4-2, 4-3, 4-4, and 4-5, i.e.

$$Effect\ of\ Agitation\ or\ A = \frac{1}{4n}[a - (1) + ab - b + ac - c + abc - bc] \qquad 4\text{-}7$$

This equation can also be developed as a contrast between four treatment combinations in the right face of the cube (where A is at high level), and the four in the left face (where A is at low level) shown in Figure 4-17. That is, the A effect is just the average of the four runs where A is at the high level ($\overline{E}_{A^+}$) minus the average of four runs where A is at the low level ($\overline{E}_{A^-}$) or

$$A = \frac{a + ab + ac + abc}{4n} - \frac{(1) + b + c + bc}{4n} \qquad 4\text{-}8$$

Rearrange equation 4-8, yields

$$A = \frac{1}{4n}[a + ab + ac + abc - (1) - b - c - bc] \qquad 4\text{-}9$$

Hence, using the values corresponding to the treatment conditions shown in Table 4-5 yield the following value:

$$A = \frac{1}{4}[147.340 + 165.785 + 89.900 + 129.135$$

$$- 168.200 - 127.880 - 152.140 - 131.880]$$

$$A = \frac{1}{4}[-47.940] = -11.985$$

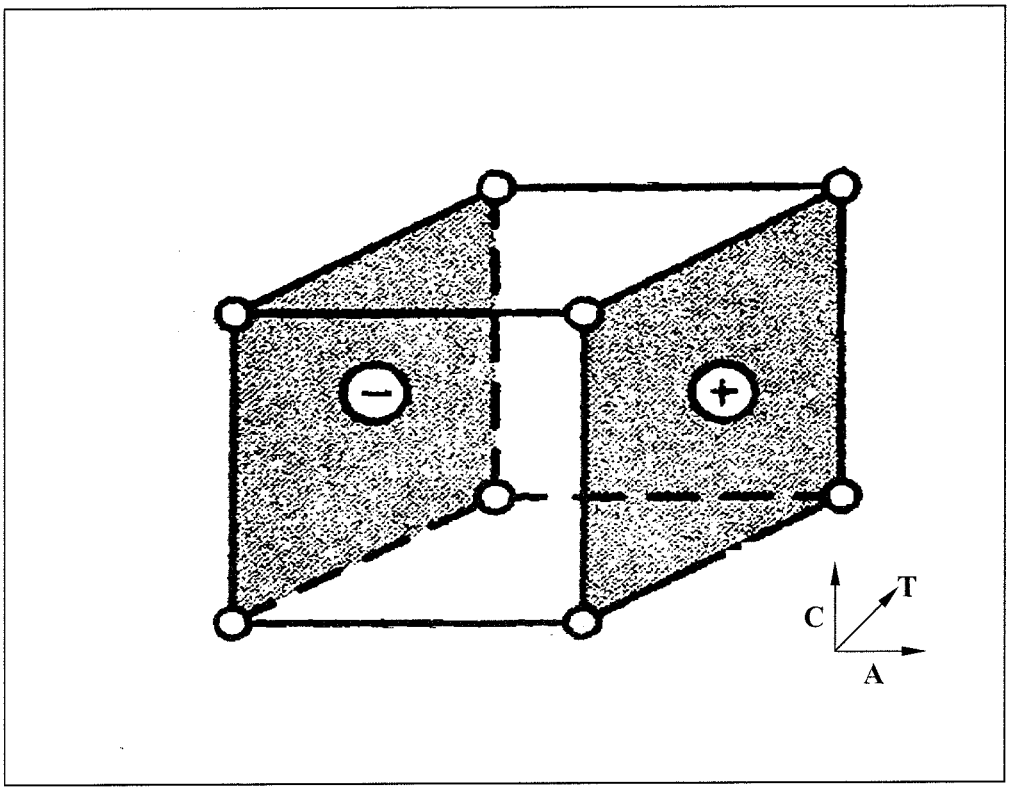

Figure 4-17: Young Modulus' Main Effect of Agitation (A).

In a similar manner, the effect of temperature (T) is the difference in averages between the four treatment combinations in the front face of the cube and the four in the back, shown in Figure 4-18.

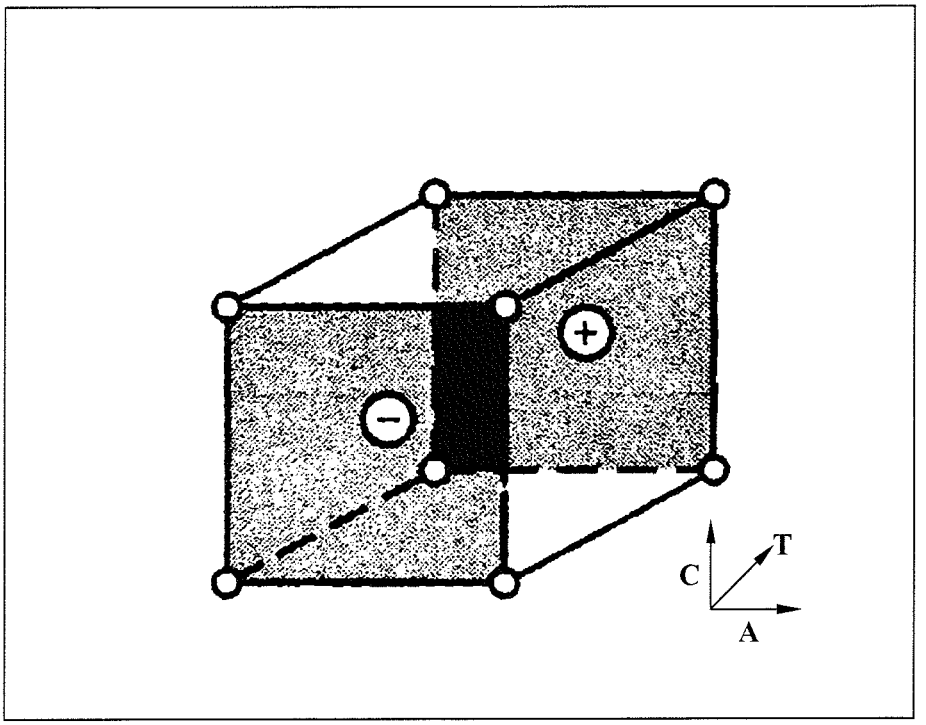

Figure 4-18: Young Modulus' Main Effect of Temperature (T).

This result is

$$Effect\ of\ Temperature\ or\ T = \overline{E}_{Temp^+} - \overline{E}_{Temp^-} \qquad 4\text{-}10$$

which yields

$$T = \frac{1}{4n}[b + ab + bc + abc - (1) - a - c - ac] \qquad 4\text{-}11$$

Again, using the values corresponding to the treatment conditions shown in Table 4-5 yield the following value:

$$T = \frac{1}{4}[127.880 + 165.785 + 131.880 + 129.135 - 168.200$$

$$- \ 147.340 - 152.140 - 89.900]$$

$$T = \frac{1}{4}[-2.900] = -0.725$$

The effect of current density (C) is the difference in the averages between the four treatment combinations in the top face of the cube and the four in the bottom, as shown in Figure 4-19.

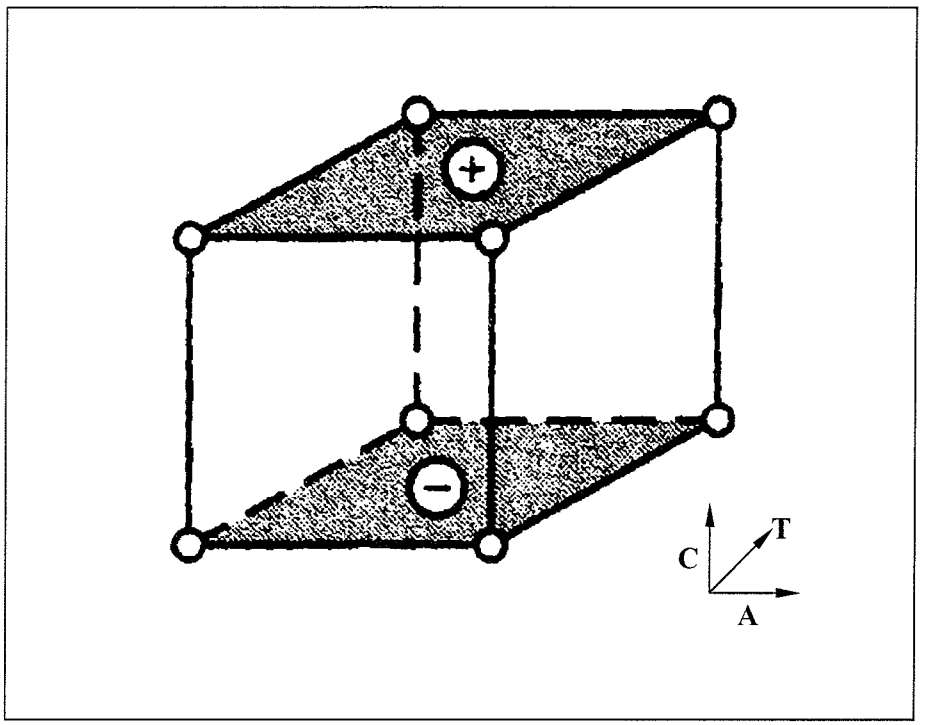

Figure 4-19: Young Modulus' Main Effect of Current Density (C).

That is

$$Effect\ of\ Current\ Density\ or\ C = \overline{E}_{Current\ Density^{+}} - \overline{E}_{Current\ Density^{-}} \qquad 4\text{-}12$$

$$C = \frac{1}{4n}[c + ac + bc + abc - (1) - a - b - ab] \qquad 4\text{-}13$$

Using the values corresponding to the treatment conditions shown in Table 4-5 yield the following value:

$$C = \frac{1}{4}[152.140 + 89.900 + 131.880 + 129.135 - 168.200$$

$$-147.340 - 127.880 - 165.785]$$

$$C = \frac{1}{4}[-106.150] = -26.5375$$

The two-factor interaction effects may be computed easily, for example the measure of the agitation-temperature (AT) interaction is the difference between the average agitation effects at the two-levels of temperature (T). By convention, one-half of this difference is called the agitation-temperature, symbolically shown in Table 4-6. Because the agitation-temperature is one-half of this difference, the effect of agitation-temperature is given by:

$$AT = \frac{[abc - bc + ab - b - ac + c - a + (1)]}{4n} \qquad 4\text{-}14$$

Table 4-6: Agitation-Temperature (AT) Interaction Calculation.

Temperature (T)	Average Agitation (A) Effect
High (+)	$\frac{[(abc - bc) + (ab - b)]}{2n}$
Low (-)	$\frac{[(ac - c) + (a - (1))]}{2n}$
Difference	$\frac{[abc - bc + ab - b - ac + c - a + (1)]}{2n}$

Substituting the values shown in Table 4-6 for the corresponding to the treatment conditions yield:

$$AT = \frac{1}{4}[129.135 + 165.785 + 152.140 + 168.200 - 131.880$$

$$-127.880 - 89.900 - 147.340]$$

$$AT = \frac{1}{4}[118.260] = 29.565$$

Rewriting AT in equation 4-14, yields

$$AT = \frac{abc + ab + c + (1)}{4n} - \frac{bc + b + ac + a}{4n} \qquad 4\text{-}15$$

And in this form, the AT interaction is easily seen to be the difference in averages between runs on two diagonal planes in the cube shown in Figure 4-20.

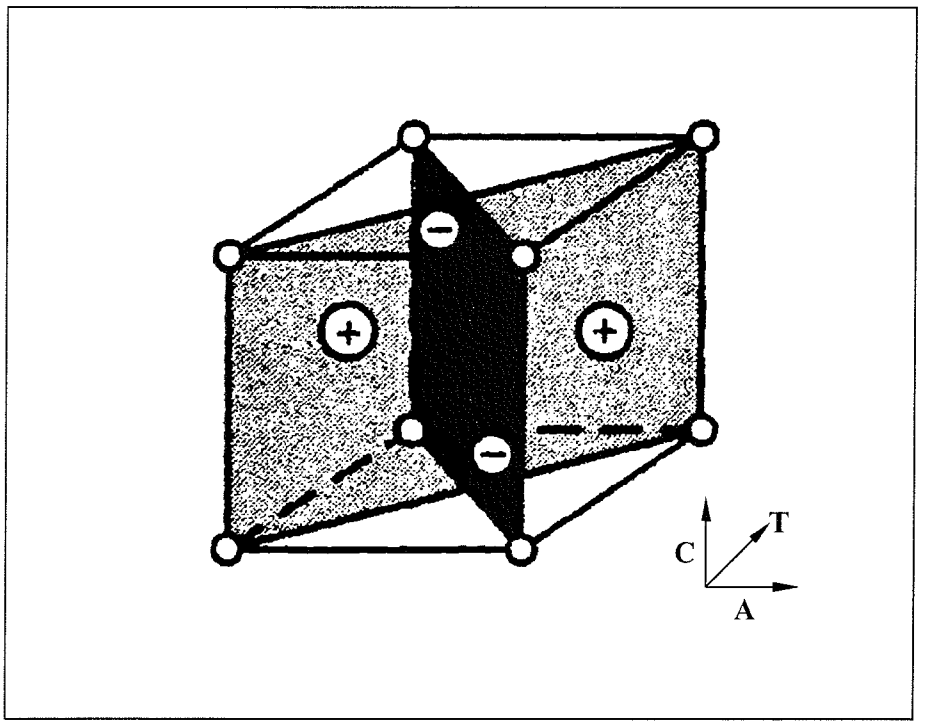

Figure 4-20: Young Modulus' Agitation-Temperature (AT) interaction.

Using similar logic, and referring to Figures 4-21 and 4-22; the agitation-current density and temperature-current density interactions are:

$$AC = \frac{1}{4n}[(1) - a + b - ab - c + ac - bc + abc] \qquad 4\text{-}16$$

$$TC = \frac{1}{4n}[(1) + a - b - ab - c - ac + bc + abc] \qquad 4\text{-}17$$

Using the values corresponding to the treatment conditions, shown in Table 4-5, yield the following values:

$$AC = \frac{1}{4}[168.200 - 147.34 + 127.880 - 165.785 - 152.140 + 89.900 - 131.880 + 129.135]$$

$$AC = \frac{1}{4}[-82.030] = -20.5075$$

$$TC = \frac{1}{4}[168.200 + 147.340 - 127.880 - 165.785 - 152.140 - 89.900 + 131.880 + 129.135]$$

$$TC = \frac{1}{4}[40.850] = 10.2125$$

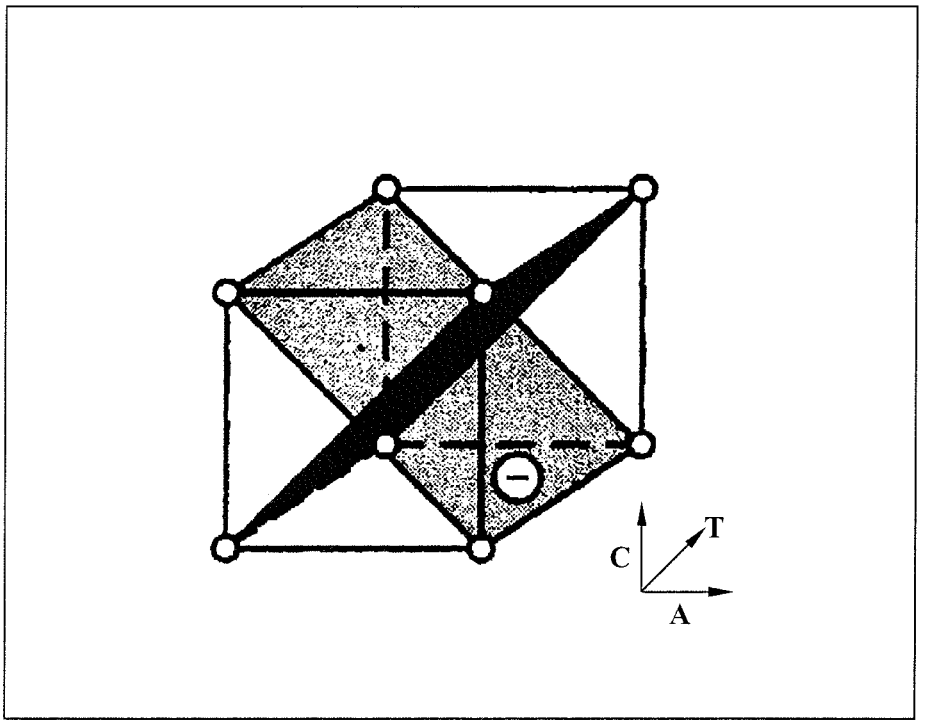

Figure 4-21: Young Modulus' Agitation-Current Density (AC) interaction.

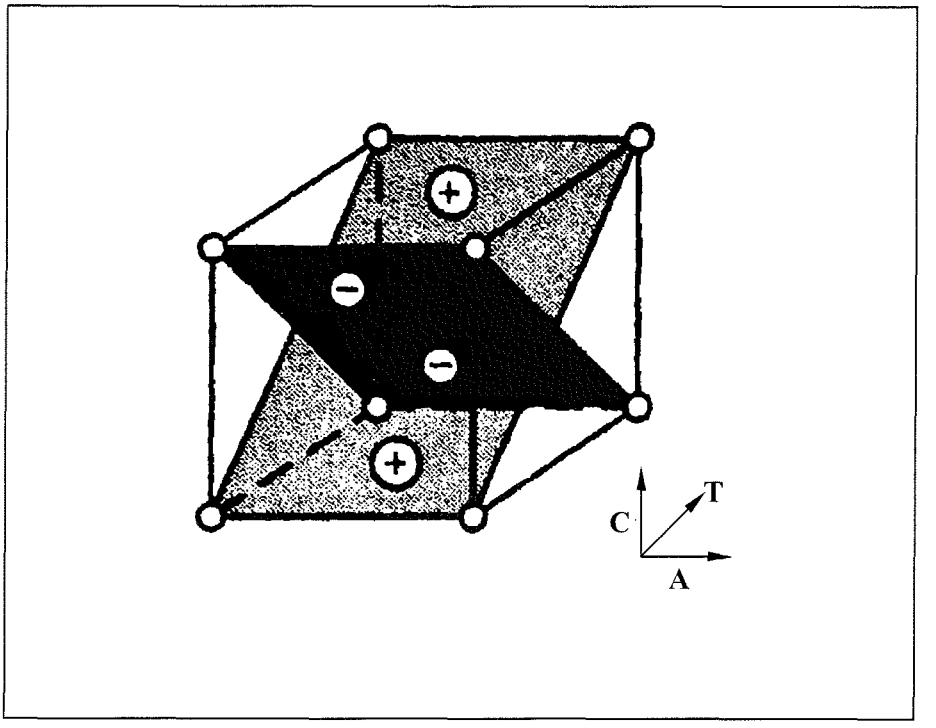

Figure 4-22: Young Modulus' Temperature-Current Density (TC) interaction.

Finally, agitation-temperature-current density (ATC) interaction is defined as the average difference between the agitation-temperature interactions for the two different levels of current density, see Figure 4-23. Thus agitation-temperature-current density effect is given by:

$$ATC = \frac{1}{4n}[abc - bc - ac + c - ab + b + a - (1)] \qquad 4\text{-}18$$

Substituting the values from Table 4-5 yield:

$$ATC = \frac{1}{4}[129.135 - 131.880 - 89.900 + 152.140 - 165.785$$

$$+ 127.880 + 147.340 - 168.200]$$

$$ATC = \frac{1}{4}[0.730] = 0.1825$$

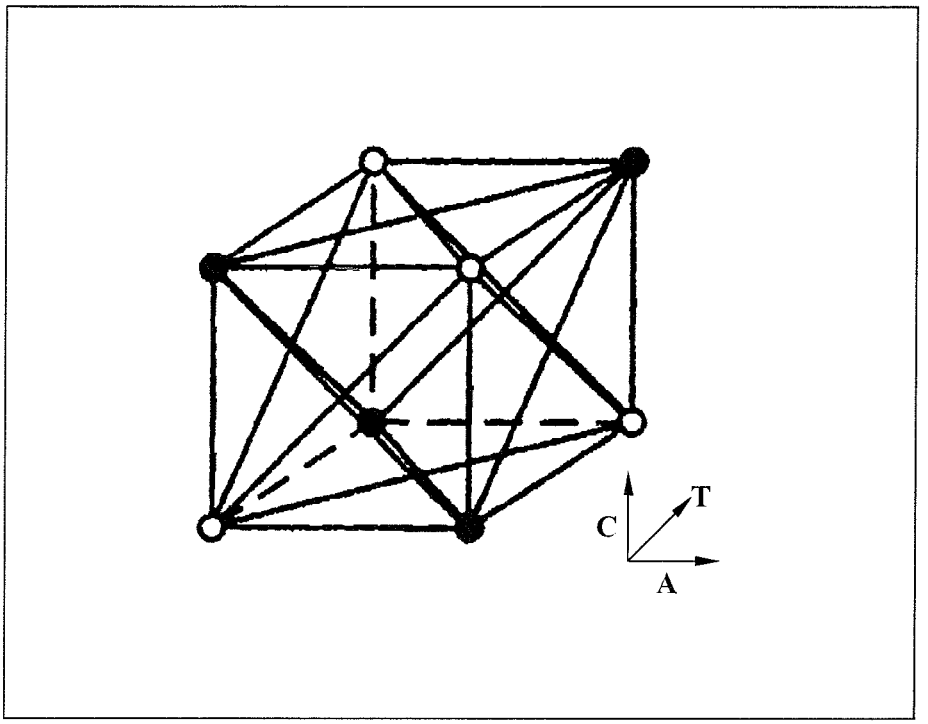

Figure 4-23: Young Modulus' Agitation-Temperature-Current Density (ATC) interaction.

In equations: 4-9, 4-11, 4-13, 4-14, 4-16, 4-17, and 4-18, the quantities in the brackets are *contrasts* in the treatment combinations. A table of plus and minus signs have been developed from the contrasts; the signs for the main effects have been established and the signs for the remaining columns have been obtained by multiplying the appropriate preceding columns, row by row—this is shown in Table 4-5.

Table 4-5 has several interesting properties: (1) except for column *I*, every column has an equal number of plus and minus signs; (2) the sum of the products of the signs in any two columns is zero; (3) column *I* multiplied times any column leaves that column

unchanged, i.e. *I* is an identity element; and (4) the product of any two columns yields a column in the table. For example

$$A \times T = AT, \text{ and}$$

$$AT \times T = AT^2 = A$$

Hence, the exponents in the products are formed by using *modulus-2* arithmetic. (That is, the exponent can only be 0 or 1; if it is greater than 1, it is reduced by multiples of 2 until it is either 0 or 1.) All of these properties are implied by the orthogonality of the contrasts used to estimate the effects.

As a result, the Sums of squares for the effects are easily computed, because each effect has a corresponding single-degree-of-freedom contrast. In the 2^3 design with n replicates, the sum of squares for any effect is

$$SS = \frac{(contrast)^2}{8n} \qquad 4\text{-}19$$

Hence, from 4-9, 4-11, 4-13, 4-14, 4-16, 4-17 and 4-18 the main effect for:

- agitation (A) = -11.985
- temperature (T) = -0.725
- current density (C) = -26.5375
- agitation-temperature AT = 29.565
- agitation-current density (AC) = -20.5075
- temperature-current density (TC) = 10.2125
- agitation-temperature-current density (ATC) = 0.1825

Therefore, the Sums of squares are calculated using equation 4-19 as follows:

$$SS_{Agitation} = SS_A = \frac{(-47.940)^2}{8} = 287.280$$

$$SS_{Temperature} = SS_T = \frac{(-2.900)^2}{8} = 1.051$$

$$SS_{Current\ Density} = SS_C = \frac{(-106.150)^2}{8} = 1408.478$$

$$SS_{Agitation-Temperature} = SS_{AT} = \frac{(118.260)^2}{8} = 1748.178$$

$$SS_{Agitation-Current\ Density} = SS_{AC} = \frac{(-82.030)^2}{8} = 841.115$$

$$SS_{Temperature-Current\ Density} = SS_{TC} = \frac{(40.850)^2}{8} = 208.590$$

$$SS_{Agitation-Temperature-Current\ Density} = SS_{ATC} = \frac{(0.730)^2}{8} = 0.067$$

Table 4-7: Effect Estimate Summary for Young Modulus E; "*" values were calculated using the Design-Expert Software.

Factor	Effect of Estimate	Sum of Squares	Percent Contribution
Model*		2036.51	
A	-11.985	287.280	6.39
T	-0.725	1.051	0.02
C	-26.5375	1408.478	31.34
AT	29.565	1748.178	38.89
AC	-20.5075	841.115	18.71
TC	10.2125	208.590	4.64
ATC	0.1825	0.067	0.001
Residual*		2458.25	
Total		4494.759	

Using the classical method, the total sum of squares is given by:

$$SS_{Total} = \sum_{i=1}^{a}\sum_{j=1}^{b}\sum_{k=1}^{c}\sum_{l=1}^{n} E_{ijkl}^2 - \frac{E_{....}^2}{abcn} \qquad 4\text{-}20$$

Table 4-8: Measured for Young Modulus' (E) values at the boundary conditions.

Agitation (rpm)	Current Density (mA/cm^2)				$E_{I\ldots}$ (GPa)
	5		10		
	Temperature (Deg C)		Temperature (Deg C)		
	25	50	25	50	
0	168.200	127.880	152.140	131.880	580.100
300	147.340	165.785	89.900	129.135	532.160
E_{ijk}	315.54	293.665	242.040	261.015	1112.26 = E

Using the experimental data for the given boundary conditions, shown in Table 4-8, yield:

$$SS_{Total} = (168.2)^2 + (147.34)^2 + (127.88)^2 + (165.785)^2 + (152.14)^2 + (89.90)^2 + (131.88)^2 + (129.135)^2 - \frac{1112.26^2}{8} = 4494.76$$

Also, the classical equations for sum of squares for the main effects are given by:

$$SS_A = \frac{1}{bcn}\sum_{i=1}^{a} E_{i\ldots}^2 - \frac{E_{\ldots\ldots}^2}{abcn} \qquad 4\text{-}21$$

$$SS_T = \frac{1}{acn}\sum_{j=1}^{b} E_{j\ldots}^2 - \frac{E_{\ldots\ldots}^2}{abcn} \qquad 4\text{-}22$$

$$SS_C = \frac{1}{abn}\sum_{k=1}^{c} E_{\ldots k}^2 - \frac{E_{\ldots\ldots}^2}{abcn} \qquad 4\text{-}23$$

And in order to compute the two-factor interaction sums of squares, the total for the A x T, A x C, and T x C cells are needed. It is frequently helpful to collapse the

original data table into three two-way tables to compute these quantities. The sums of squares are found from

$$SS_{AT} = \frac{1}{cn}\sum_{i=1}^{a}\sum_{j=1}^{b} E_{ij}^2 - \frac{E^2}{abcn} - SS_A - SS_T = SS_{subtotal(AT)} - SS_A - SS_T \qquad 4\text{-}24$$

$$SS_{AC} = \frac{1}{bn}\sum_{i=1}^{a}\sum_{k=1}^{c} E_{ik}^2 - \frac{E^2}{abcn} - SS_A - SS_C = SS_{subtotal(AC)} - SS_A - SS_C \qquad 4\text{-}25$$

and

$$SS_{TC} = \frac{1}{an}\sum_{j=1}^{b}\sum_{k=1}^{c} E_{jk}^2 - \frac{E^2}{abcn} - SS_T - SS_C = SS_{subtotal(TC)} - SS_T - SS_C \qquad 4\text{-}26$$

Note that the sums of squares for the two-factor subtotals are found from the totals in each two-way table. The three-factor sum of squares is computed from the three-way cell totals $\{E_{ijk}\}$ as:

$$SS_{ATC} = \frac{1}{n}\sum_{i=1}^{a}\sum_{j=1}^{b}\sum_{k=1}^{c} E_{ijk}^2 - \frac{E^2}{abcn} - SS_A - SS_T - SS_C - SS_{AT} - SS_{AC} - SS_{TC} \qquad 4\text{-}27a$$

$$= SS_{subtotal(ATC)} - SS_A - SS_T - SS_C - SS_{AT} - SS_{AC} - SS_{TC} \qquad 4\text{-}27b$$

This implies that:

$$SS_{subtotal(ATC)} = SS_{ATC} + SS_A + SS_T + SS_C + SS_{AT} + SS_{AC} + SS_{TC} \qquad 4\text{-}28$$

Substituting the values from Table 4-7, yields

$$SS_{subtotal(ATC)} = 0.067 + 287.280 + 1.051 + 1748.178$$

$$+ 841.115 + 208.590 = 4494.759$$

4.3 The Regression Model and Response Surface for Young Modulus

The regression model for predicting the boundary conditions' influences on Young Modulus can be expressed as:

$$E = \beta_0 + \beta_1 x_1 + \beta_2 x_2 + \beta_3 x_3 + \beta_{12} x_1 x_2 + \beta_{13} x_1 x_3 + \beta_{23} x_2 x_3 + \beta_{123} x_1 x_2 x_3 \quad 4\text{-}29$$

where the coded variables x_1, x_2, and x_3 are defined on a scale from -1 to +1; the low and high levels of A, T, and C respectively. The terms x_1x_2, x_1x_3, x_2x_3, and $x_1x_2x_3$ are AT, AC, TC, and ATC interactions respectively. And the β's are regression coefficients and are related to the effect estimates.

$$\beta_1 = \frac{1}{2}(Effect\ of\ Estimate\ A) \quad 4\text{-}30$$

$$\beta_1 = \frac{-11.985}{2} = -5.993$$

$$\beta_2 = \frac{1}{2}(Effect\ of\ Estimate\ T) \quad 4\text{-}31$$

$$\beta_2 = \frac{-0.725}{2} = -0.363$$

$$\beta_3 = \frac{1}{2}(Effect\ of\ Estimate\ C) \quad 4\text{-}32$$

$$\beta_3 = \frac{-26.5375}{2} = -13.269$$

$$\beta_{12} = \frac{1}{2}(Effect\ of\ Estimate\ AT) \quad 4\text{-}33$$

$$\beta_{12} = \frac{29.565}{2} = 14.783$$

$$\beta_{13} = \frac{1}{2}(Effect\ of\ Estimate\ AC) \quad 4\text{-}34$$

$$\beta_{13} = \frac{-20.5075}{2} = -10.254$$

$$\beta_{23} = \frac{1}{2}(Effect\ of\ Estimate\ TC) \qquad 4\text{-}35$$

$$\beta_{23} = \frac{10.2125}{2} = 5.106$$

$$\beta_{123} = \frac{1}{2}(Effect\ of\ Estimate\ ATC) \qquad 4\text{-}36$$

$$\beta_{123} = \frac{0.1825}{2} = 0.091$$

And β_0 is the estimated average of all eight responses, hence

$$\beta_0 = \frac{1}{8}[129.135 + 131.880 + 89.900 + 152.140 + 165.785 + 127.880 + 147.340 + 168.200]$$

$$= 139.0325$$

The relationship between the natural variables; agitation, temperature, and current density, and the coded variables is:

$$X_1 = \frac{A - (A_{Low} + A_{High})/2}{(A_{High} - A_{Low})/2} \qquad 4\text{-}37a$$

$$X_1 = \frac{A - 150}{150} \qquad 4\text{-}37b$$

$$X_2 = \frac{T - (T_{Low} + T_{High})/2}{(T_{High} - T_{Low})/2} \qquad 4\text{-}38a$$

$$X_2 = \frac{T - 37.50}{12.50} \qquad 4\text{-}38b$$

$$X_3 = \frac{C - (C_{Low} + C_{High})/2}{(C_{High} - C_{Low})/2} \qquad 4\text{-}39a$$

$$X_3 = \frac{C-5}{2.50} \qquad 4\text{-}39b$$

As a result, the regression model—coded values—is given by:

$$E = 139.0325 - 5.993x_1 - 0.363x_2 - 13.269x_3 + 14.783x_1x_2 - 10.254\,x_1x_3 + 5.106x_2x_3 + 0.091x_1x_2x_3 \qquad 4\text{-}40$$

The regression model—in actual physical values—is given by:

$$E \approx 244.714 - 0.131A - 2.415T - 7.224C + 0.015AT - 0.032AC + 0.160TC \qquad 4\text{-}41$$

4.4 Young Modulus' Plots as a Function of the Boundary Conditions

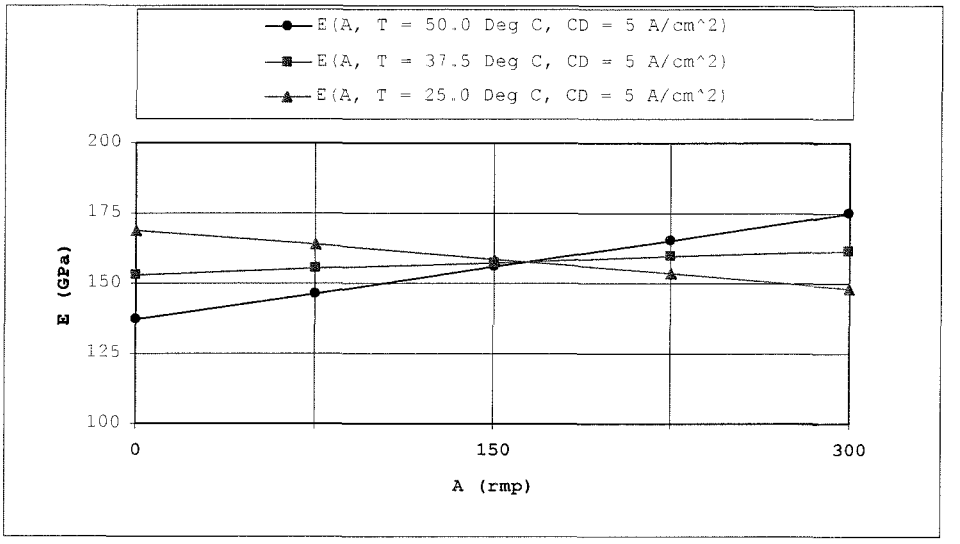

Figure 4-24: Young Modulus with varying agitation (A) and temperature (T); and constant current density (C = 5.0 A/cm^2).

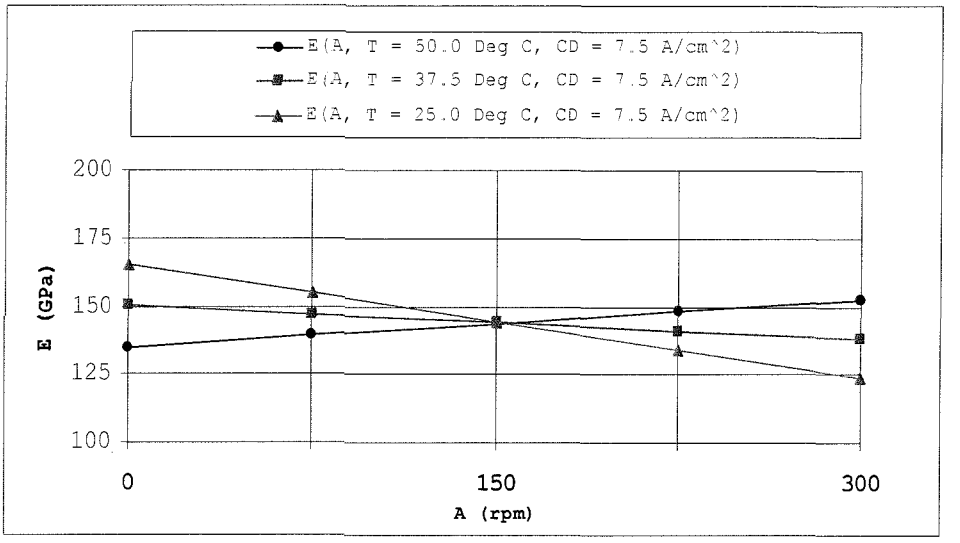

Figure 4-25: Young Modulus with varying agitation (A) and temperature (T); and constant current density (C = 7.5 A/cm^2).

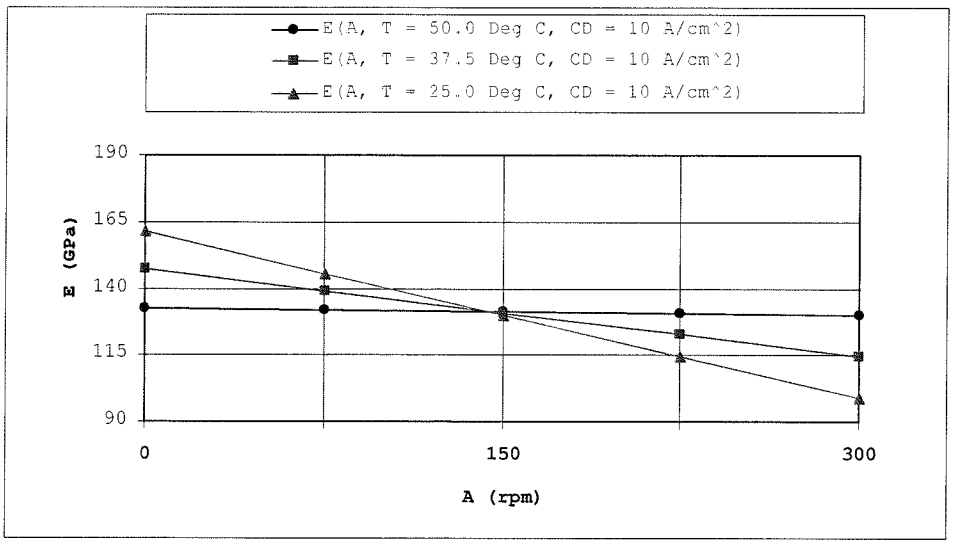

Figure 4-26: Young Modulus with varying agitation (A) and temperature (T); and constant current density (C = 10.0 A/cm^2).

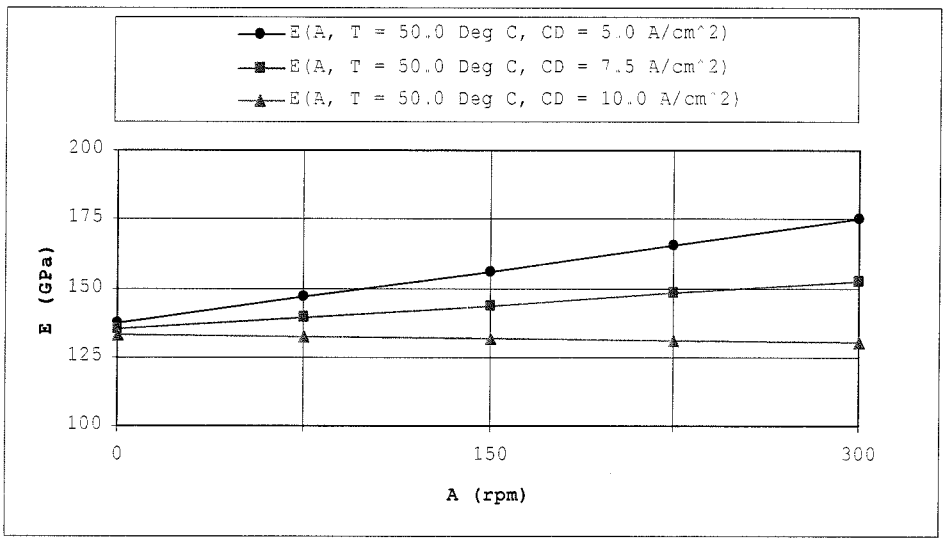

Figure 4-27: Young Modulus with varying agitation (A) and current density (C); and constant temperature (T = 50 Deg C).

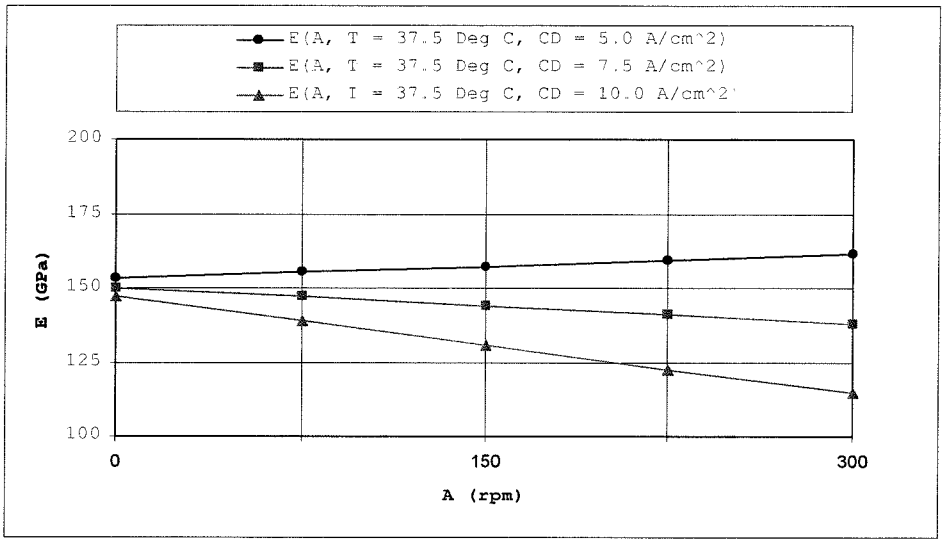

Figure 4-28: Young Modulus with varying agitation (A) and current density (C); and constant temperature (T = 37.5 Deg C).

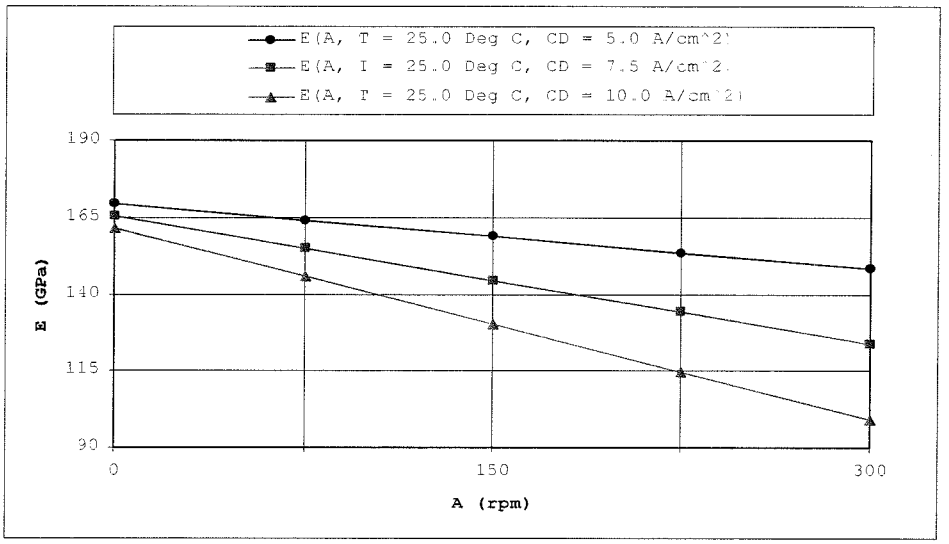

Figure 4-29: Young Modulus with varying agitation (A) and current density (C); and constant temperature (T = 25 Deg C).

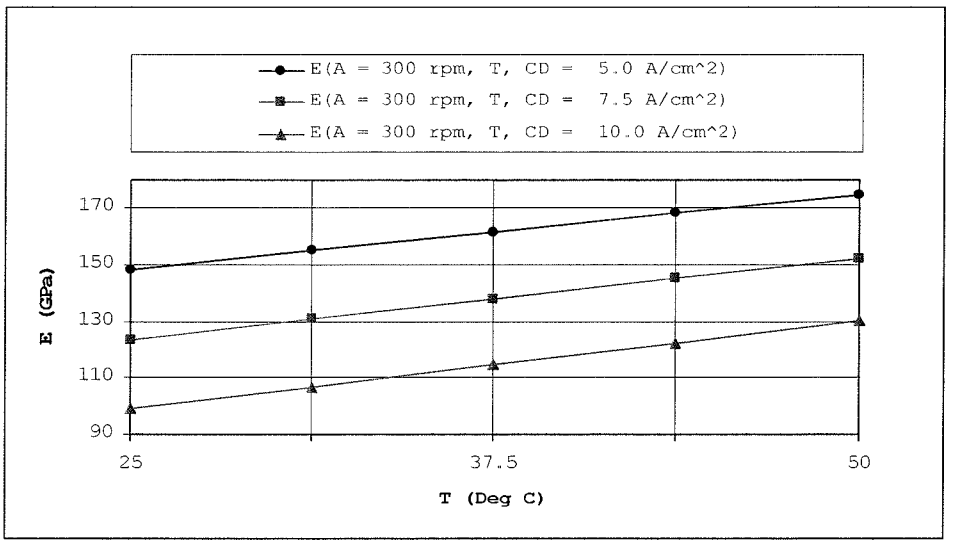

Figure 4-30: Young Modulus with varying temperature (T) and current density (C); and constant agitation (A = 300 rpm).

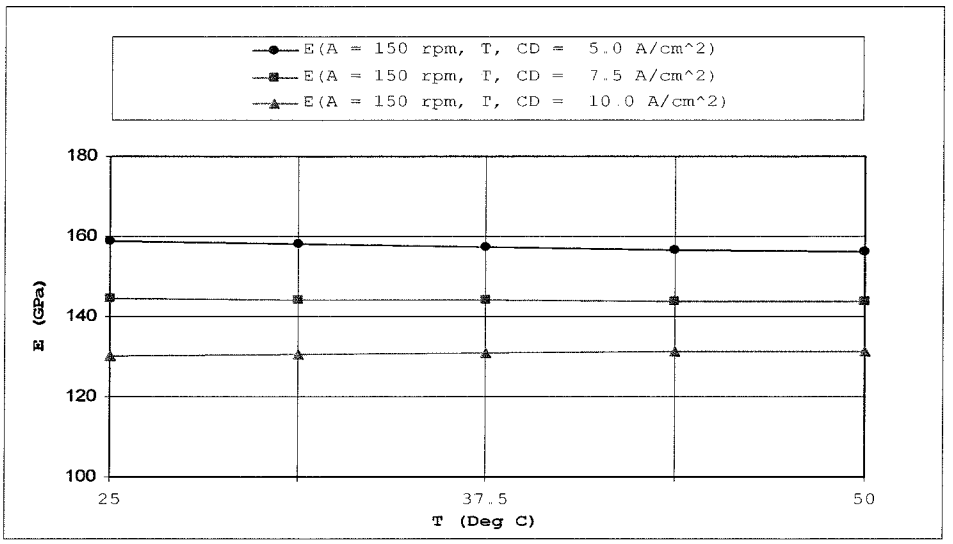

Figure 4-31: Young Modulus with varying temperature (T) and current density (C); and constant agitation (A = 150 rpm).

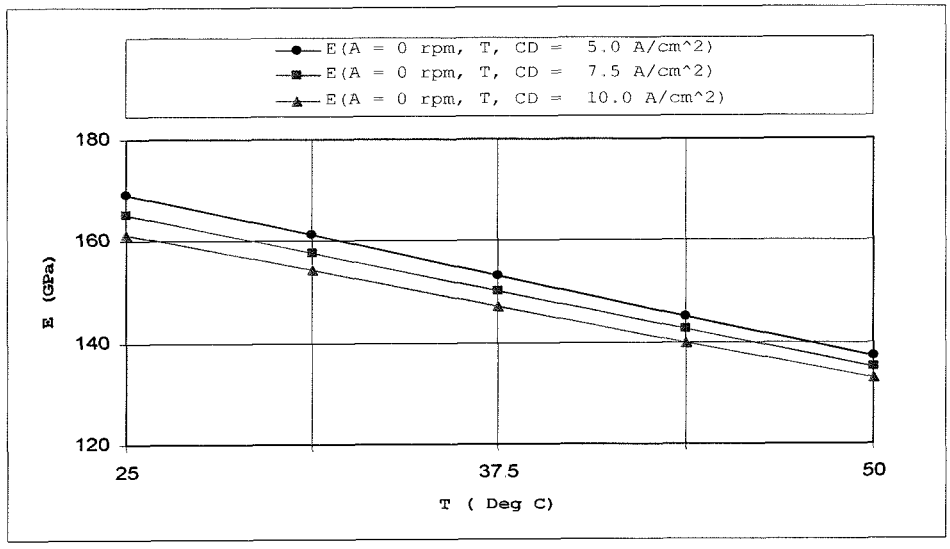

Figure 4-32: Young Modulus with varying temperature (T) and current density (C); and constant agitation (A = 0 rpm).

4.5 Results Young Modulus—Design-Expert Software

Table 4-9: Design-Expert Software Printout for Response Variable Young Modulus; ANOVA for selected factorial model; Analysis of Variance table [Partial sum of squares - Type III]

Source	Sum of Squares	df	Mean Square	F Value	p-value Prob > F
Model	4494.69	6	749.12	11245.87	*0.0072*
significant					
A-Agitation	*287.28*	*1*	*287.28*	*4312.71*	*0.0097*
B-Temperature	*1.05*	*1*	*1.05*	*15.78*	*0.1570*
C-Current Density	*1408.48*	*1*	*1408.48*	*21144.35*	*0.0044*
AB	*1748.18*	*1*	*1748.18*	*26244.00*	*0.0039*
AC	*841.12*	*1*	*841.12*	*12626.99*	*0.0057*
BC	*208.59*	*1*	*208.59*	*3131.40*	*0.0114*
Residual0.067	1	0.067			
Cor Total	4494.76	7			

The Model F-value of 11245.87 implies the model is significant. There is only a 0.72% chance that a "Model F-Value" this large could occur due to noise.

Values of "Prob > F" less than 0.0500 indicate model terms are significant.

In this case A, C, AB, AC, BC are significant model terms.

Values greater than 0.1000 indicate the model terms are not significant.

If there are many insignificant model terms (not counting those required to support hierarchy), model reduction may improve your model.

Std. Dev.	0.26	R-Squared	1.0000
Mean	139.03	Adj R-Squared	0.9999
C.V. %	0.19	Pred R-Squared	0.9991
PRESS	4.26	Adeq Precision	324.325

The "Pred R-Squared" of 0.9991 is in reasonable agreement with the "Adj R-Squared" of 0.9999.

"Adeq Precision" measures the signal to noise ratio. A ratio greater than 4 is desirable. Your ratio of 324.325 indicates an adequate signal. This model can be used to navigate the design space.

Coefficient Factor	Estimate	df	Standard Error	95% CI Low	95% CI High	VIF
Intercept	139.03	1	0.091	137.87	140.19	
A-Agitation	-5.99	1	0.091	-7.15	-4.83	1.00
B-Temperature	-0.36	1	0.091	-1.52	0.80	1.00
C-Current Density	-13.27	1	0.091	-14.43	-12.11	1.00
AB	14.78	1	0.091	13.62	15.94	1.00
AC	-10.25	1	0.091	-11.41	-9.09	1.00
BC	5.11	1	0.091	3.95	6.27	1.00

Final Equation in Terms of Coded Factors:

Young Modulus = +139.03 - 5.99 * A - 0.36 * T - 13.27 * C

+ 14.78 * A * T - 10.25 * A * C + 5.11 * T * C

Final Equation in Terms of Actual Factors:

Young Modulus = +245.46125 - 0.13053 * Agitation

- 2.43710 * Temperature - 7.33350 * Current Density

+7.88400E-003 * Agitation * Temperature

-0.027343 * Agitation * Current Density

+0.16340 * Temperature * Current Density

4.6 Design-Expert Plots: Young Modulus

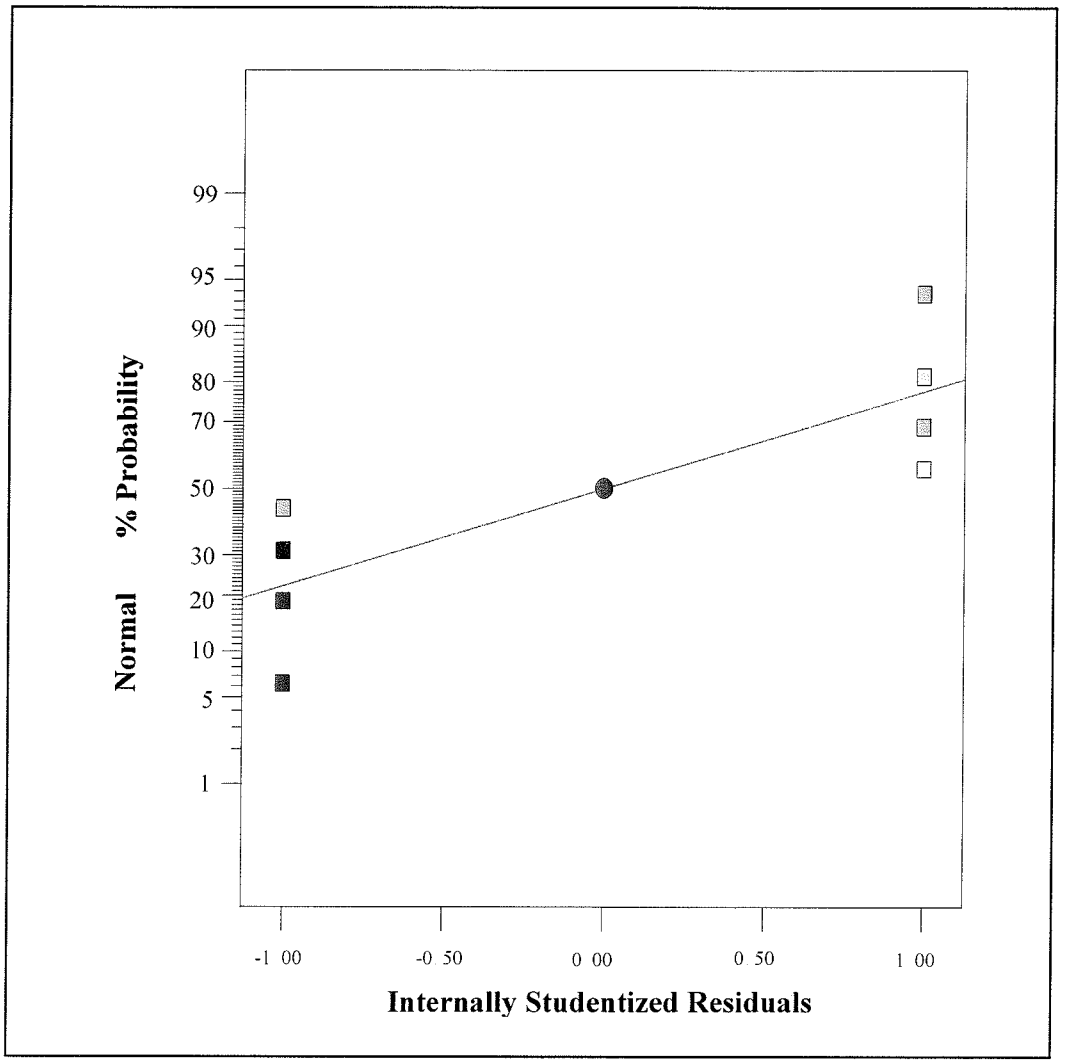

Figure 4-33: Normal Probability Plot of Residuals for Young Modulus.

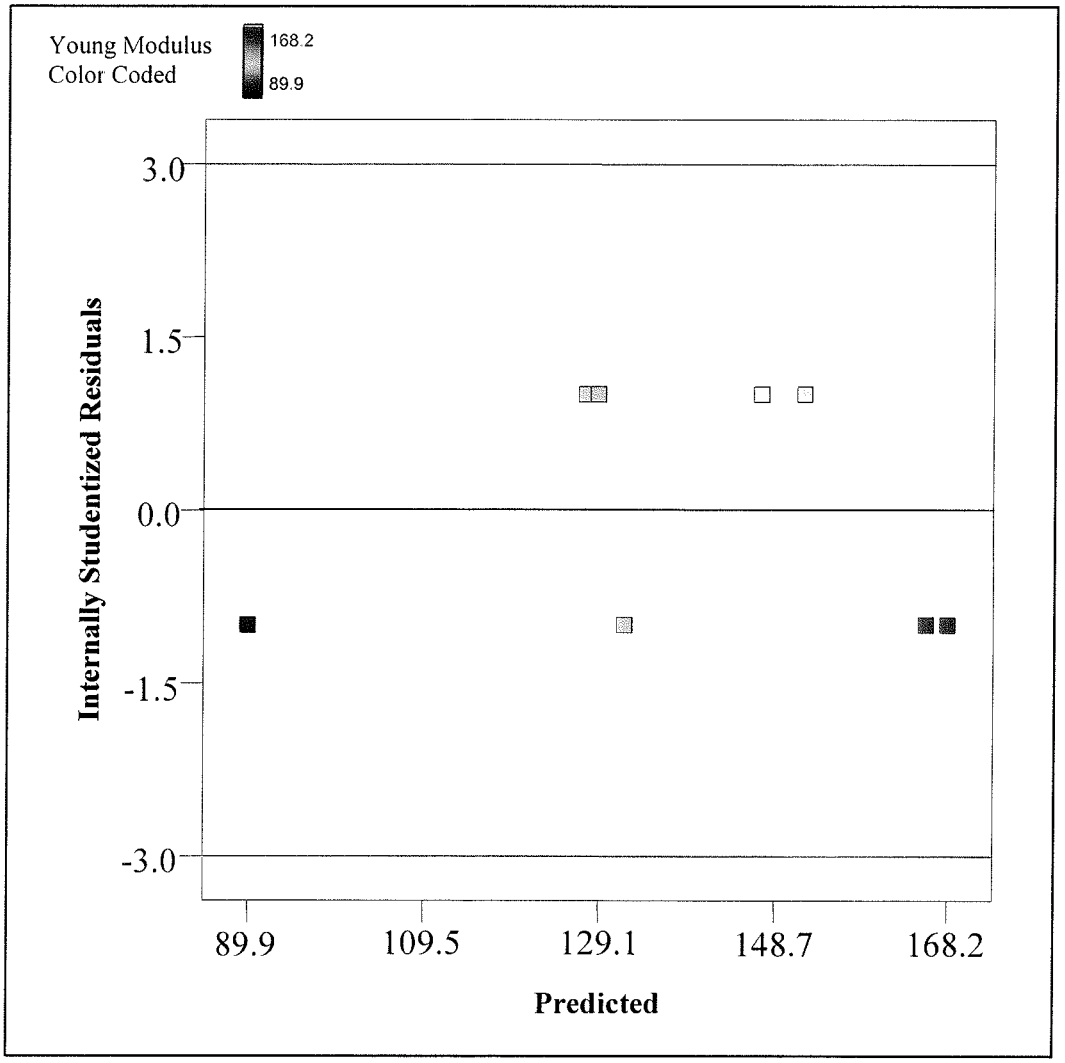

Figure 4-34: Residuals verses Predicted Plot for Young Modulus.

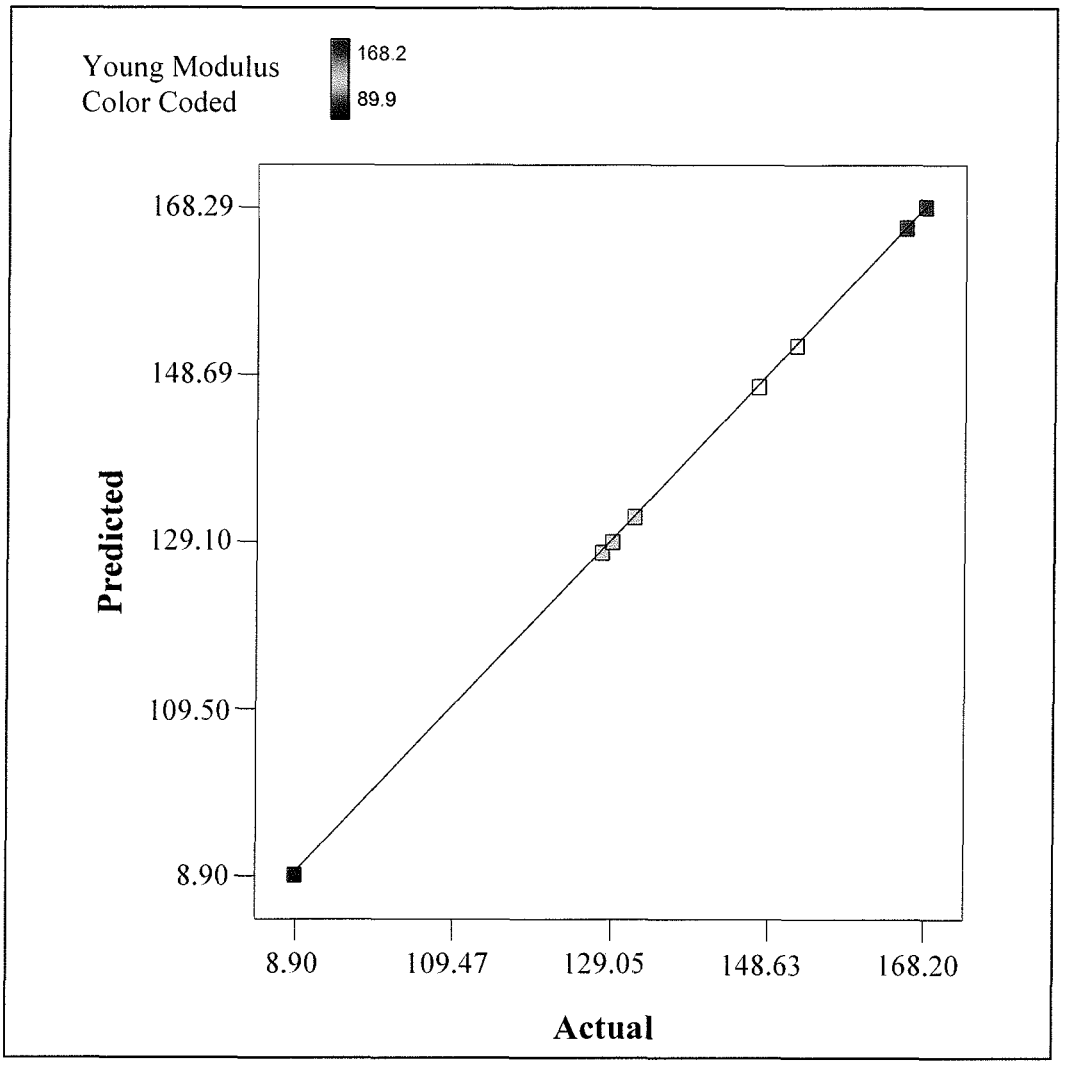

Figure 4-35: Predicted vs. Actual Value Plot for Young Modulus.

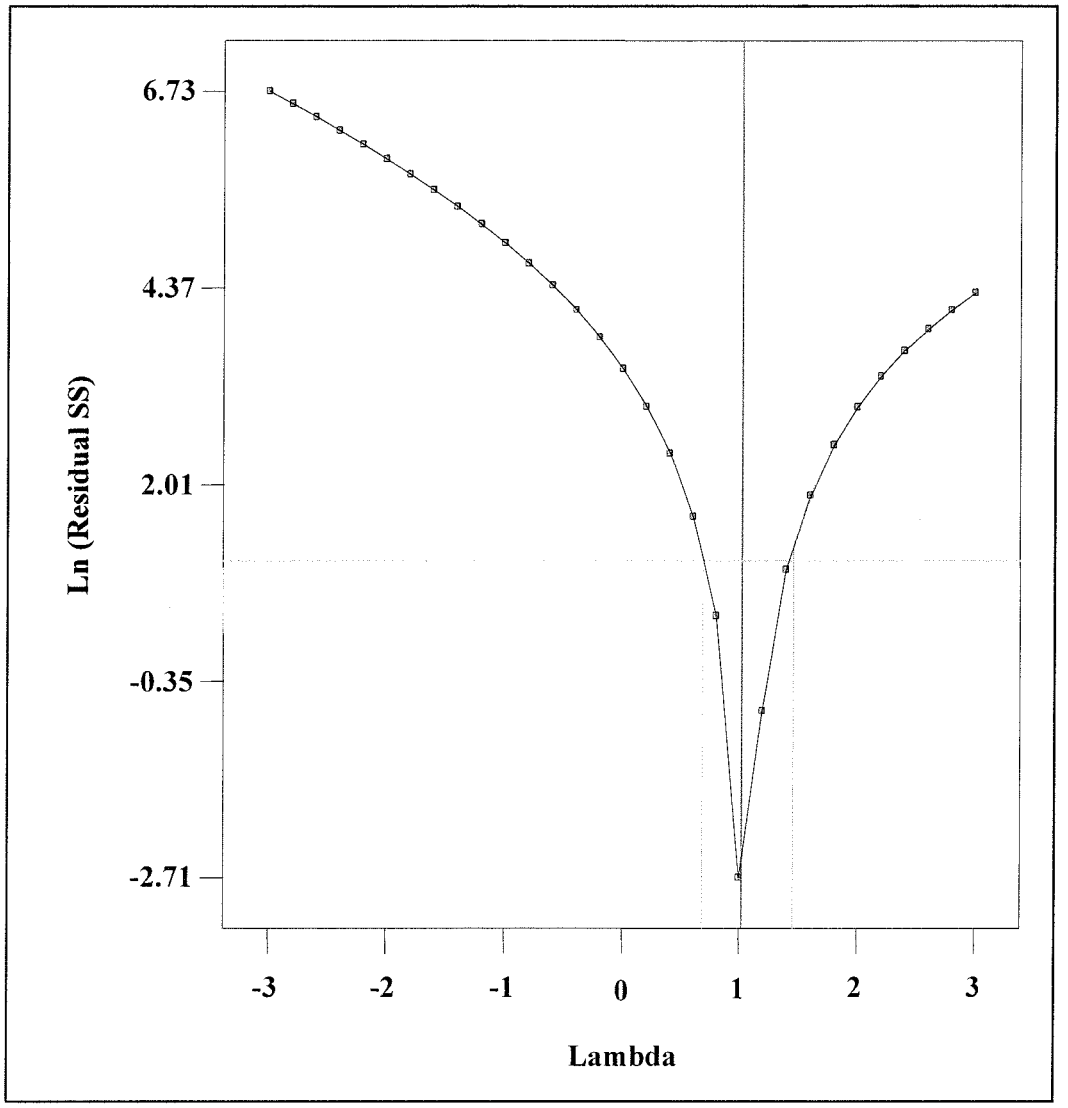

Figure 4-36: Box-Cox Plot for Power Transforms—Young Modulus. In particular, $\lambda = 1$; best fit $\lambda = 1.02$, 95% CI = (0.68, 1.46); where $BC(y:\lambda)=\begin{cases}\dfrac{y^{\lambda}-1}{\lambda} & \text{if } \lambda \neq 0 \\ \ln y & \text{if } \lambda = 0\end{cases}$.

Therefore, no Power Transforms are recommended.

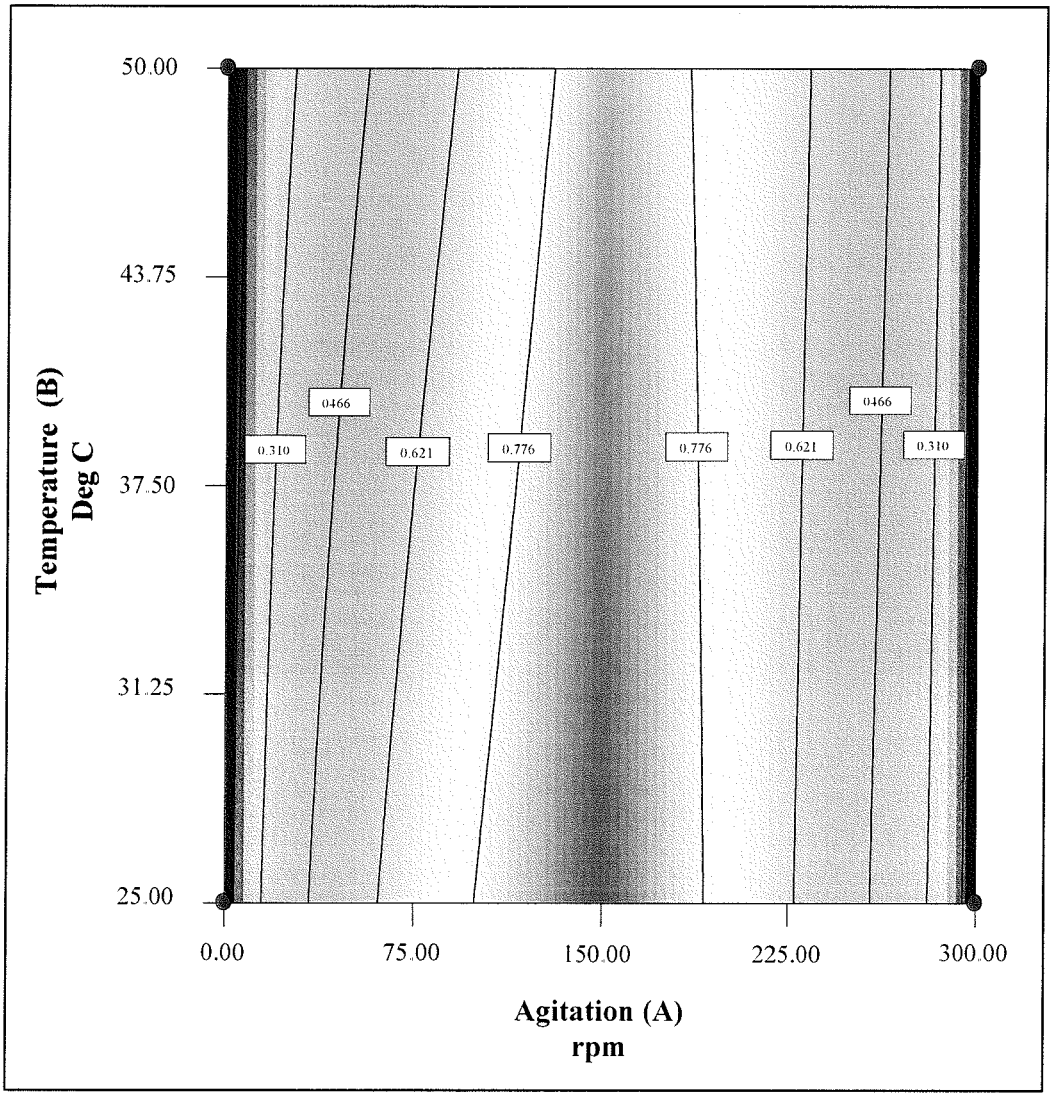

Figure 4-37: 2-D Desirability Plot for Young Modulus as a function of agitation and temperature—current density is fixed at 5.0 mA/cm^2.

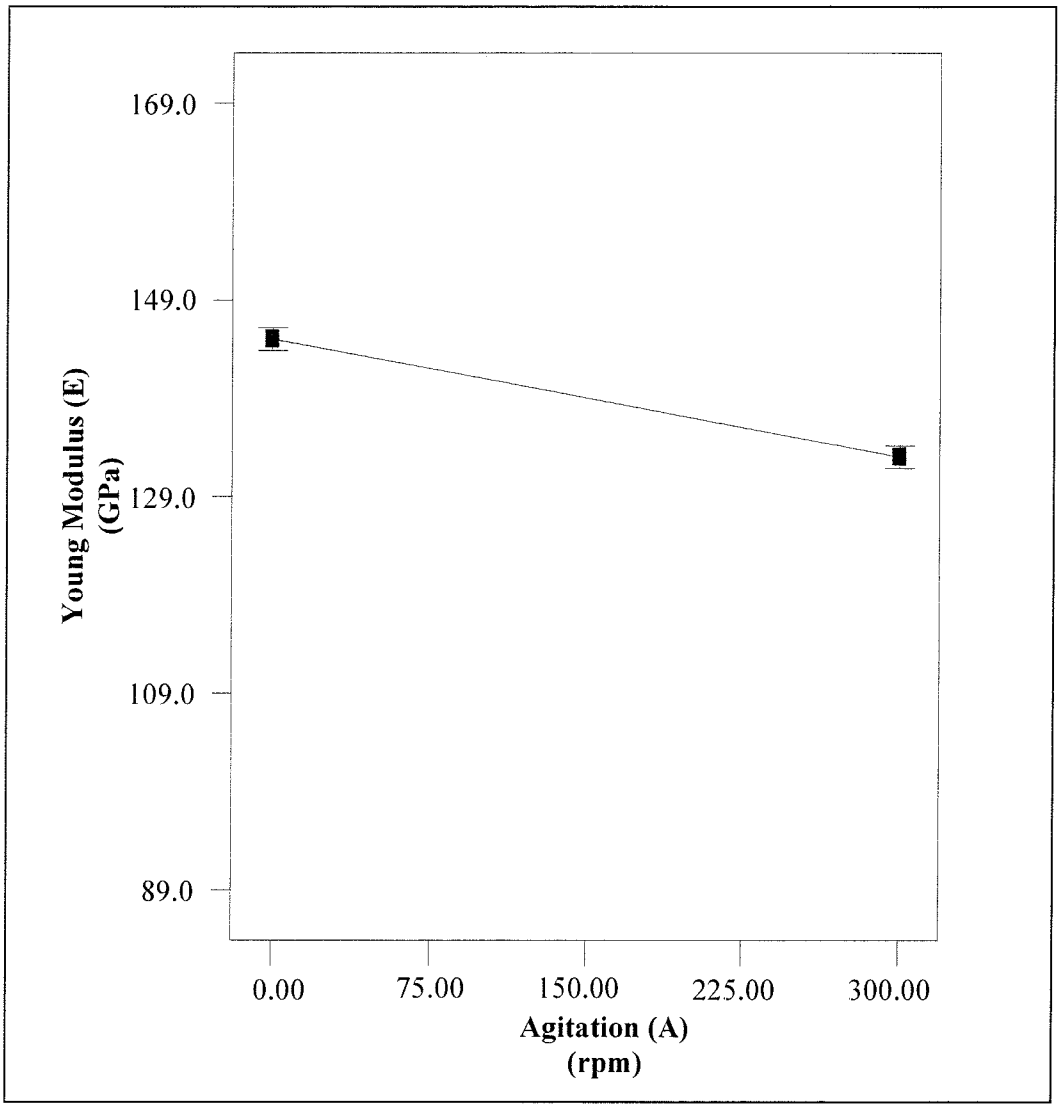

Figure 4-38: One factor plot of Young Modulus (E) as a function of agitation (A); note should be taken that agitation is also involved in an interaction. Temperature and current density are fixed at 37.50 Deg C and 7.5 mA/cm^2 respectively.

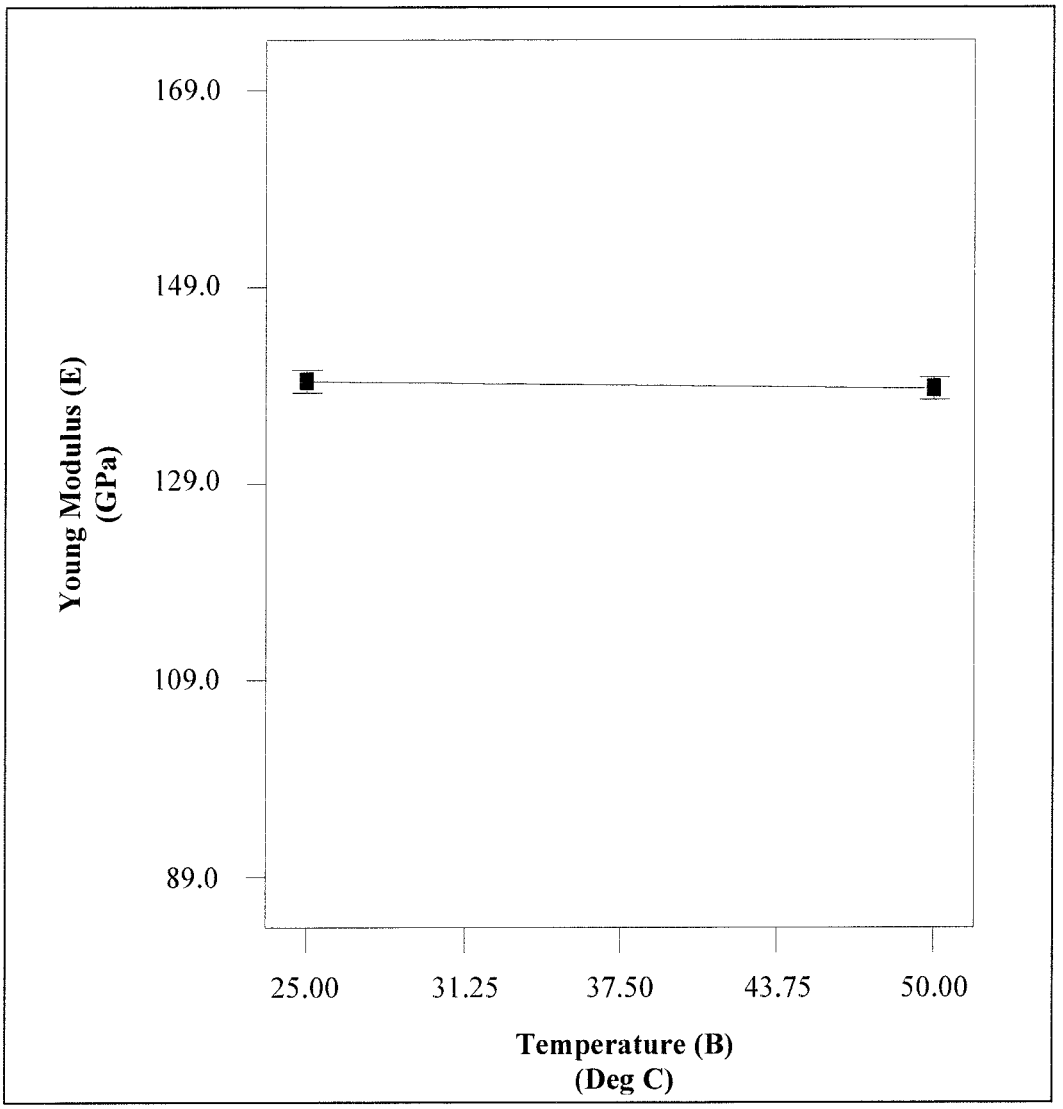

Figure 4-39: One Factor Plot of Young Modulus (E) as a function of Temperature (B); note should be taken that temperature is also involved in an interaction. Agitation and current density are fixed at 150 rpm and 7.5 mA/cm^2 respectively.

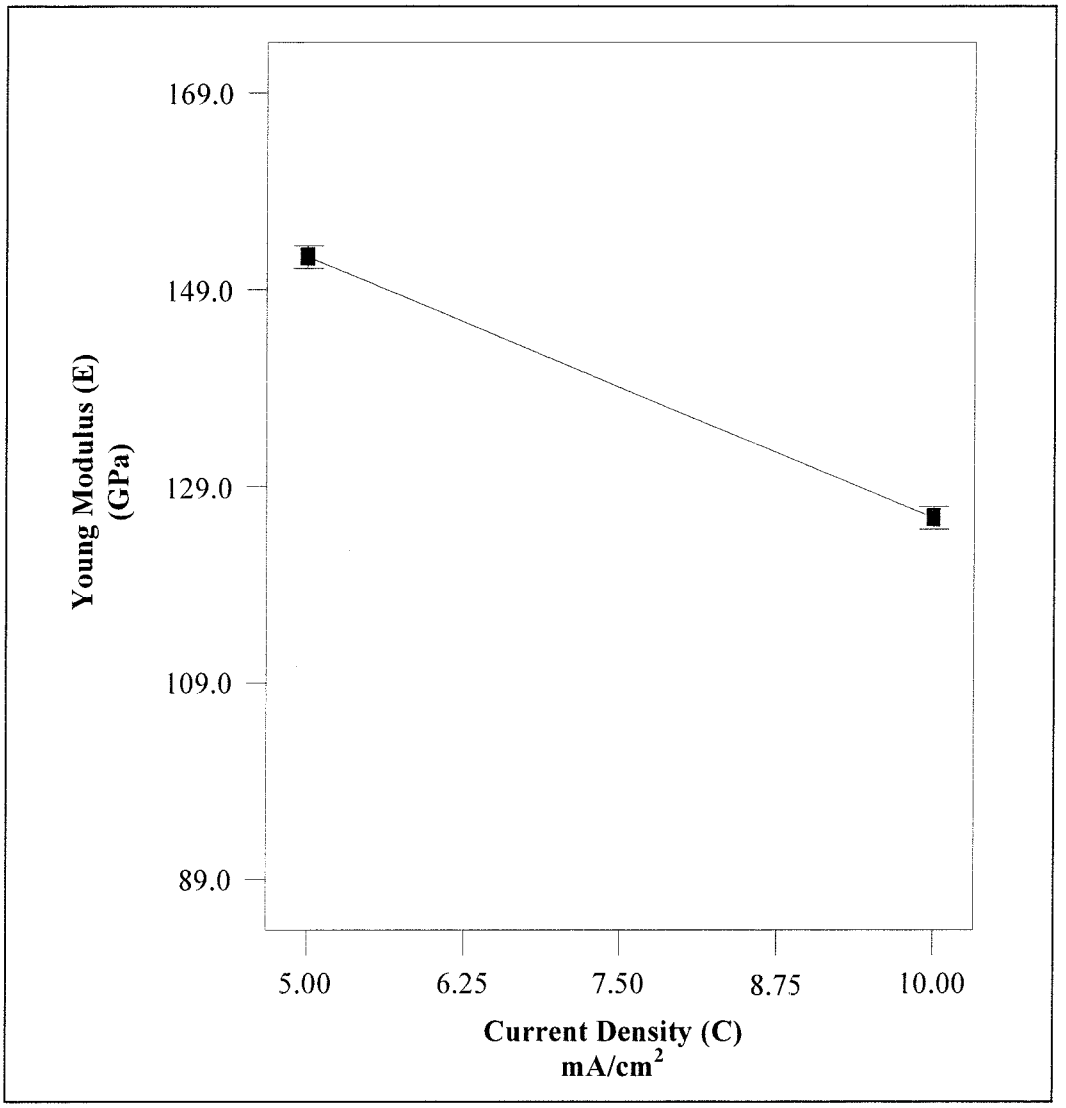

Figure 4-40: One Factor Plot of Young Modulus (E) as a Current Density C); note should be taken that temperature is also involved in an interaction Temperature and agitation are fixed at 37.50 Deg C and 150 rpm respectively.

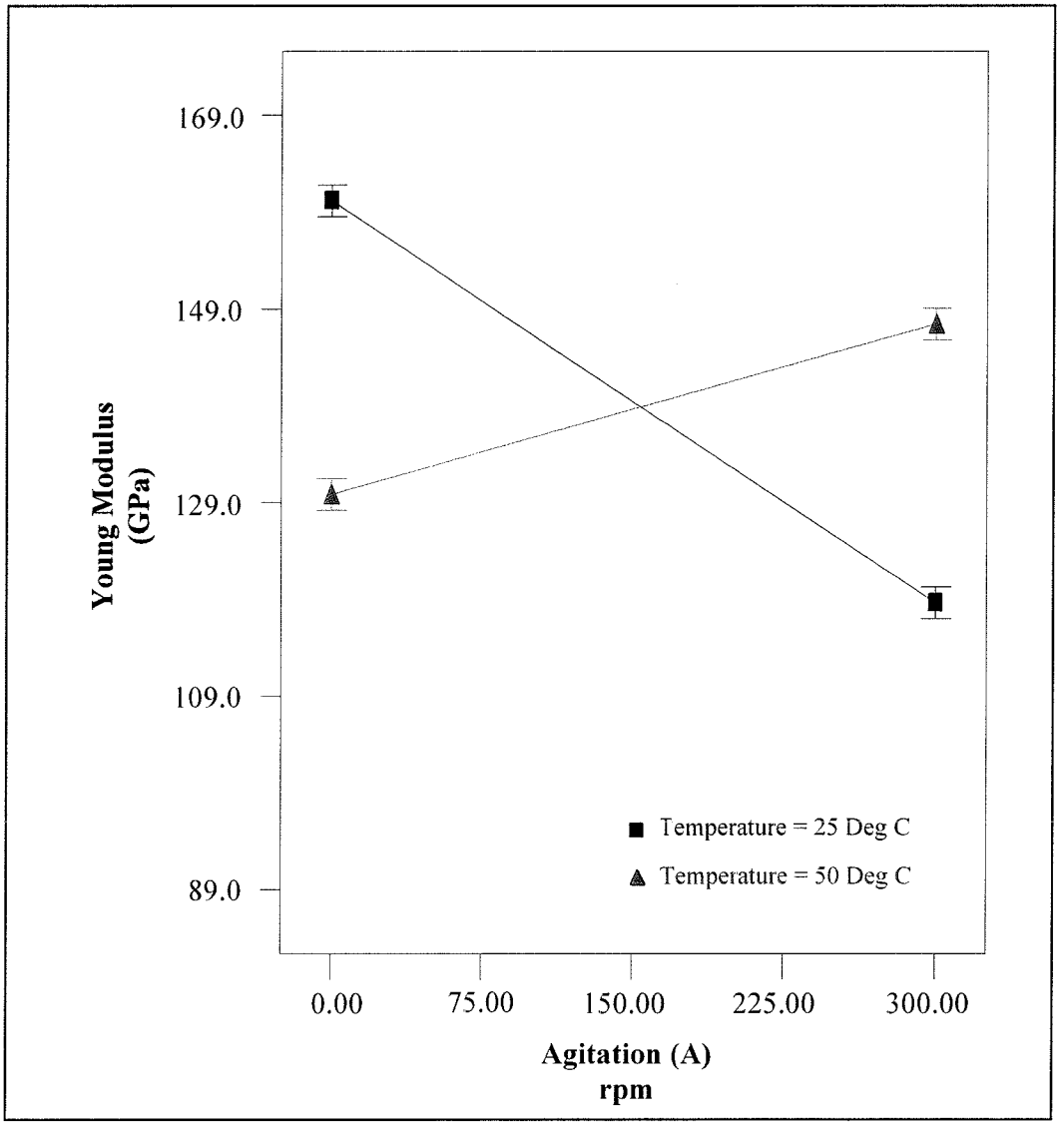

Figure 4-41: Two Factor Interaction of Young Modulus Plot as a function of agitation (A) and temperature (T). Current density (C) is fixed at 7.50 mA/cm^2.

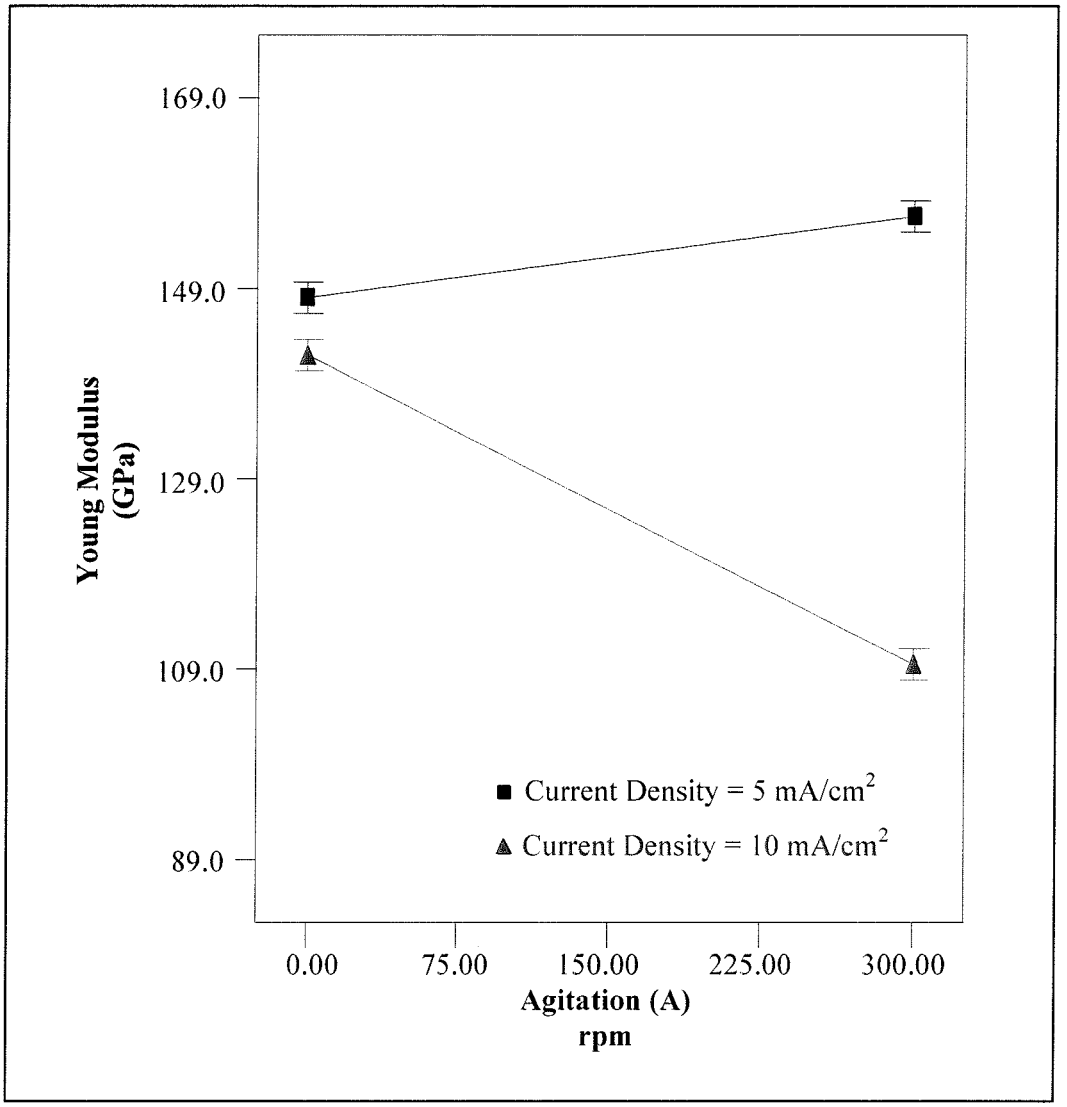

Figure 4-42: Two Factor Interaction Plot of Young Modulus as a function agitation (A) and current density (C). Temperature is fixed at 37.50 Deg C.

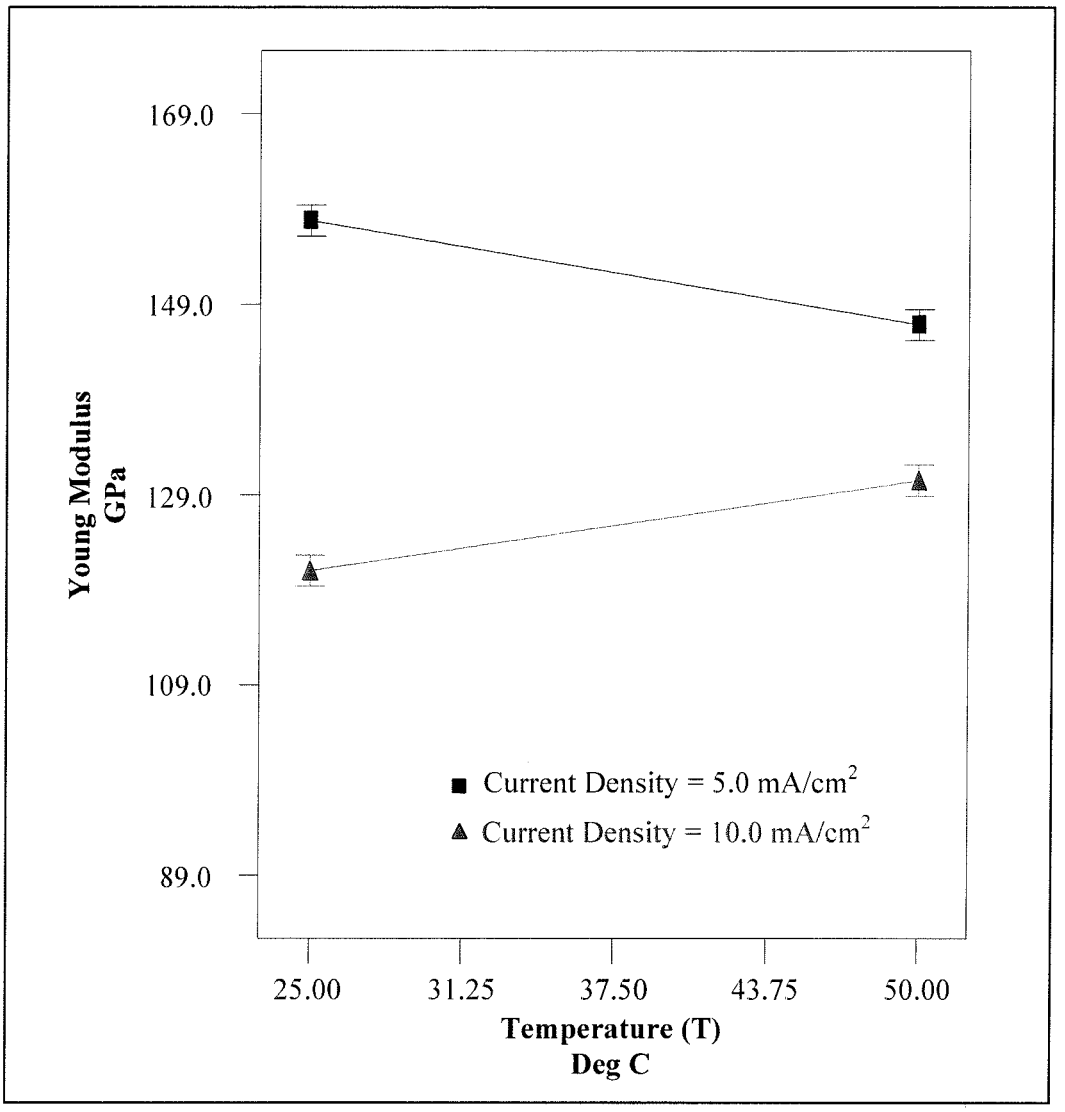

Figure 4-43: Two Factor Interaction Plot of Young Modulus as a function of temperature (T) and current density (C). Agitation is fixed at 150 rpm.

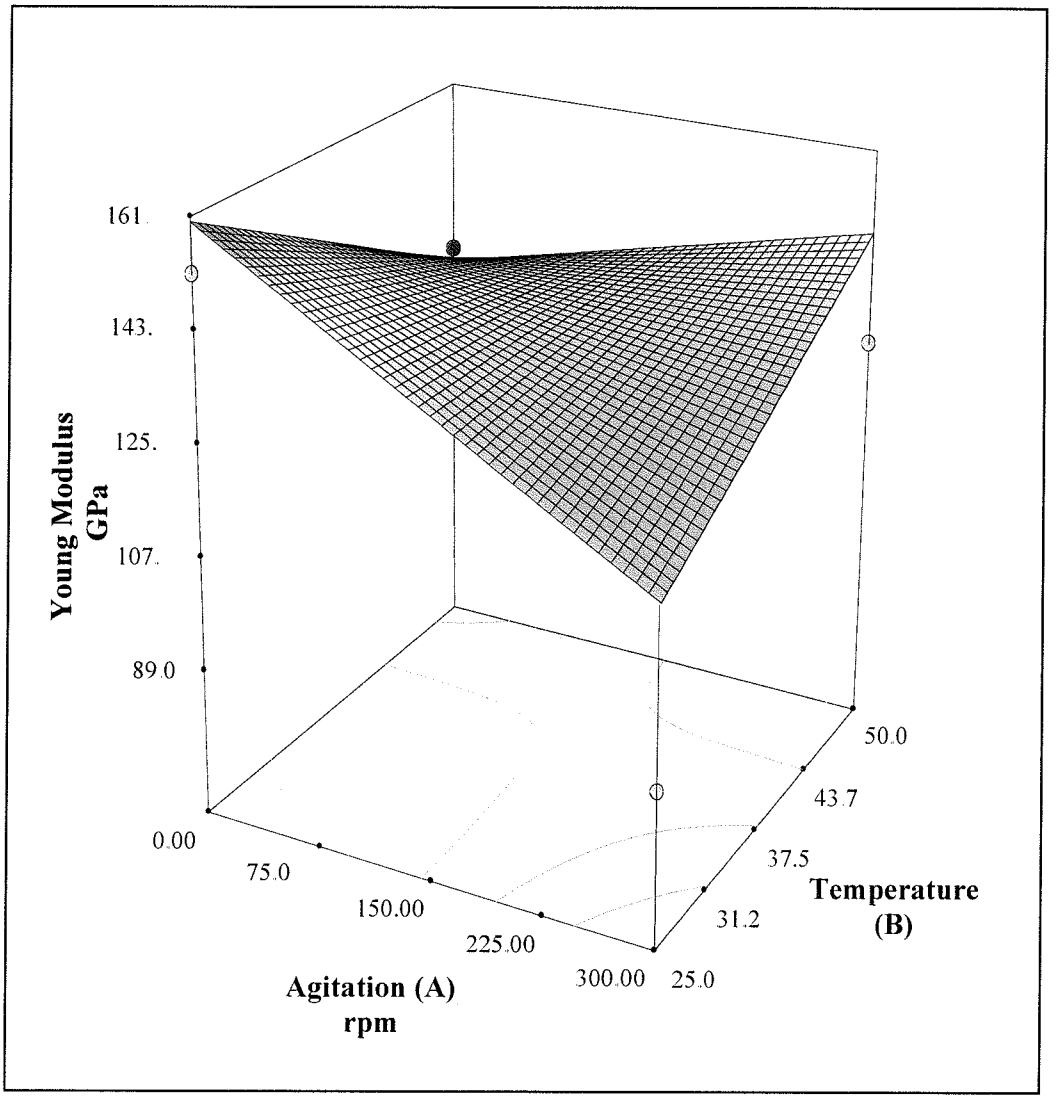

Figure 4-44: 3D Surface Plot of Young Modulus as function of agitation and temperature; current density is fixed at 10.0 A/cm^2.

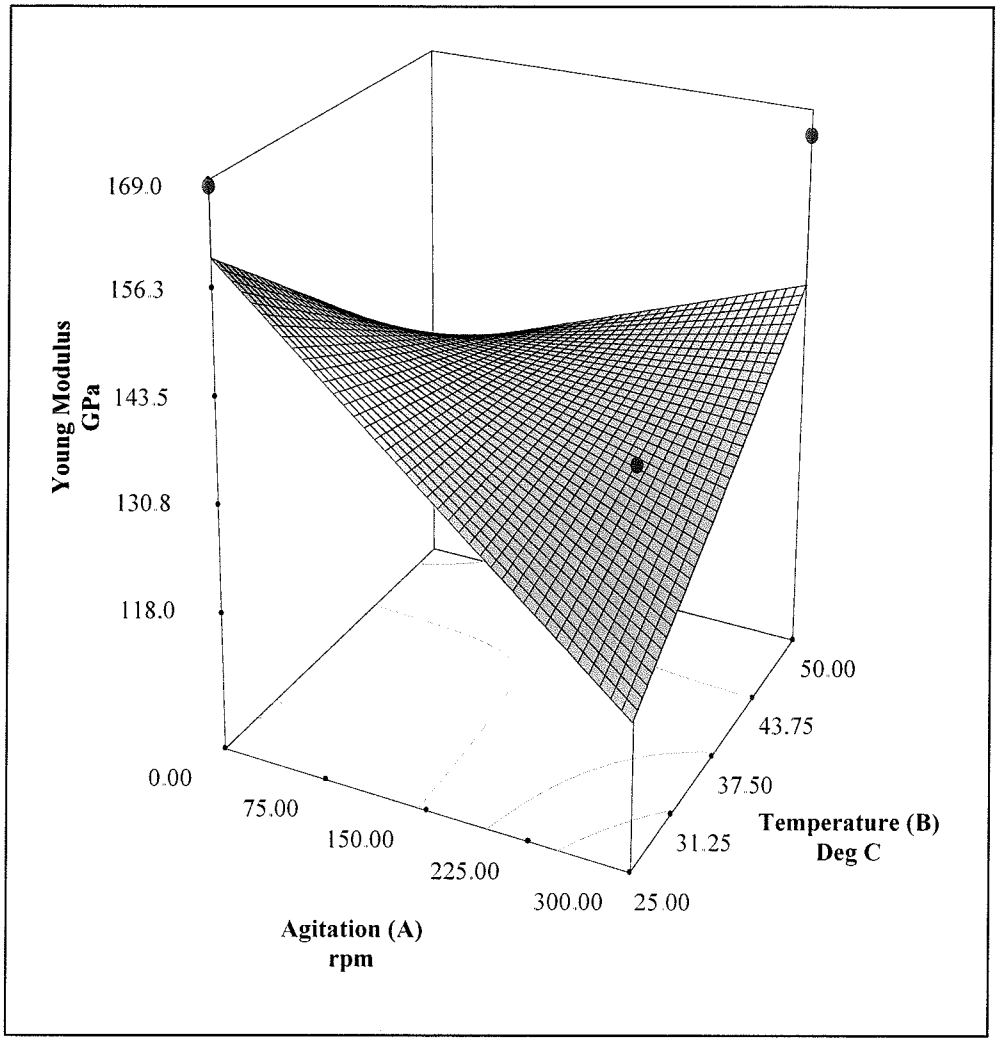

Figure 4-45: Young Modulus 3D surface Plot as function of agitation and temperature; current density is fixed at 5.0 A/cm^2.

4.7 Statistical Model: Ultimate Strength

Following the same analysis and algorithm that were conducted for Young Modulus; the main effects, and interactions can be computed in a similar matter. The three boundary conditions that were used—agitation (A), temperature (T), and current density (C)—for Young Modulus is also used for the Ultimate Strength (σ_{ult}).

Similarly, the levels of the factors are arbitrarily called "low" and "high." There are eight treatment combinations in this design, and are shown geometrically as a cube, see Figures 4-46 and 4-47.

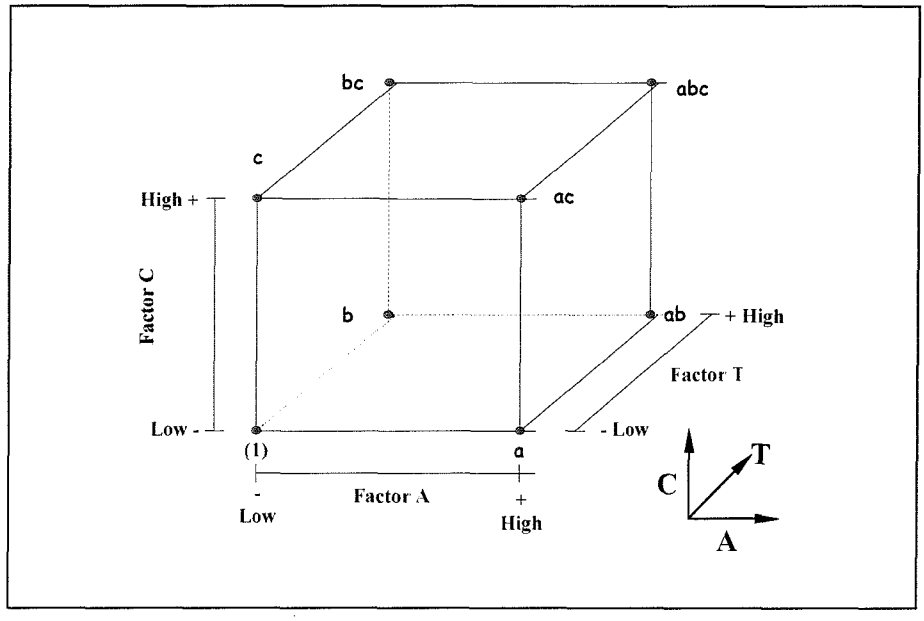

Figure 4-46: Treatment combinations in the 2^3 design.

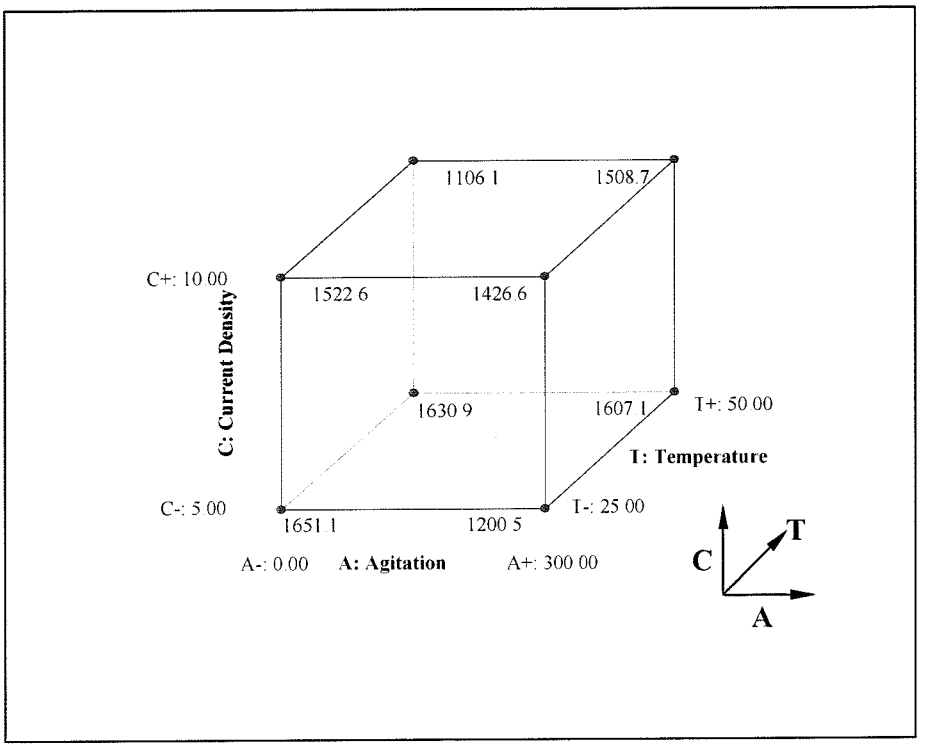

Figure 4-47: Treatment combinations in the 2^3 design with σ_{ult} values.

The treatment combinations along with σ_{ult} values are shown in Table4-10a and Table 4-10b.

Table 4-10a: Measured σ_{ult} values and standard deviation for each test case.

Ultimate Strength (σ_{ult})						
Test Specimen	**A (MPa)**	**B (MPa)**	**C (MPa)**	**D (MPa)**	**Mean (MPa)**	**Standard Deviation (MPa)**
1B2		1351.8	1665.6		**1508.7**	**221.9**
1B4	1168.9	977.3	1213.0	1065.2	**1106.1**	**105.9**
1B1	1398.7	1384.6	1588.1	1335.2	**1426.7**	**111.0**
9B1	1631.7		1413.55		**1522.6**	**154.3**
2B6		1691.23	1524.11		**1607.1**	**118.2**
2B8	1678.56	1681.55	1532.59		**1630.9**	**85.2**
10B5		1127.7	1273.21		**1200.5**	**102.9**
10B7	1705.9	1385.7	1719.3	1793.7	**1651.1**	**181.1**

Table 4-10b: Algebraic Sign for Calculating Effects in the 2^3 Design.

Treatment Combination	Factorial Effect								
	I	A	T	AT	C	AC	TC	ATC	σ_{ult} (MPa)
abc	+	+	+	+	+	+	+	+	1508.72
bc	+	-	+	-	+	-	+	-	1106.13
ac	+	+	-	-	+	+	-	-	1426.60
c	+	-	-	+	+	-	-	+	1522.63
ab	+	+	+	+	-	-	-	-	1607.07
b	+	-	+	-	-	+	-	+	1630.90
a	+	+	-	-	-	-	+	+	1200.46
(1)	+	-	-	+	-	+	+	-	1651.134

Next, consider estimating the boundary conditions' main effect. The effect of agitation (A) when temperature (T) and current density (C) are at the low level is given by

$$[a-(1)]/n \qquad 4\text{-}2$$

Similarly, the effect of agitation when temperature (T) is at high level and current density (C) is at low level is given by

$$[ab - b]/n \qquad 4\text{-}3$$

Continuing, the effect of agitation (A) when current density (C) is at high level and temperature (T) is at low level is given by

$$[ac - c]/n \qquad 4\text{-}4$$

Finally, the effect of agitation (A) when both temperature (T) and current density (C) are at high level is given by:

$$[abc - bc]/n \qquad 4\text{-}5$$

Thus, the average effect of agitation (A) is given by

$$Effect\ of\ Agitation\ or\ A = \overline{E}_{A^+} - \overline{E}_{A^-} \qquad 4\text{-}6$$

or it can be computed as the average of equations 4-2, 4-3, 4-4, and 4-5, i.e.

$$Effect\ of\ Agitation\ or\ A = \frac{1}{4n}[a - (1) + ab - b + ac - c + abc - bc] \qquad 4\text{-}7$$

This equation can also be developed as a contrast between four treatment combinations in the right face of the cube (where A is at high level), and the four in the left face (where A is at low level) shown in Figure 4-48. That is, the A effect is just the average

of the four runs where A is at the high level ($\overline{E}_{A^+}$) minus the average of four runs where A is at the low level ($\overline{E}_{A^-}$) or

$$A = \frac{a+ab+ac+abc}{4n} - \frac{(1)+b+c+bc}{4n} \qquad 4\text{-}8$$

Rearrange equation 4-8, yields

$$A = \frac{1}{4n}[a+ab+ac+abc-(1)-b-c-bc] \qquad 4\text{-}9$$

Hence, using the values corresponding to the treatment conditions shown in Table 9 yields the following value:

$$A = \frac{1}{4}[1200.46 + 1607.07 + 1426.60 + 1508.72$$

$$- 1651.134 - 1630.90 - 1522.63 - 1106.13]$$

$$A = \frac{1}{4}[-167.944] = -41.986$$

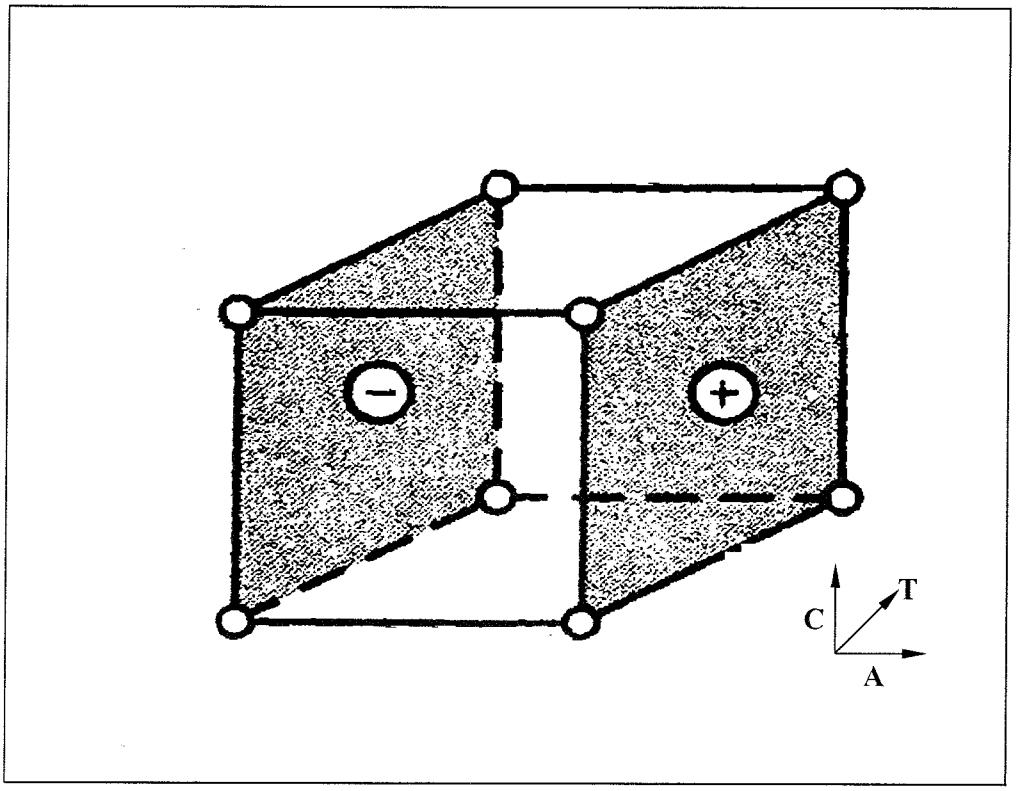

Figure 4-48: Ultimate Stress' Main Effect of Agitation (A).

In a similar manner, the effect of temperature (T) is the difference in averages between the four treatment combinations in the front face of the cube and the four in the back, shown in Figure 4-49.

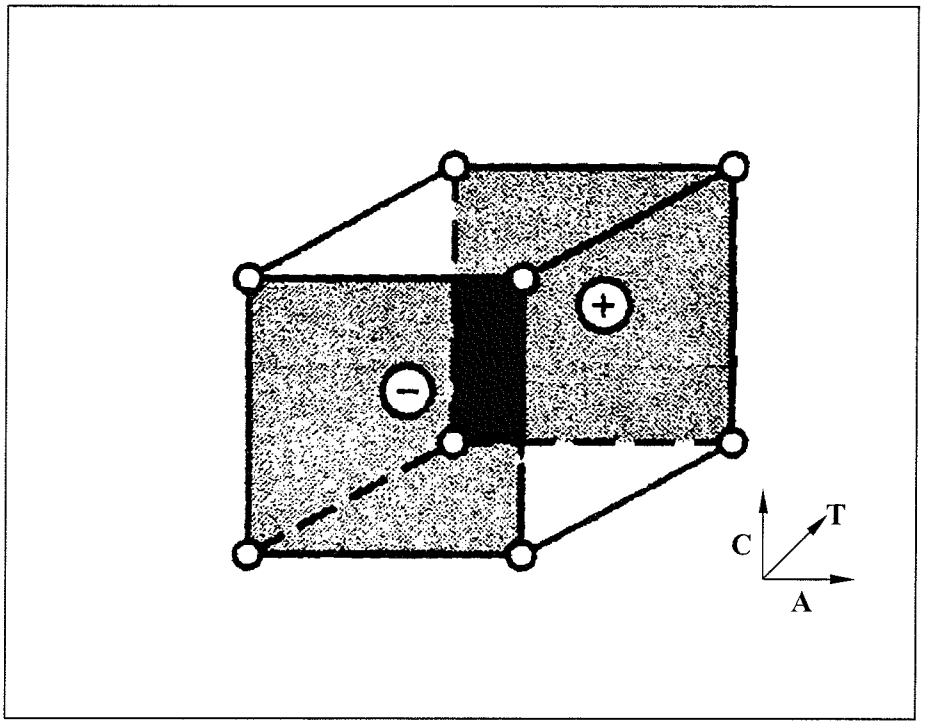

Figure 4-49: Ultimate Stress' Main Effect of Temperature (T).

This yield

$$Effect\ of\ Temperature\ or\ T = \bar{E}_{Temp^+} - \bar{E}_{Temp^-} \qquad 4\text{-}10$$

which yields

$$T = \frac{1}{4n}[b + ab + bc + abc - (1) - a - c - ac] \qquad 4\text{-}11$$

Again, using the values corresponding to the treatment conditions shown in Table 4-9 yields the following value:

$$T = \frac{1}{4}[1630.90 + 1607.07 + 1106.13 + 1508.72 - 1651.134$$

$$- \ 1200.46 - 1522.63 - 1426.60]$$

$$T=\frac{1}{4}[51.996]=12.999$$

The effect of current density (C) is the difference in the averages between the four treatment combinations in the top face of the cube and the four in the bottom, as shown in Figure 4-50.

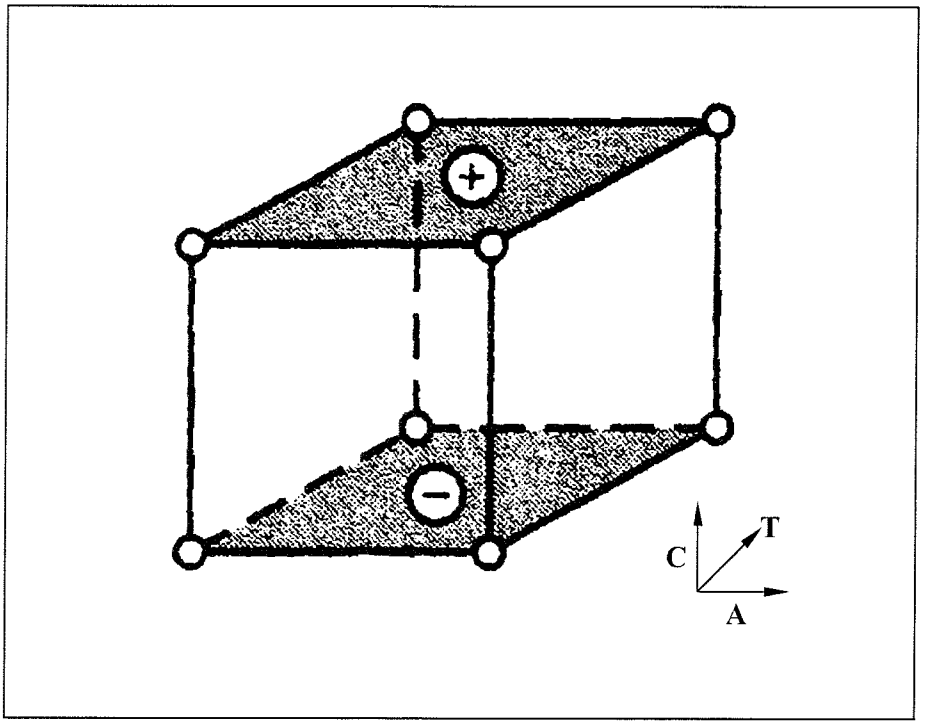

Figure 4-50: Ultimate Stress' Main Effect of Current Density (C).

that is

$$Effect\ of\ Current\ Density\ or\ C=\overline{E}_{Current\ Density^{+}}-\overline{E}_{Current\ Density^{-}} \qquad 4\text{-}12$$

Using the values corresponding to the treatment conditions shown in Table 4-9 yields the following value:

$$C=\frac{1}{4}[1522.63 + 1426.60 + 1106.13 + 1508.72 - 1651.134$$

$$- 1200.46 - 1630.90 - 1607.07]$$

$$C=\frac{1}{4}[-525.484] = -131.371$$

The two-factor interaction effects may be computed easily, for example the measure of the agitation-temperature (AT) interaction is the difference between the average agitation effects at the two-levels of temperature (T). By convention, one-half of this difference is called the agitation-temperature, symbolically shown in Table 4-10. Because the agitation-temperature is one-half of this difference, the effect of agitation-temperature is given by

$$AT=\frac{[abc-bc+ab-b-ac+c-a+(1)]}{4n} \qquad 4\text{-}14$$

Table 4-11: Agitation-Temperature (AT) Interaction Calculation.

Temperature (T)	Average Agitation (A) Effect
High (+)	$\frac{[(abc-bc)+(ab-b)]}{2n}$
Low (-)	$\frac{[(ac-c)+(a-(1))]}{2n}$
Difference	$\frac{[abc-bc+ab-b-ac+c-a+(1)]}{2n}$

Substituting the values shown in Table 4-11 for the corresponding to the treatment conditions yields:

$$AT=\frac{1}{4}[1508.72 + 1106.13 + 1607.07 + 1630.90 - 1426.60$$

$$- 1522.63 - 1200.46 - 1651.134]$$

$$AT=\frac{1}{4}[925.464] = 29.565$$

Rewriting AT in equation 4-14, yields

$$AT=\frac{abc+ab+c+(1)}{4n} - \frac{bc+b+ac+a}{4n} \qquad 4\text{-}15$$

And in this form, the AT interaction is easily seen to be the difference in averages between runs on two diagonal planes in the cube shown in Figure 4-51.

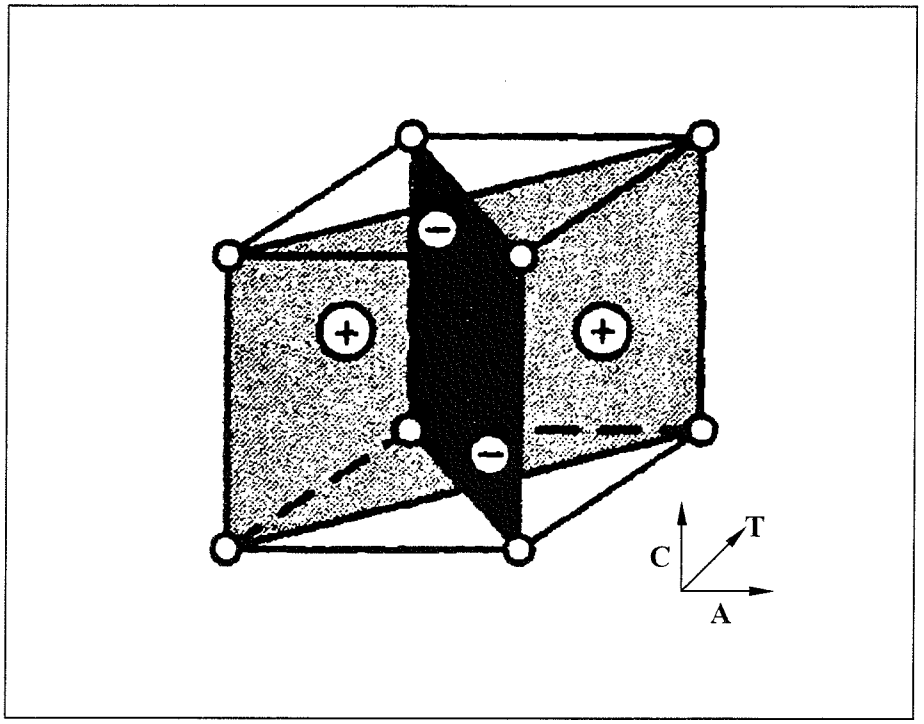

Figure 4-51: Ultimate Stress' Agitation-Temperature (AT) interaction.

Using similar logic, and referring to Figures 4-52 and 4-53; the agitation-current density and temperature-current density interactions are:

$$AC=\frac{1}{4n}[(1)-a+b-ab-c+ac-bc+abc] \qquad 4\text{-}16$$

$$TC=\frac{1}{4n}[(1)+a-b-ab-c-ac+bc+abc] \qquad 4\text{-}17$$

Using the values corresponding to the treatment conditions shown in Table 4-9 yields the following values:

$$AC=\frac{1}{4}[1651.134 - 1200.46 + 1630.90 - 1607.07 - 1522.63$$

$$+ 1426.60 - 1106.13 + 1508.72]$$

$$AC = \frac{1}{4}[781.064] = 195.266$$

$$TC = \frac{1}{4}[1651.134 + 1200.46 - 1630.90 - 1607.07 - 1522.63 - 1426.60 + 1106.13 + 1508.72]$$

$$TC = \frac{1}{4}[-720.756] = -180.189$$

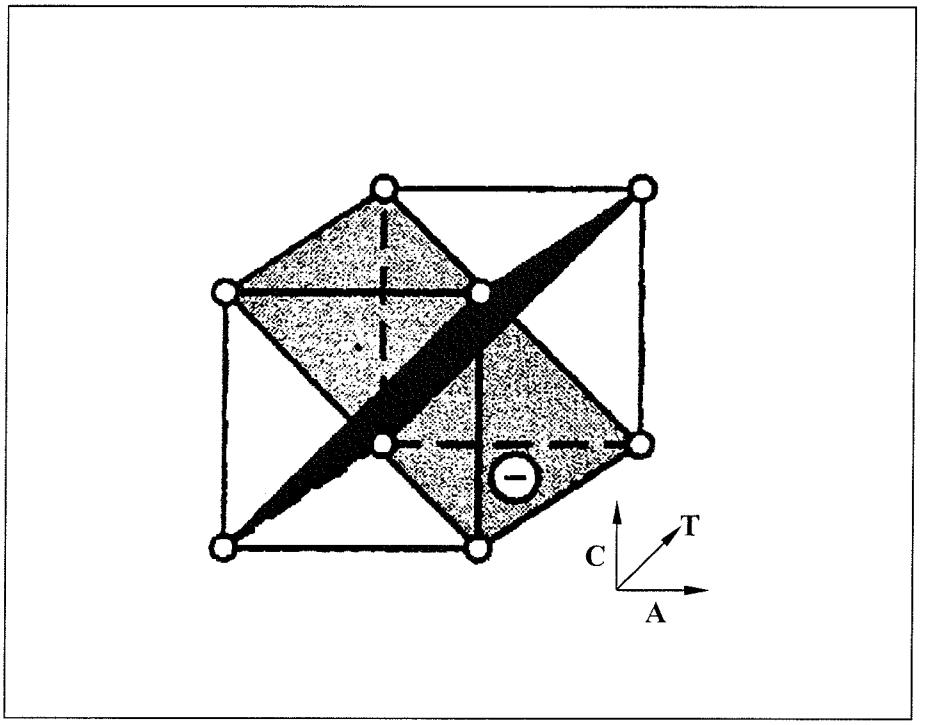

Figure 4-52: Ultimate Stress' Agitation-Current Density (AC) interaction.

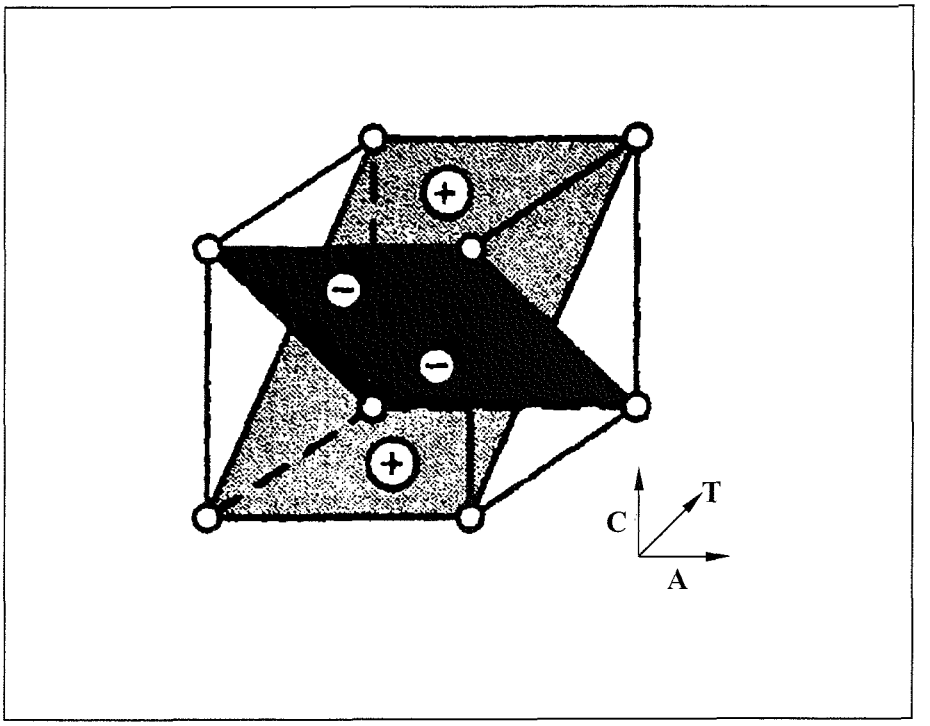

Figure 4-53: Ultimate Stress' Temperature-Current Density (TC) interaction.

Finally, agitation-temperature-current density (ATC) interaction is defined as the average difference between the agitation-temperature interactions for the two different levels of current density, see Figure 4-54. Thus agitation-temperature-current density effect is given by:

$$ATC = \frac{1}{4n}[abc - bc - ac + c - ab + b + a - (1)] \qquad 4\text{-}18$$

Substituting the values from Table 4-9 yields

$$ATC = \frac{1}{4}[1508.72 - 1106.13 - 1426.60 + 1522.63 - 1607.07$$

$$+ 1630.90 + 1200.46 - 1651.134]$$

$$ATC = \frac{1}{4}[71.776] = 17.944$$

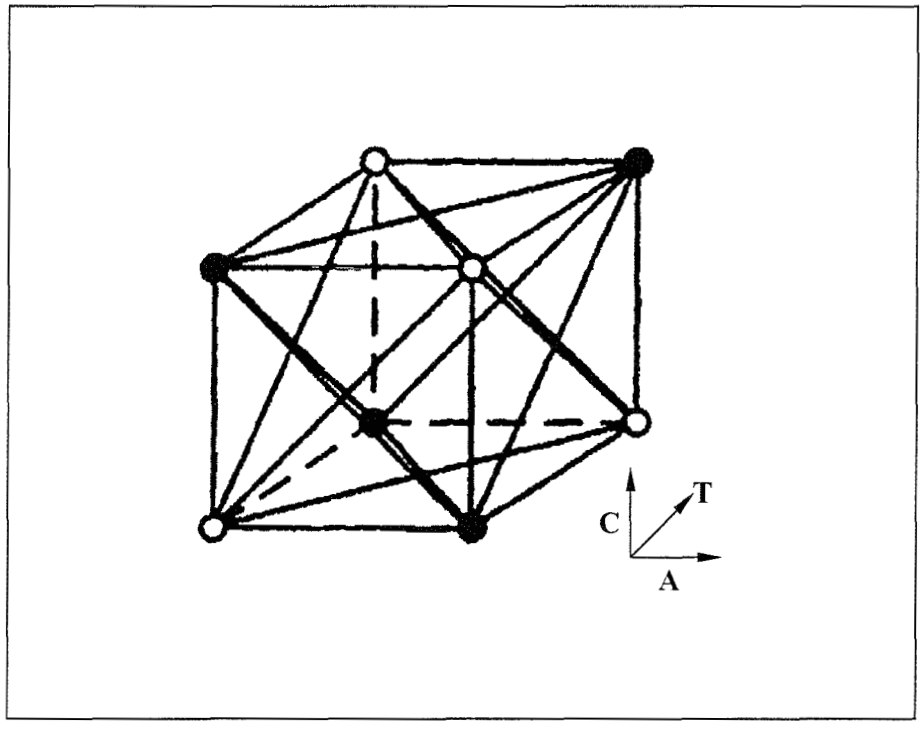

Figure 4-54: Ultimate Stress' Agitation-Temperature-Current Density (ATC) interaction.

In equations: 4-9, 4-11, 4-13, 4-14, 4-16, 4-17, and 4-18, the quantities in the brackets are *contrasts* in the treatment combinations. A table of plus and minus signs can be developed from the contrasts; and once the signs for the main effects have been established the signs for the remaining columns can be obtained by multiplying the appropriate preceding columns, row by row—this is shown in Table 4-9.

Table 4-5 has several interesting properties: (1) except for column *I*, every column has an equal number of plus and minus signs; (2) the sum of the products of the signs in any two columns is zero; (3) column *I* multiplied times any column leaves that

column unchanged, i.e. *I* is an identity element; and (4) the product of any two columns yields a column in the table. For example

$$A \times T = AT, \text{ and}$$

$$AT \times T = AT^2 = A$$

Hence, the exponents in the products are formed by using ***modulus-2*** arithmetic. (That is, the exponent can only be 0 or 1; if it is greater than 1, it is reduced by multiples of 2 until it is either 0 or 1.) All of these properties are implied by the orthogonality of the contrasts used to estimate the effects.

As a result, the Sums of squares for the effects are easily computed, because each effect has a corresponding single-degree-of-freedom contrast. In the 2^3 design with n replicates, the sum of squares for any effect is

$$SS = \frac{(contrast)^2}{8n} \qquad 4\text{-}19$$

Hence, from 4-9, 4-11, 4-13, 4-14, 4-16, 4-17 and 4-18 the main effect for:

- agitation (A) = -41.986
- temperature (T) = 12.999
- current density (C) = -131.371
- agitation-temperature AT = 231.366
- agitation-current density (AC) = 195.266
- temperature-current density (TC) = -180.189
- agitation-temperature-current density (ATC) = 17.944

Therefore, the Sums of squares are calculated using equation 4-19 as follows:

$$SS_{Agitation} = SS_A = \frac{(-167.994)^2}{8} = 3{,}525.65$$

$$SS_{Temperature} = SS_T = \frac{(51.966)^2}{8} = 337.95$$

$$SS_{Current\ Density} = SS_C = \frac{(-525.484)^2}{8} = 3{,}4516.68$$

$$SS_{Agitation-Temperature} = SS_{AT} = \frac{(925.464)^2}{8} = 107{,}060.45$$

$$SS_{Agitation-Current\ Density} = SS_{AC} = \frac{(781.064)^2}{8} = 76{,}257.62$$

$$SS_{Temperature-Current\ Density} = SS_{TC} = \frac{(-720.756)^2}{8} = 64{,}936.15$$

$$SS_{Agitation-Temperature-Current\ Density} = SS_{ATC} = \frac{(71.776)^2}{8} = 643.97$$

Table 4-12: Effect Estimate Summary for Ultimate Strength σ_{ult}; "*" values were calculated using the Design-Expert Software.

Factor	Effect of Estimate	Sum of Squares	Percent Contribution
Model*		2.866E+005	
A	-41.986	3525.65	1.23
T	12.999	337.95	0.12
C	-131.371	34516.68	12.02
AT	231.366	107060.45	37.27
AC	195.266	76257.62	26.54
TC	-180.189	64936.15	22.60
ATC	17.944	643.97	0.22
Pure Error			
Total		287,278.47	

Using the classical method, the total sum of squares is given by:

$$SS_{Total} = \sum_{i=1}^{a}\sum_{j=1}^{b}\sum_{k=1}^{c}\sum_{l=1}^{n}\sigma^2{}_{(ult)_{ijkl}} - \frac{\sigma^2{}_{(ult)_{....}}}{abcn} \qquad 4\text{-}20$$

In particular, this yields the following:

$$SS_{Total} = \sum_{i=1}^{2}\sum_{j=1}^{2}\sum_{k=1}^{2}\sum_{l=1}^{1}\sigma^2{}_{(ult)_{ijkl}} - \frac{\sigma^2{}_{(ult)_{....}}}{8}$$

Table 4-13: Ultimate Strength (σ_{ult}) from Experiment

Agitation (rpm)	Current Density (mA/cm^2)				σ_{ult} (MPa)
	5		10		
	Temperature (Deg C)		Temperature (Deg C)		
	25	50	25	50	
0	1651.134	1630.90	1522.63	1106.13	5910.79
300	1200.46	1607.07	1426.60	1508.72	5742.85
$\sigma_{(ult)ijk}$	2851.59	3237.97	2949.23	2614.85	11653.64 = σ_{ult}

Using the experimental data for the given boundary conditions, shown in Table 4-13, yields:

$$SS_{Total} = (1651.134)^2 + (1200.46)^2 + (1630.90)^2 + (1607.07)^2 + (1522.63)^2 + (1426.60)^2 + (1106.13)^2 + (1508.72)^2 - \frac{11653.64^2}{8}$$

$$= 287{,}290.13$$

Also, the classical equations for sum of squares for the main effects are given by:

$$SS_A = \frac{1}{bcn}\sum_{i=1}^{a}\sigma^2_{(ult)_i} - \frac{\sigma^2_{(ult)_{....}}}{abcn} \qquad 4\text{-}21$$

$$SS_T = \frac{1}{acn}\sum_{j=1}^{b}\sigma^2_{(ult)_j} - \frac{\sigma^2_{(ult)_{....}}}{abcn} \qquad 4\text{-}22$$

$$SS_C = \frac{1}{abn}\sum_{k=1}^{c}\sigma^2_{(ult)_k} - \frac{\sigma^2_{(ult)_{....}}}{abcn} \qquad 4\text{-}23$$

4.8 Regression Model and Response Surface for Ultimate Strength

The regression model for predicting the boundary conditions' influences on Ultimate Strength can be expressed as:

$$\sigma_{ult} = \beta_0 + \beta_1 x_1 + \beta_2 x_2 + \beta_3 x_3 + \beta_{12} x_1 x_2 + \beta_{13} x_1 x_3 + \beta_{23} x_2 x_3 + \beta_{123} x_1 x_2 x_3 \quad 4\text{-}29$$

where the coded variables x_1, x_2, and x_3 are defined on a scale from -1 to +1; the low and high levels of A, T, and C respectively. The x_1x_2, x_1x_3, x_2x_3, and $x_1x_2x_3$ terms are the AT, AC, TC, and ATC interactions respectively. And the β's are regression coefficients and are related to the effect estimates.

$$\beta_1 = \frac{1}{2}(Effect\ of\ Estimate\ A) \quad 4\text{-}30$$

$$\beta_1 = \frac{-41.986}{2} = -20.993$$

$$\beta_2 = \frac{1}{2}(Effect\ of\ Estimate\ T) \quad 4\text{-}31$$

$$\beta_2 = \frac{12.999}{2} = 6.500$$

$$\beta_3 = \frac{1}{2}(Effect\ of\ Estimate\ C) \quad 4\text{-}32$$

$$\beta_3 = \frac{-131.371}{2} = -65.686$$

$$\beta_{12} = \frac{1}{2}(Effect\ of\ Estimate\ AT) \quad 4\text{-}33$$

$$\beta_{12} = \frac{231.366}{2} = 115.683$$

$$\beta_{13} = \frac{1}{2}(Effect\ of\ Estimate\ AC) \qquad 4\text{-}34$$

$$\beta_{13} = \frac{195.266}{2} = 97.633$$

$$\beta_{23} = \frac{1}{2}(Effect\ of\ Estimate\ TC) \qquad 4\text{-}35$$

$$\beta_{23} = \frac{-180.189}{2} = -90.095$$

$$\beta_{123} = \frac{1}{2}(Effect\ of\ Estimate\ ATC) \qquad 4\text{-}36$$

$$\beta_{123} = \frac{17.944}{2} = 8.972$$

And β_0 is the estimated average of all eight responses, hence

$$\beta_0 = \frac{1}{8}[1508.72 + 1106.13 + 1426.6 + 1522.63 + 1607.07 + 1630.9 + 1200.46 + 1651.134] = 1456.706$$

The relationship between the natural variables; agitation, temperature, and current density, and the coded variables is:

$$X_1 = \frac{A - (A_{Low} + A_{High})/2}{(A_{High} - A_{Low})/2} \qquad 4\text{-}37a$$

$$X_1 = \frac{A - 150}{150} \qquad 4\text{-}37b$$

$$X_2 = \frac{T - (T_{Low} + T_{High})/2}{(T_{High} - T_{Low})/2} \qquad 4\text{-}38a$$

$$X_2 = \frac{T - 37.5}{12.5} \qquad 4\text{-}38b$$

$$X_3 = \frac{C - \left(C_{Low} + C_{High}\right)/2}{\left(C_{High} - C_{Low}\right)/2} \qquad 4\text{-}39a$$

$$X_3 = \frac{C - 7.50}{2.50} \qquad 4\text{-}39b$$

As a result, the regression model—coded values—for $\sigma_{(ult)}$ is given by:

$$\sigma_{ult} = 1456.706 - 20.993x_1 + 6.500x_2 - 65.686x_3 + 115.683x_1x_2 + 97.633x_1x_3 - 90.095x_2x_3 + 8.972x_1x_2x_3 \qquad 4\text{-}42$$

The regression model—in actual physical values—is given by:

$$\sigma_{ult} \approx 1484.354 - 4.4063A + 12.888T + 42.786C + 0.0617AT + 0.2604AC - 2.883TC \qquad 4\text{-}43$$

4.9 Ultimate Strength's Plots as a Function of the Boundary Conditions

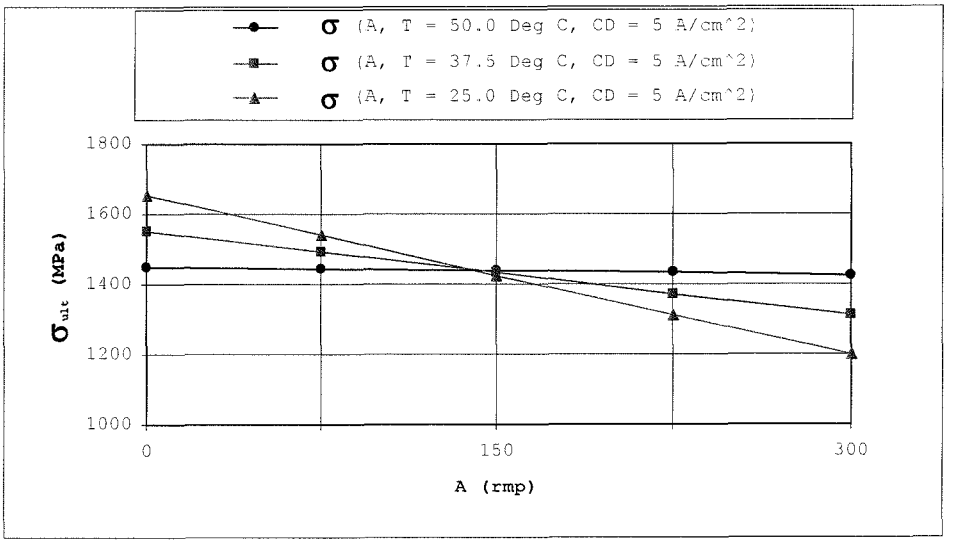

Figure 4-55: Ultimate Strength with varying agitation (A) and temperature (T); and constant current density (C = 5.0 A/cm^2).

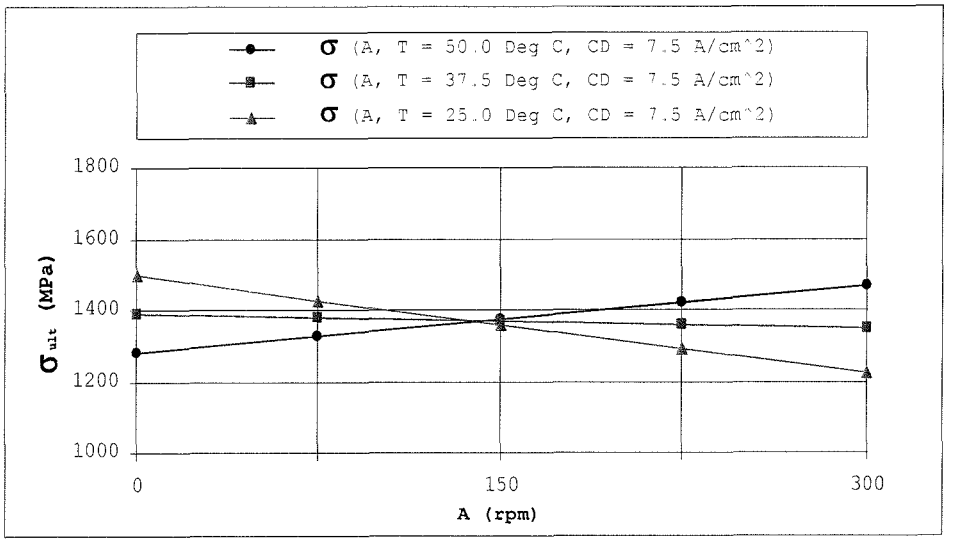

Figure 4-56: Ultimate Strength with varying agitation (A) and temperature (T); and constant current density (C = 7.5 A/cm^2).

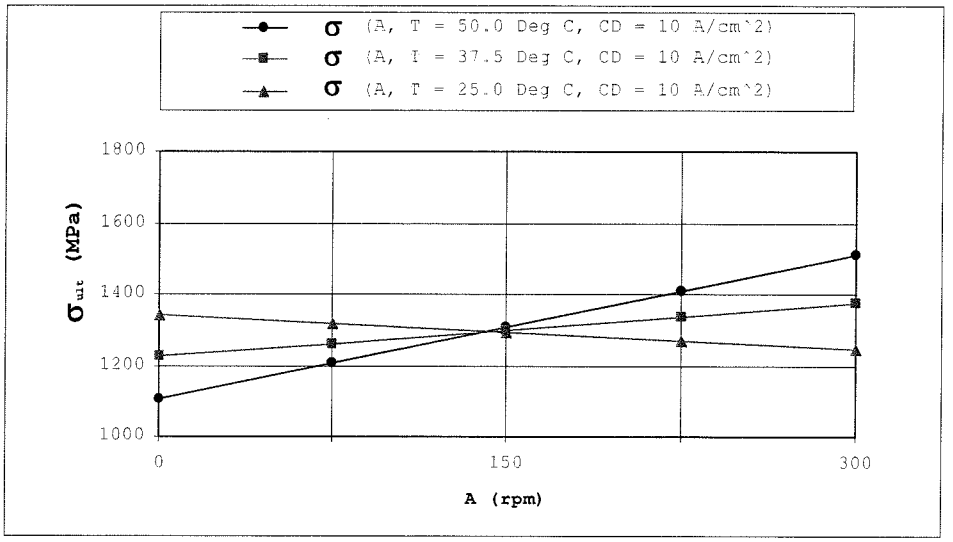

Figure 4-57: Ultimate Strength with varying agitation (A) and temperature (T); and constant current density (C = 10.0 A/cm^2).

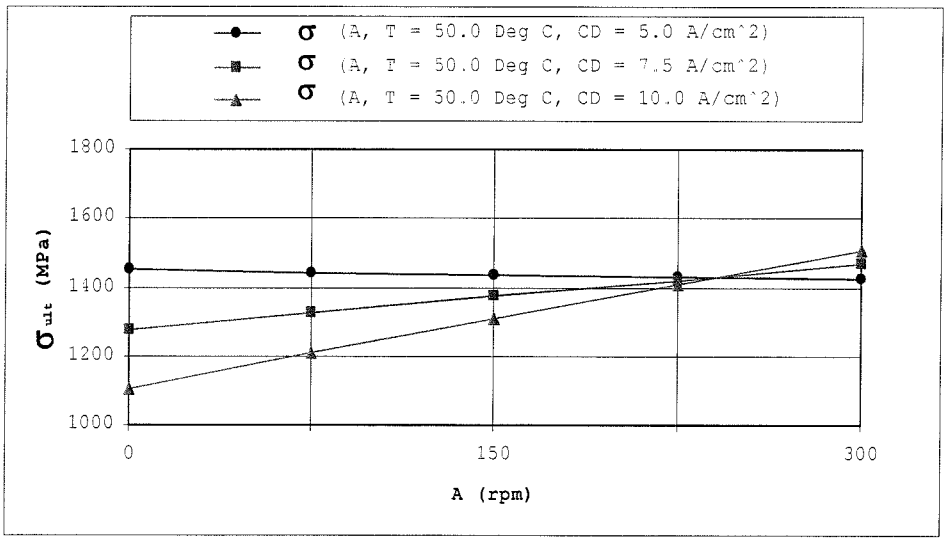

Figure 4-58: Ultimate Strength with varying agitation (A) and current density (C); and constant temperature (T = 50.0 Deg C).

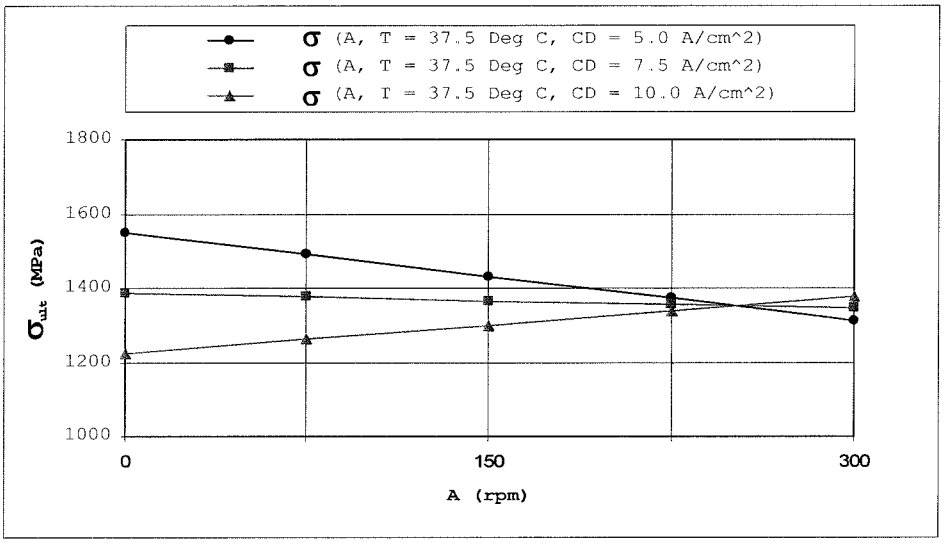

Figure 4-59: Ultimate Strength with varying agitation (A) and current density (C); and constant temperature (T = 37.5 Deg C).

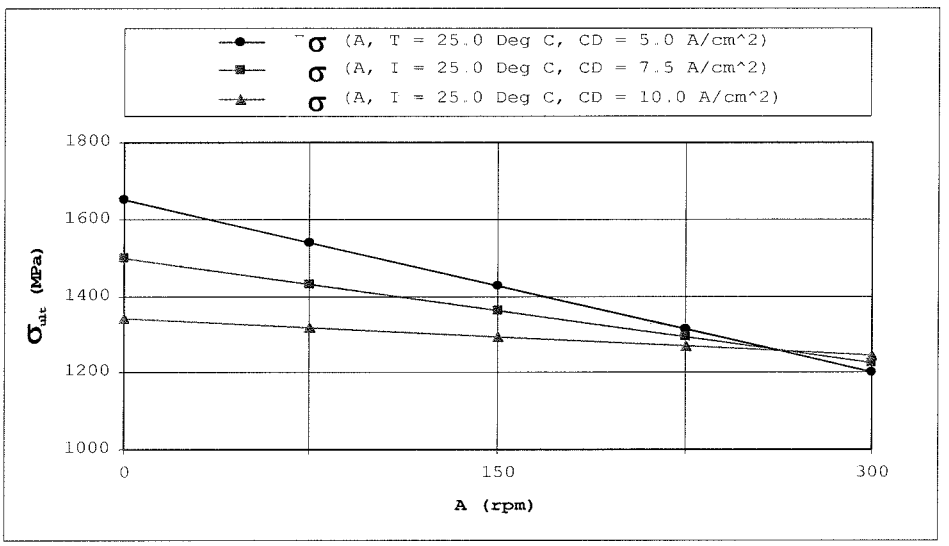

Figure 4-60: Ultimate Strength with varying agitation (A) and current density (C); and constant temperature (T = 25.0 Deg C).

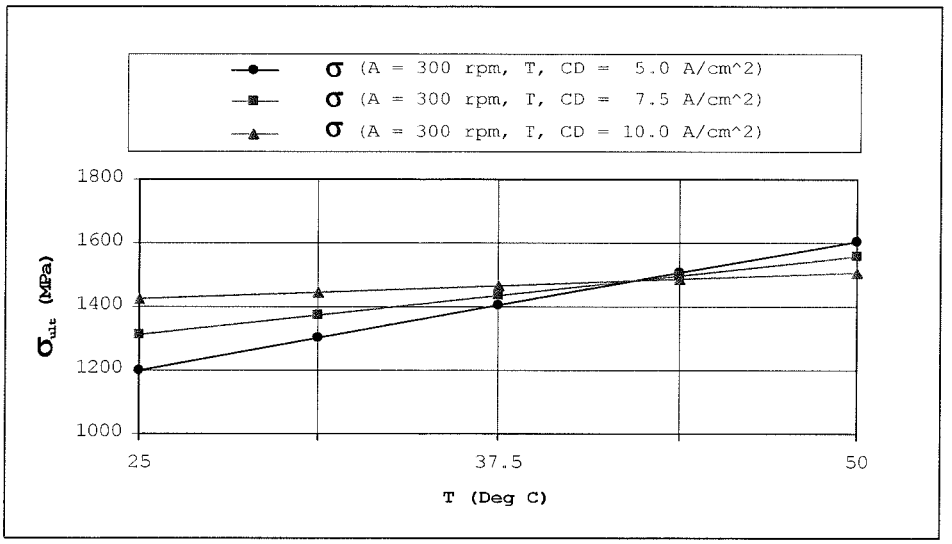

Figure 4-61: Ultimate Strength with varying temperature (T) and current density (C); and constant agitation (A = 300 rpm).

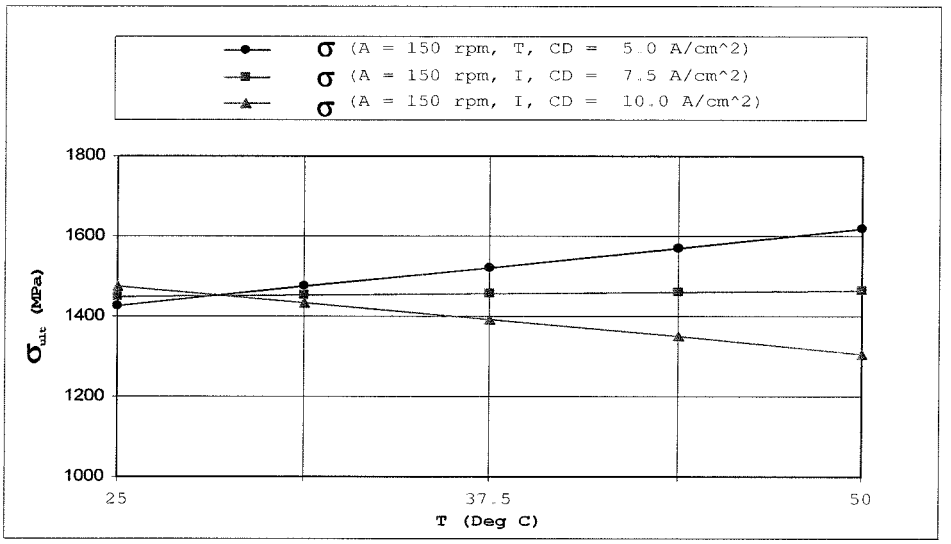

Figure 4-62: Ultimate Strength with varying temperature (T) and current density (C); and constant agitation (A = 150 rpm).

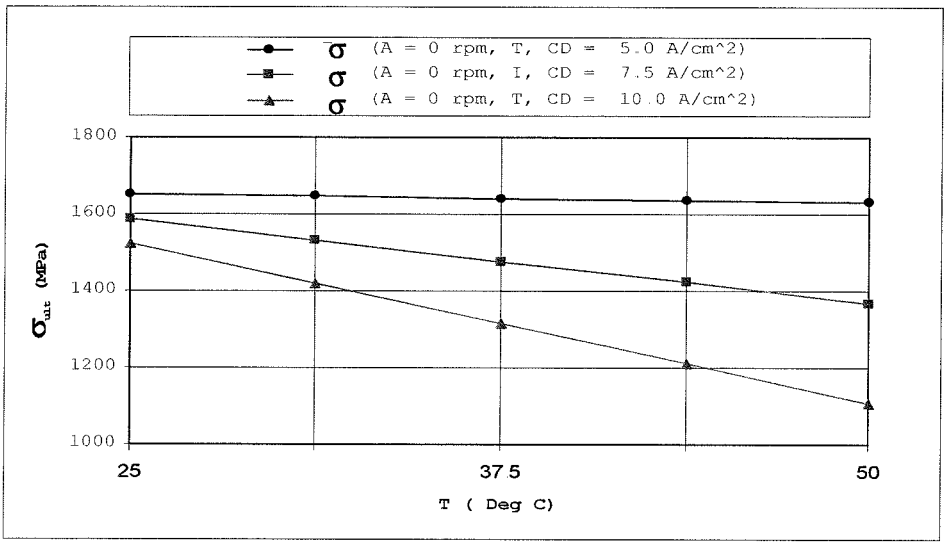

Figure 4-63: Ultimate Strength with varying temperature (T) and current density (C); and constant agitation (A = 0 rpm).

4.10 Results Ultimate Stress: Design-Expert Software

ANOVA for selected factorial model

Analysis of variance table [Partial sum of squares - Type III]

Source	Sum of Squares	df	Mean Square	F Value	p-value Prob > F
Model2.866E+005	6	47772.42	74.18	*0.0886*	not significant
A-Agitation	*3525.65*	*1*	*3525.65*	*5.47*	*0.2571*
B-Temperature	*337.95*	*1*	*337.95*	*0.52*	*0.6009*
C-Current Density	*34516.68*	*1*	*34516.68*	*53.60*	*0.0864*
AB	*1.071E+005*	*1*	*1.071E+005*	*166.25*	*0.0493*
AC	*76257.62*	*1*	*76257.62*	*118.42*	*0.0583*
BC	*64936.15*	*1*	*64936.15*	*100.84*	*0.0632*
Residual	643.97	1	643.97		
Cor Total			2.873E+005		7

The Model F-value of 74.18 implies there is a 8.86% chance that a "Model F-Value" this large could occur due to noise.

Values of "Prob > F" less than 0.0500 indicate model terms are significant.

In this case AB are significant model terms. Values greater than 0.1000 indicate the model terms are not significant. If there are many insignificant model terms (not counting those required to support hierarchy), model reduction may improve your model.

Std. Dev.	25.38	R-Squared	0.9978
Mean	1456.71	Adj R-Squared	0.9843
C.V. %	1.74	Pred R-Squared	0.8565
PRESS	41214.35	Adeq Precision	22.959

The "Pred R-Squared" of 0.8565 is in reasonable agreement with the "Adj R-Squared" of 0.9843.

"Adeq Precision" measures the signal to noise ratio. A ratio greater than 4 is desirable. Your ratio of 22.959 indicates an adequate signal. This model can be used to navigate the design space.

Coefficient Factor	Standard Estimate	df	Error	95% CI Low	95% CI High	VIF
Intercept	1456.71	1	8.97	1342.71	1570.71	
A-Agitation	-20.99	1	8.97	-134.99	93.01	1.00
B-Temperature	6.5	1	8.97	-107.50	120.50	1.00
C-Current Density	-65.69	1	8.97	-179.69	48.31	1.00
AB	115.68	1	8.97	1.68	229.68	1.00
AC	97.63	1	8.97	-16.37	211.63	1.00
BC	-90.09	1	8.97	-204.09	23.91	1.00

Final Equation in Terms of Coded Factors:

Ultimate Stress (σ_{ult}) = +1456.71 - 20.99 * A + 6.50 * B - 65.69 * C

+ 115.68 * A * B + 97.63 * A * C

- 90.09 * B * C

Final Equation in Terms of Actual Factors:

Ultimate Stress (σ_{ult}) = +1484.35400 - 4.40627 * Agitation +12.88800 * Temperature

+ 42.78600 * Current Density

+ 0.061698 * Agitation * Temperature

+ 0.26035 * Agitation * Current Density

- 2.88302 * Temperature * Current Density

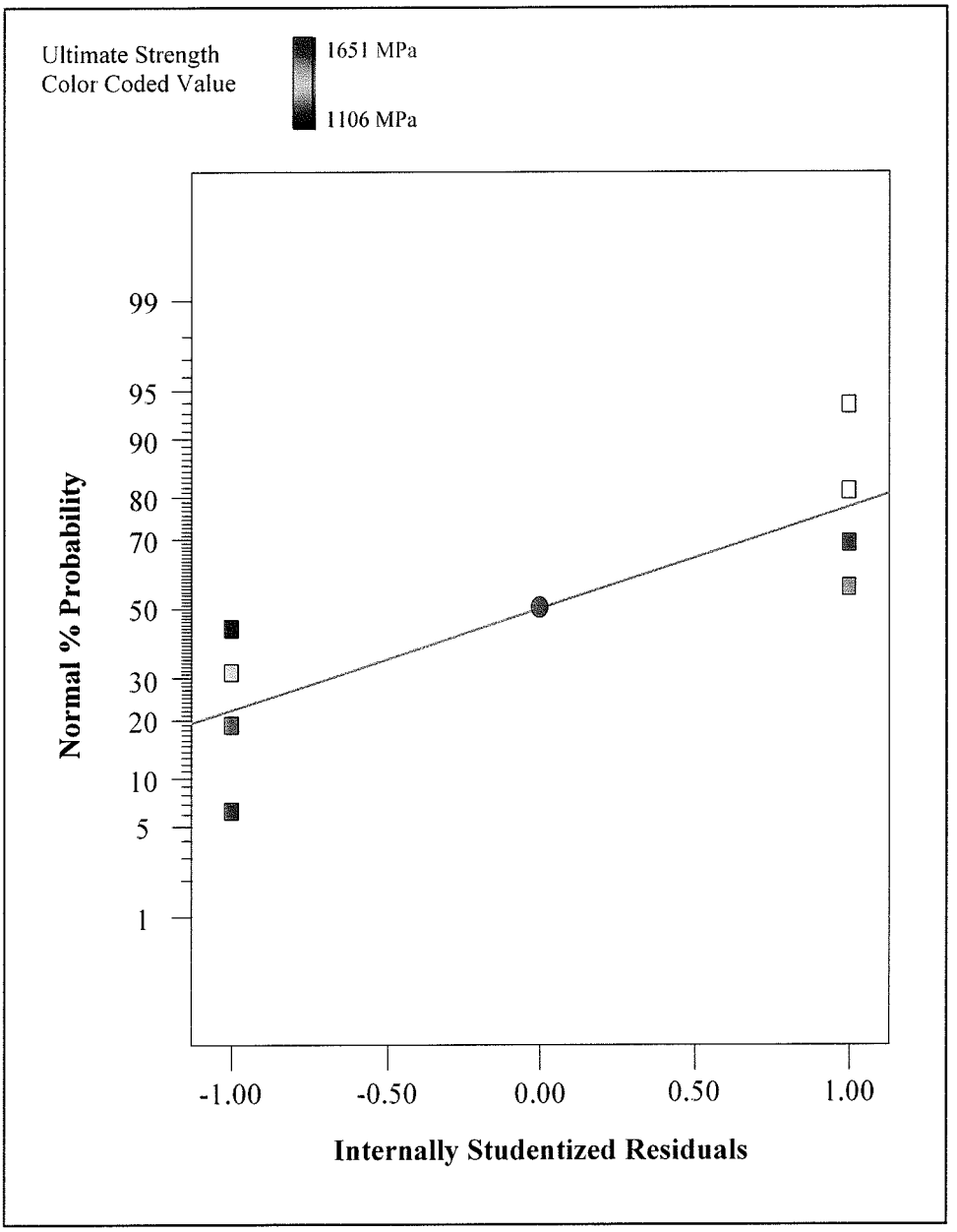

Figure 4-64: Normal Probability Plot of Residuals for Ultimate Strength.

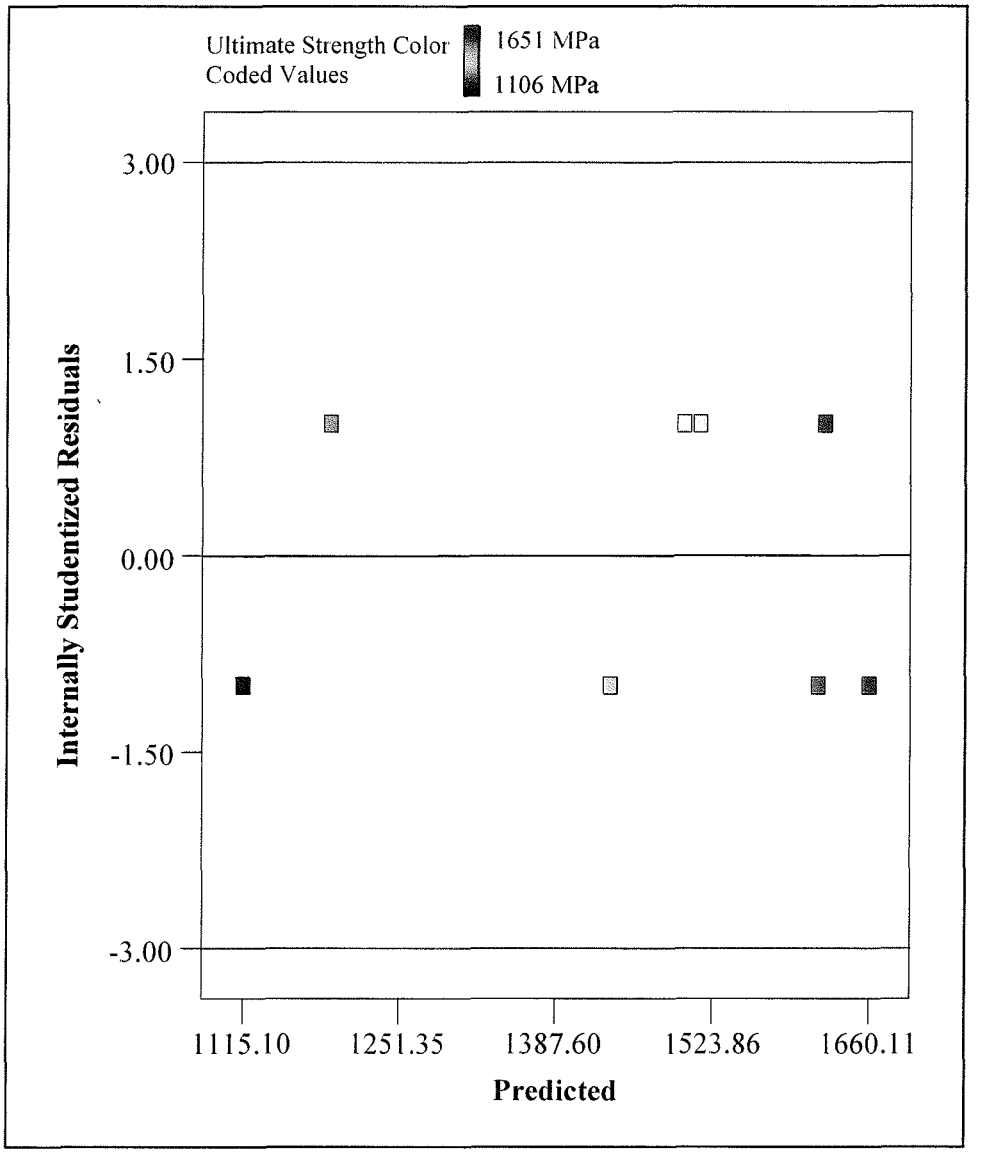

Figure 4-65: Plot of Residual vs. Predicted for Ultimate Strength.

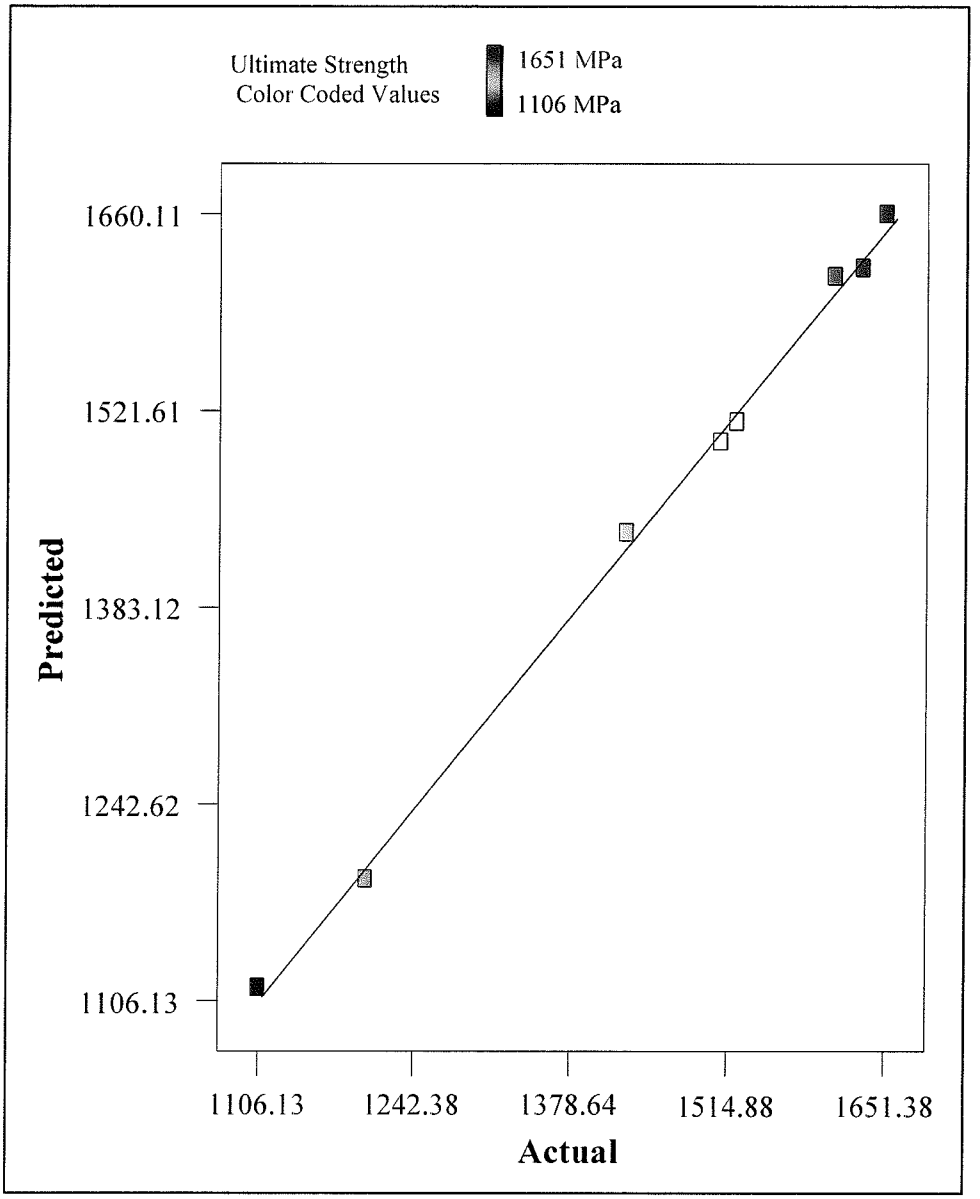

Figure 4-66: Predicted vs. Actual Value Plot for Ultimate Strength.

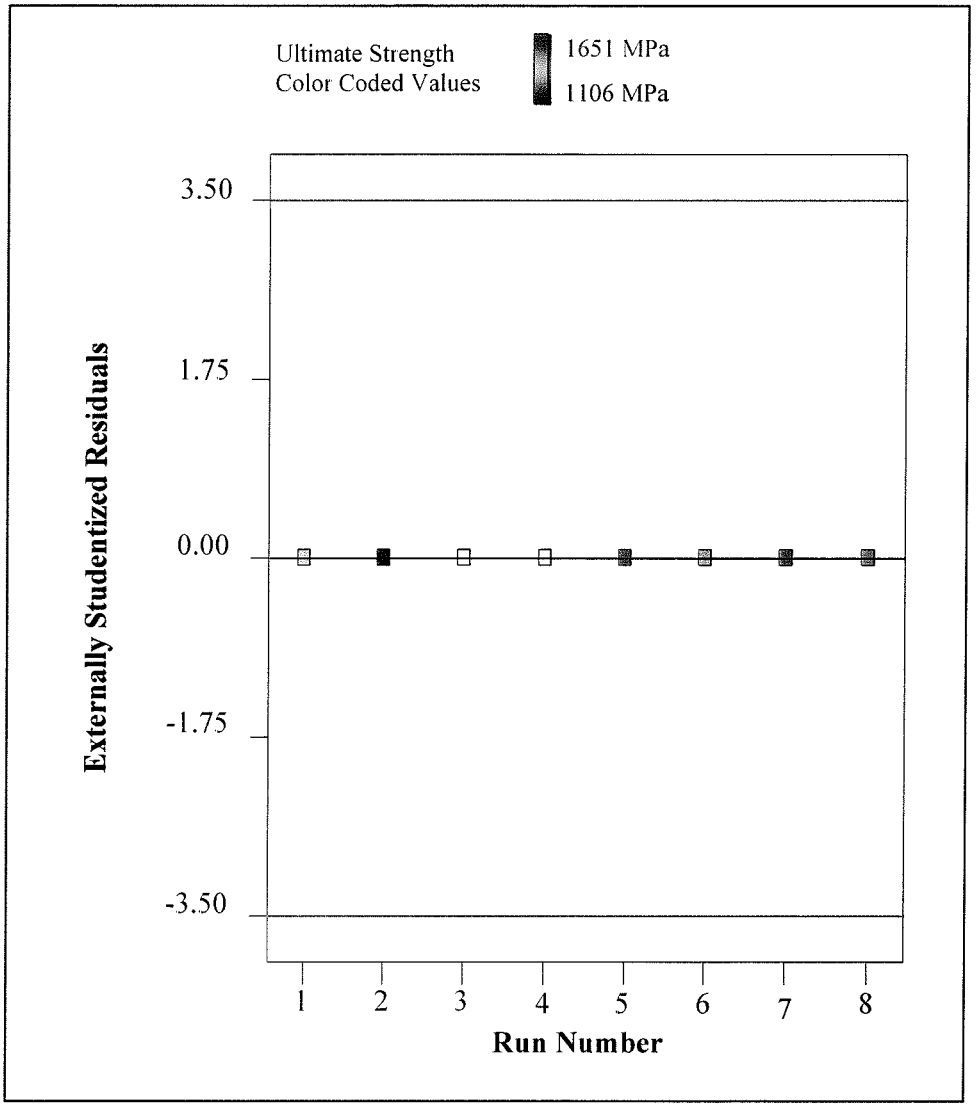

Figure 4-67: External Studentized Residual Plot for Ultimate Strength.

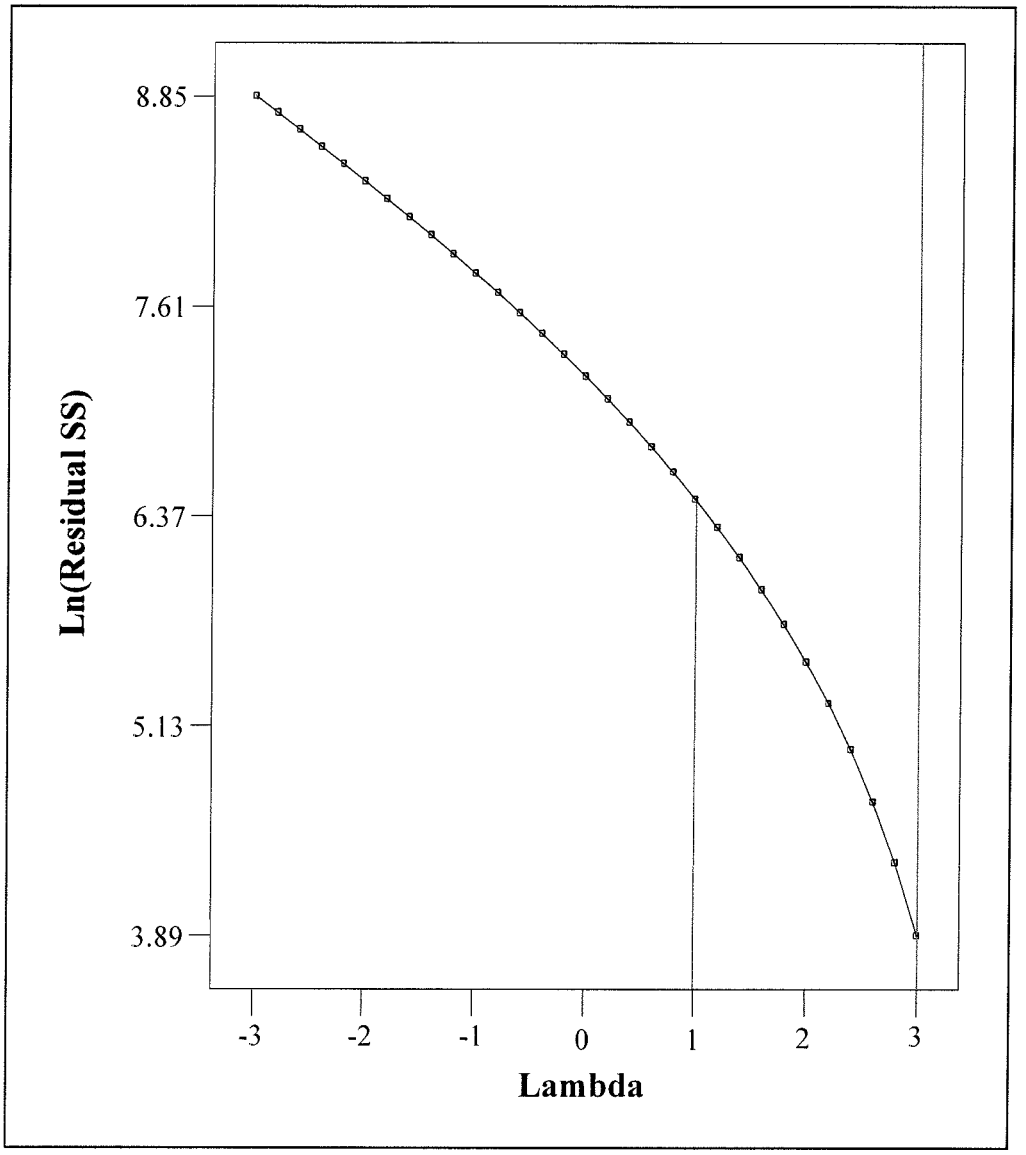

Figure 4-68: Box-Cox Plot for Power Transforms—Ultimate Strength.

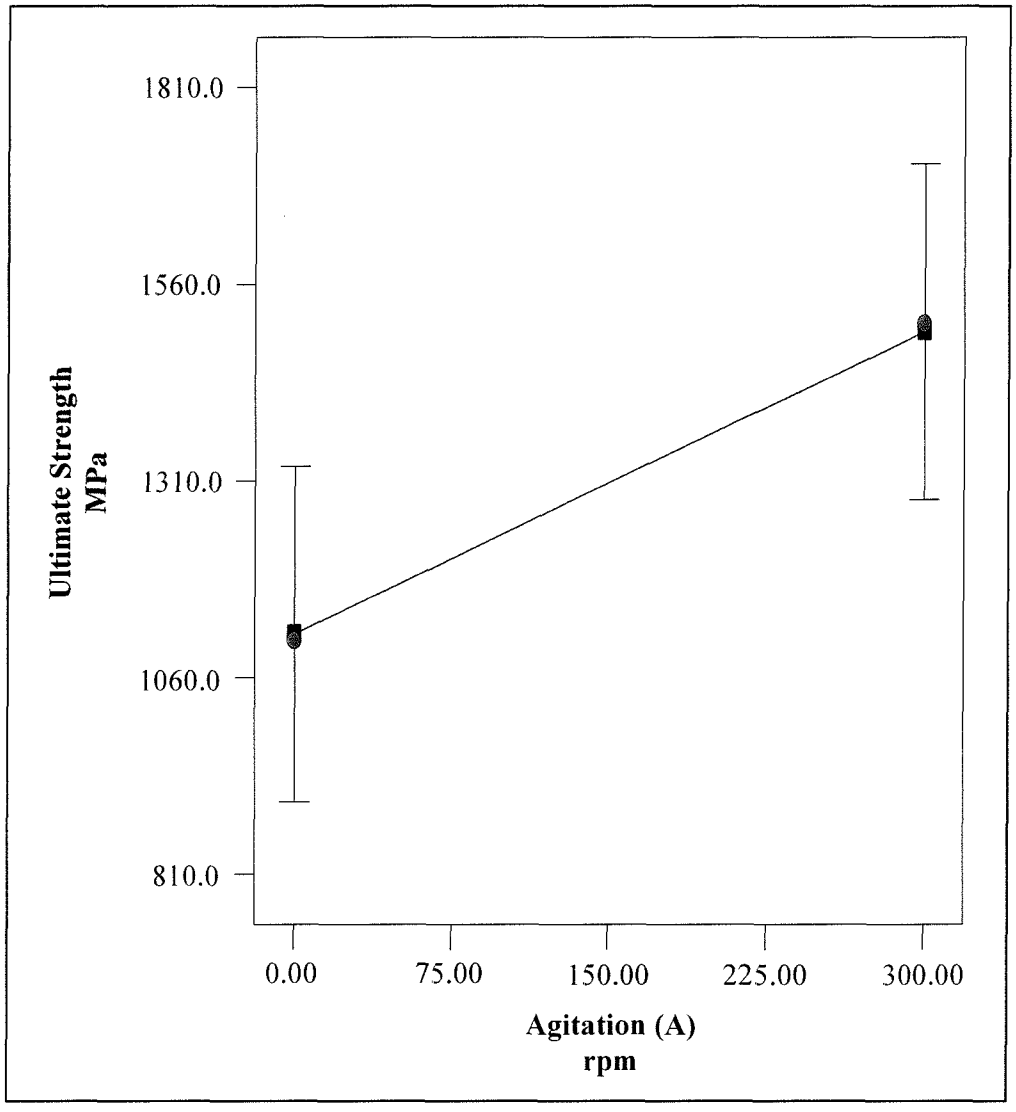

Figure 4-69: One Factor Plot of Ultimate Strength Plot as a function of agitation. Temperature and current density are fixed at 50.0 Deg C and 10.0 A/cm^2 respectively.

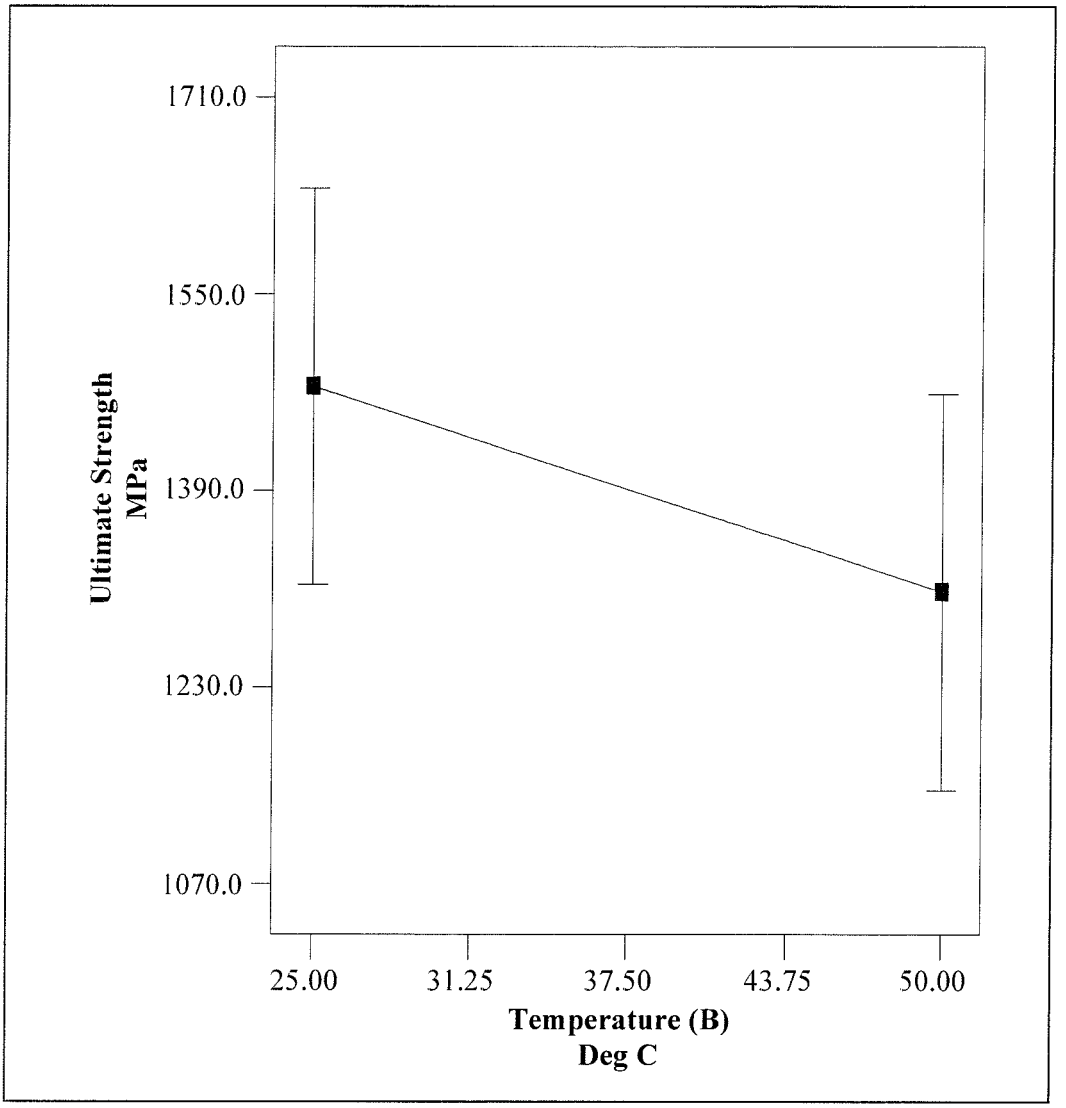

Figure 4-70: One Factor Plot of Ultimate Strength as a function of temperature. Agitation and current density are fixed at 150 rpm and 10.0 A/cm^2 respectively.

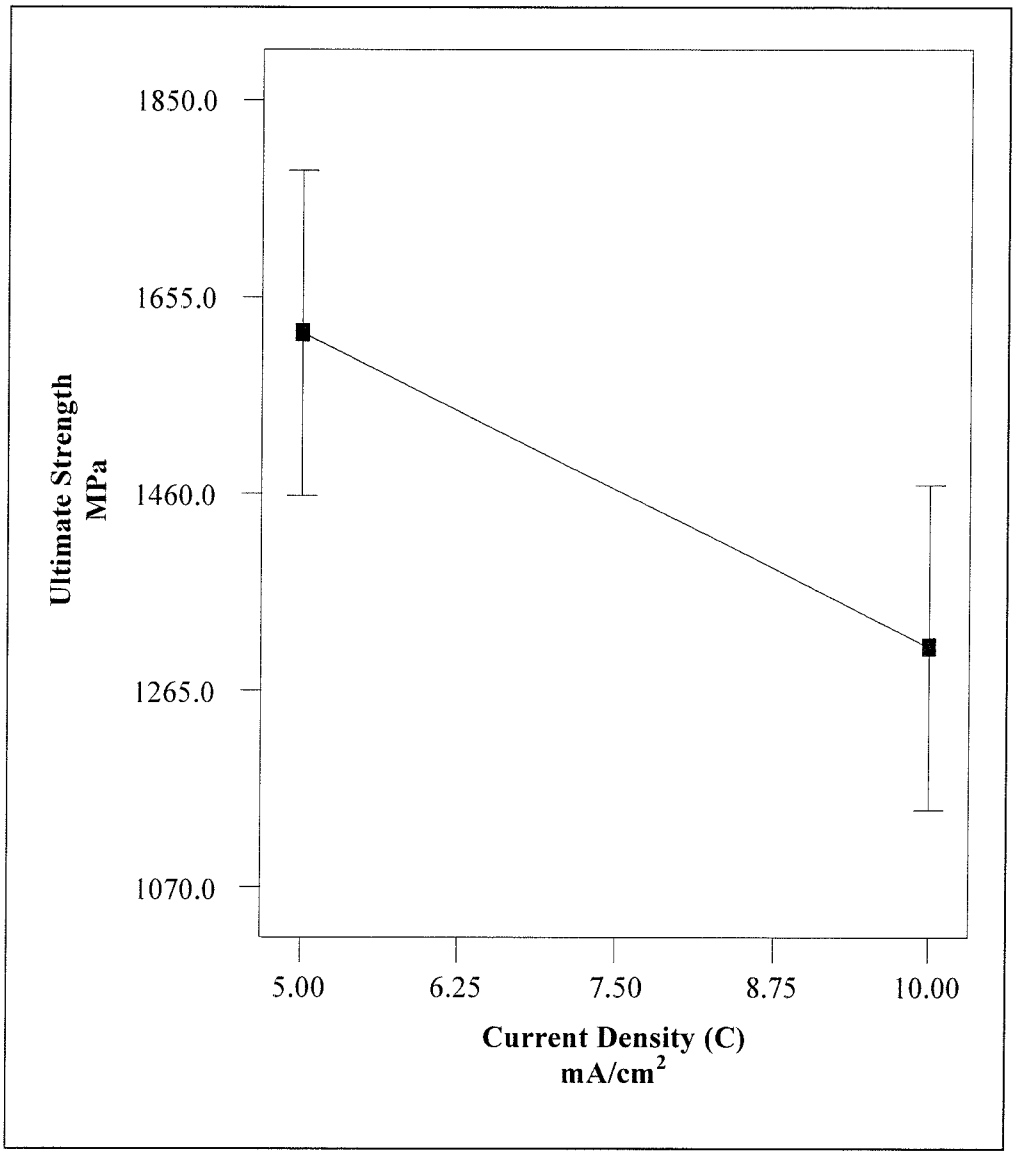

Figure 4-71: One-Factor Plot of Ultimate Strength current density. Temperature and agitation are fixed at 50.0 Deg C and 150 rpm respectively.

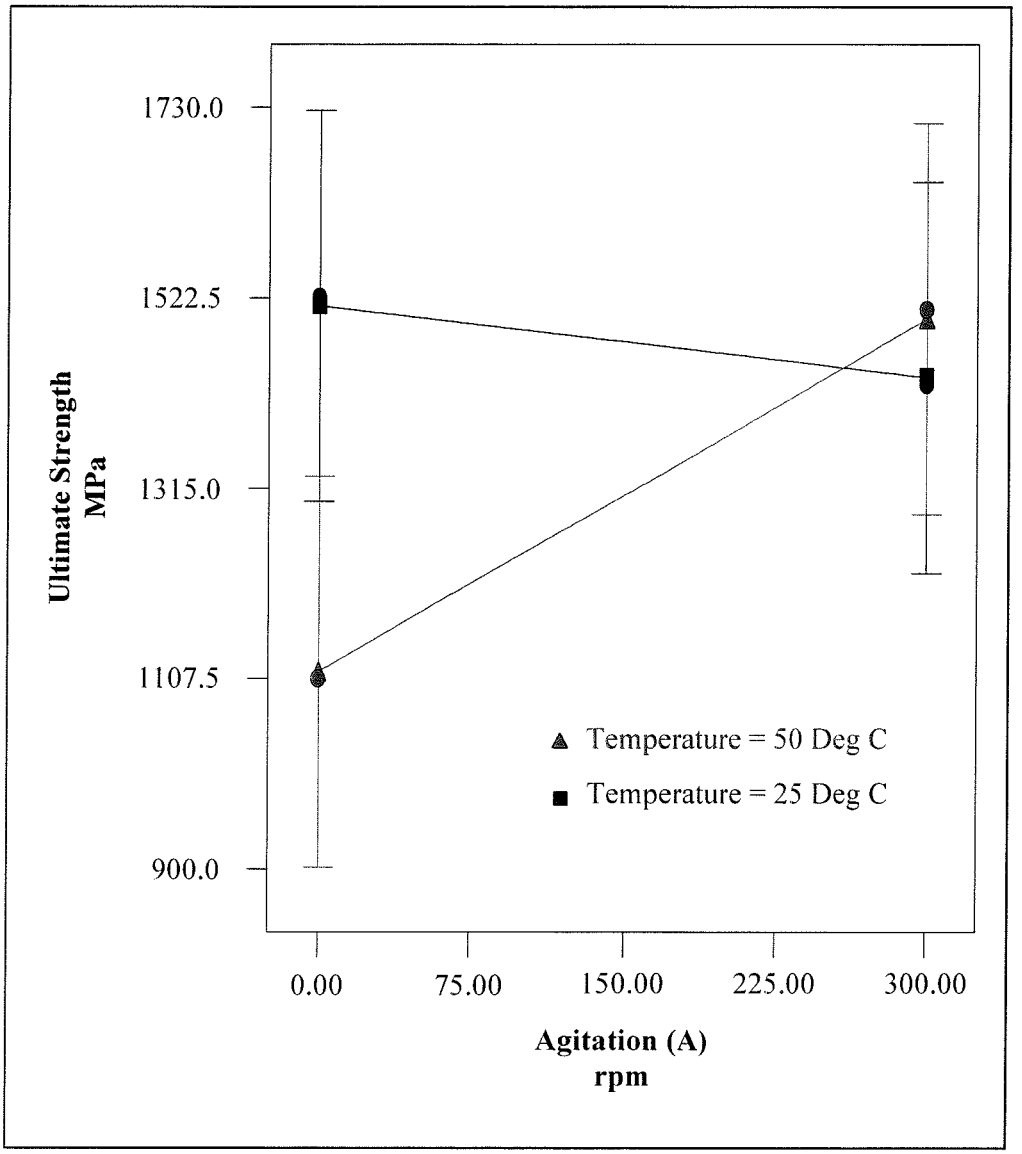

Figure 4-72: Two-Factors Interaction Plot of Ultimate Strength Plot as a function of agitation and temperature. Current density is fixed at 10.0 A/cm^2.

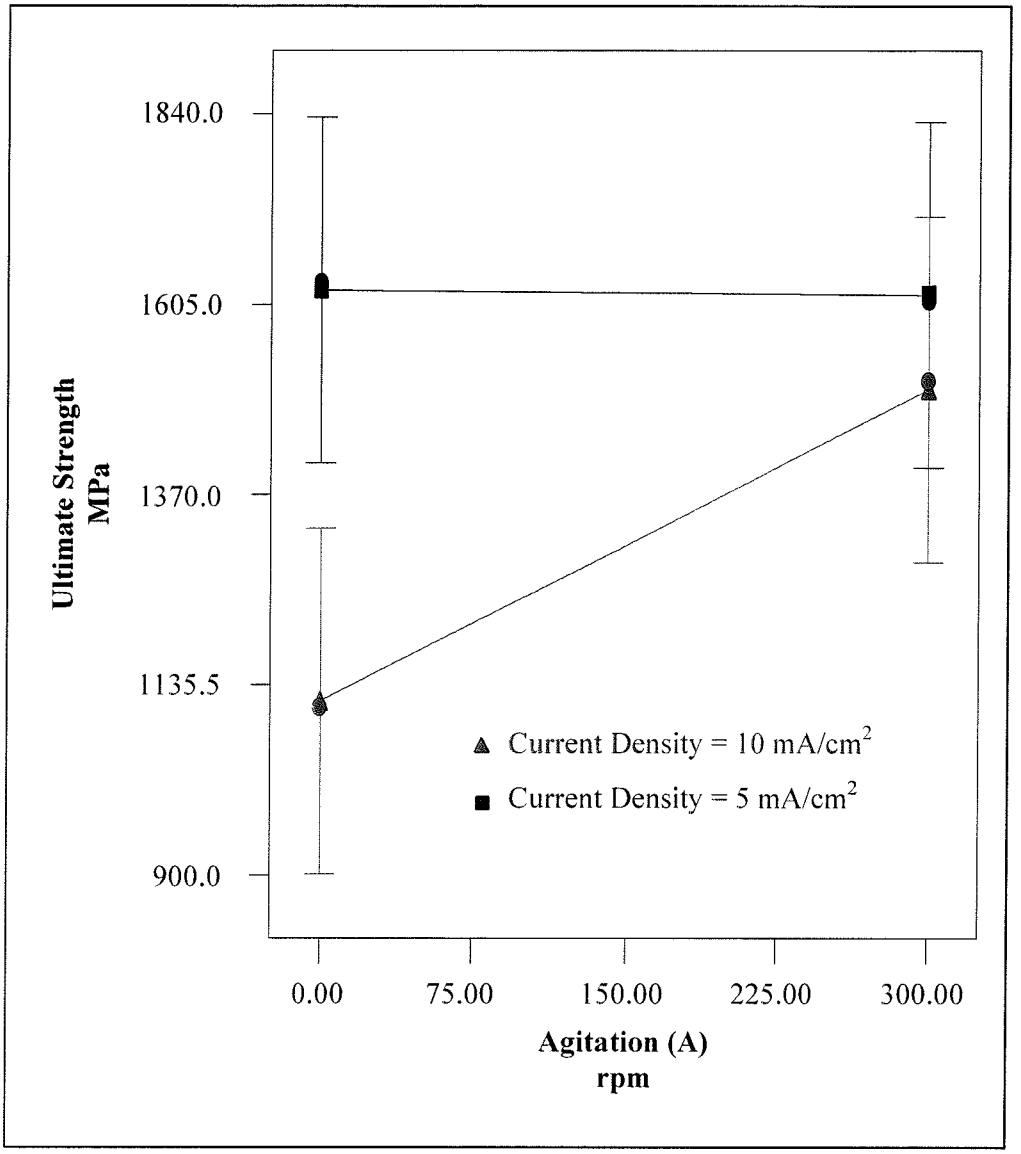

Figure 4-73: Two-Factors Interaction Plot of Ultimate Strength Plot as a function agitation and current density. Temperature is fixed at 50 Deg C.

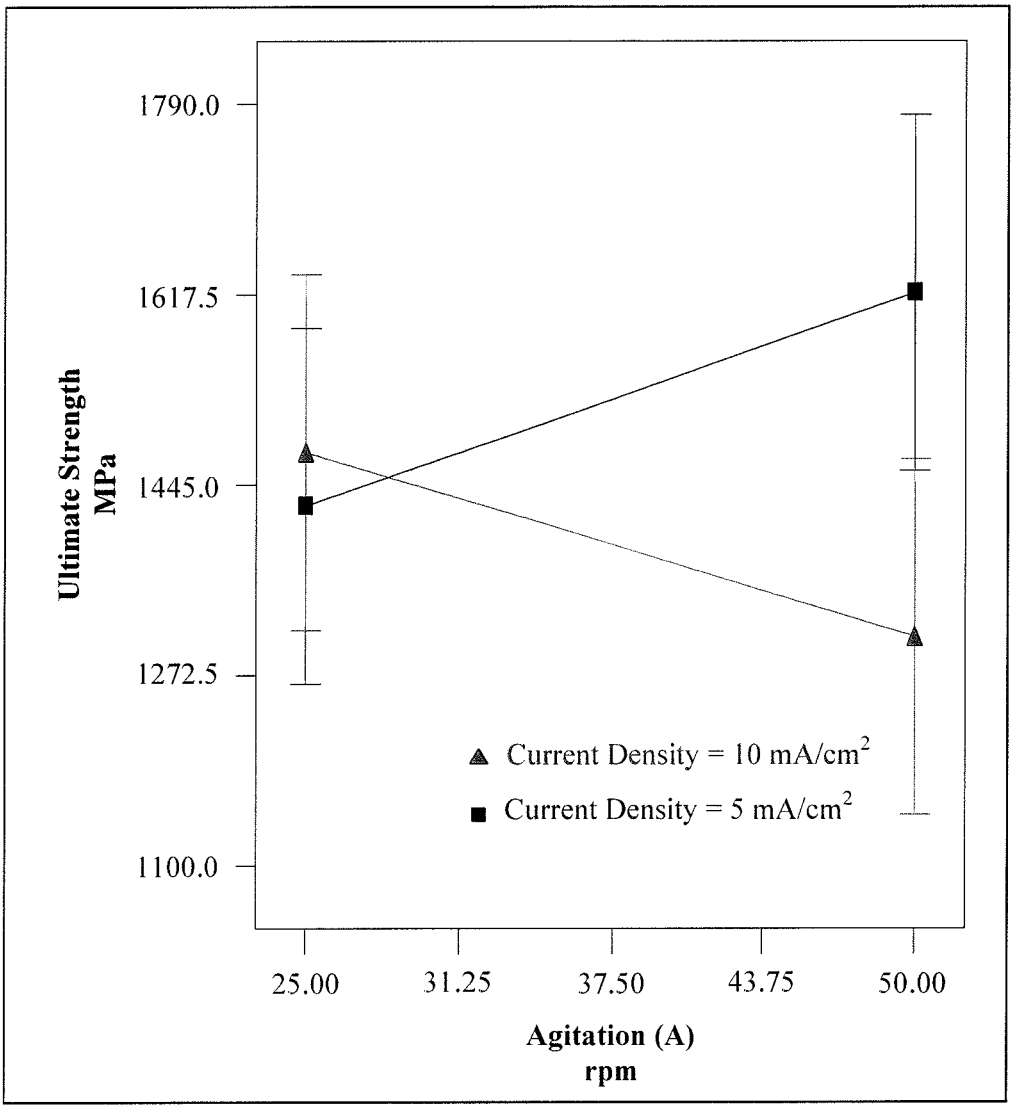

Figure 4-74: Two-Factors Interaction Plot of Ultimate Strength as a function of current density and temperature. Agitation is fixed at 150 rpm.

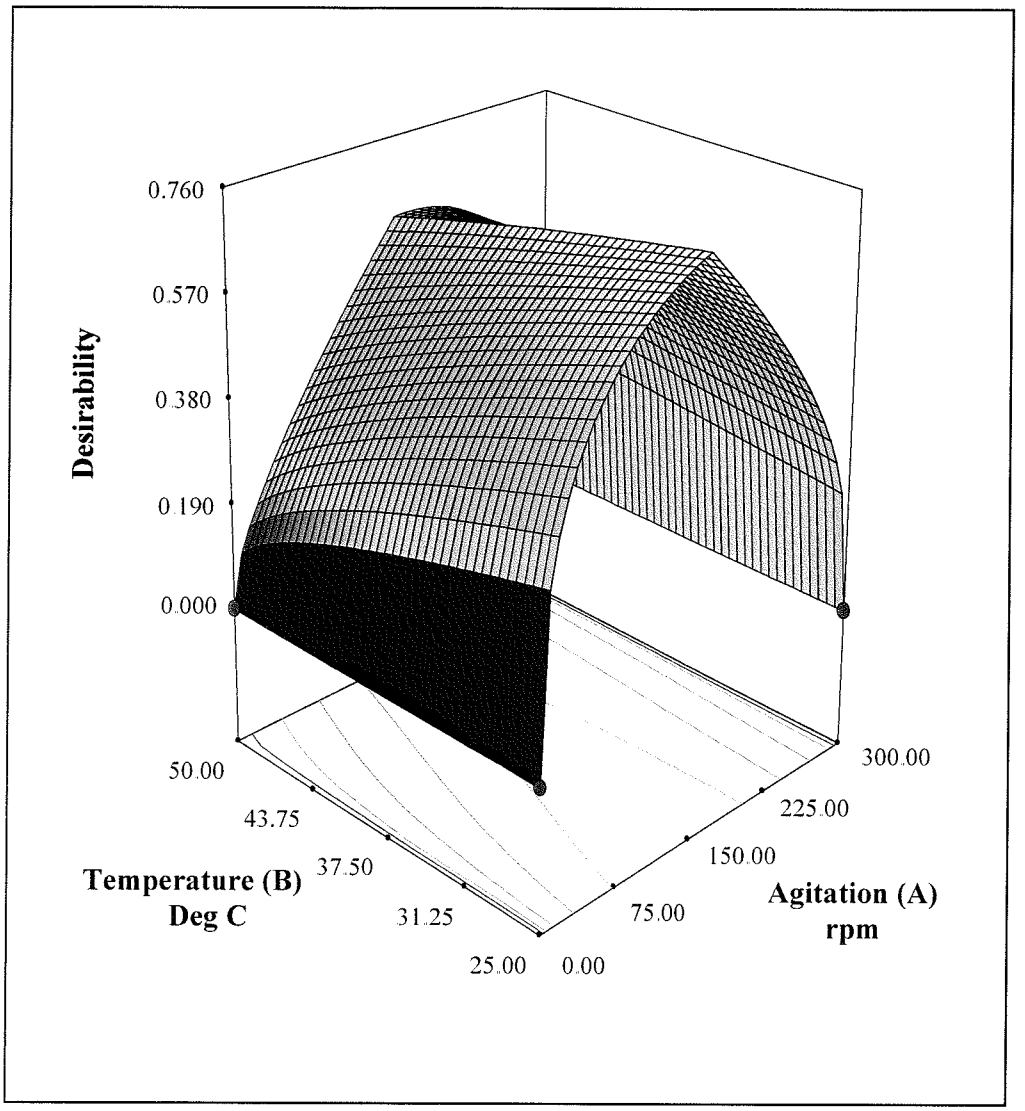

Figure 4-75: 3D Surface Desirability Plot of Ultimate Strength as a function of agitation and temperature. Current density is fixed at 10.0 A/cm^2.

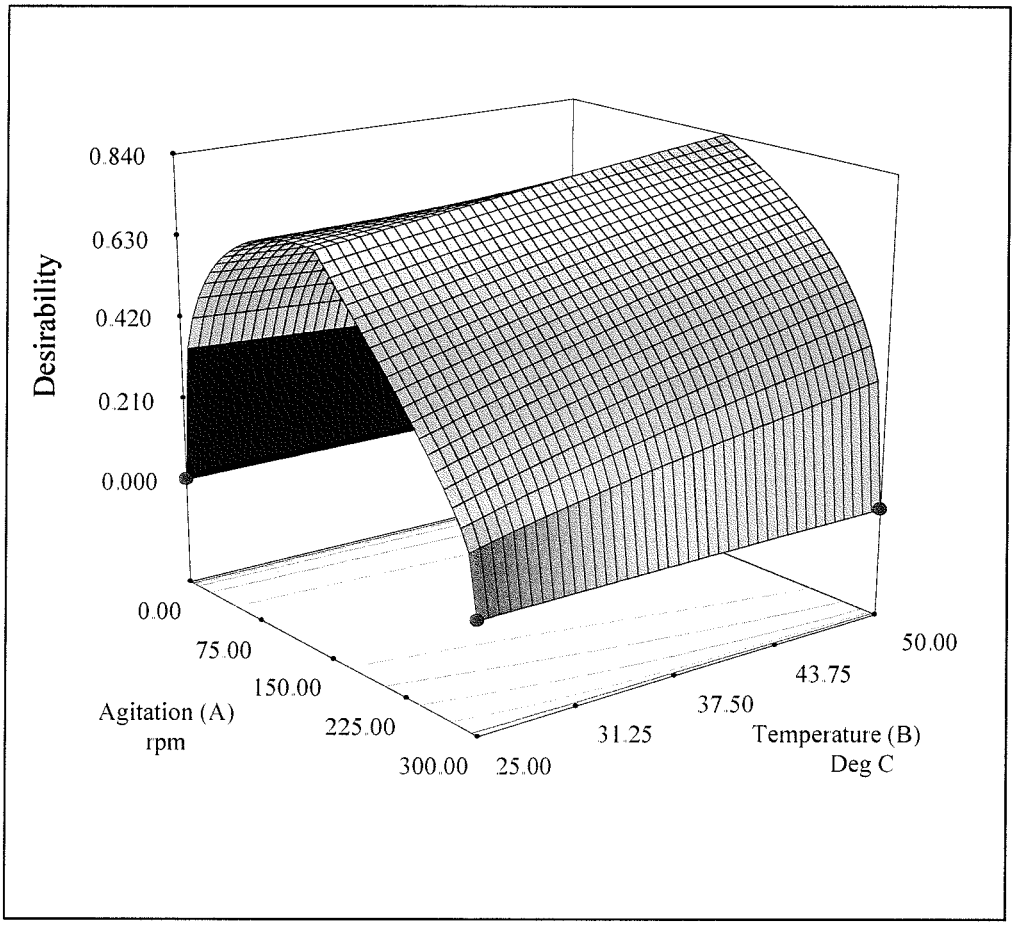

Figure 4-76: 3D Surface Desirability Plot of Ultimate Strength as a function of agitation and temperature. Current density is fixed at 5.0 A/cm^2.

4.11 References

[1] Y. Xue, D. R. Veazie, and K. Hillman, "*Thermal-Mechanical Evaluation of Plated Electro-Magnetic NiFe for MEMS Generators*", *Proceedings of the Fall Meeting of the Materials Research Society (MRS), December 1 – 5, 2003 Boston, MA.*

[2] S. D. Leith, S. Ramli, and D. T. Schwartz, "*Characterization of NixFe1-x (0.10 < x < 0.95) Electrodeposition from a Family of Sulfamate-Chloride Electrolytes*", *Journal of Electrochemical Society,* ***146*** *(4), pp. 1431-1435 (1999)*

[3] S. D. Leith, S. Ramli, and D. T. Schwartz, "*Characterization of NixFe1-x (0.10 < x < 0.95) Electrodeposition from a Family of Sulfamate-Chloride Electrolytes*", *Journal of Electrochemical Society,* ***146*** *(4), pp. 1431-1435 (1999)*

[4] H. Huang, D. R. Veazie, and D. Ephraim, "*In-Situ Tensile Test of NiFe Thin Films Using AFM-Based Micro/Nano-Scale Mechanical Testing System (AFM-MTS)*", *Proceedings of the 22nd Southeastern Conference on Theoretical and Applied Mechanics (SECTAM-XXII), August 15 – 17, 2004, Tuskegee AL.*

CHAPTER 5

DISCUSSION AND CONCLUSION

In Chapter 1, Introduction, background information was discussed concerning new developments and ongoing research in the area of power MEMS. Because of these new developments; materials (thin-film materials), whose applications in the past, required limited to no structural application, are now being used as structural components and devices. As a result, material characterizations and mechanical properties are vital design. This research focused on the material—electrodeposited $Ni_{80}Fe_{20}$. In particular, this research focused on how the electrolytes' boundary conditions influence the mechanical properties of electrodeposited $Ni_{80}Fe_{20}$. The processes used for achieving the objectives were as follows:

1) Design a 2^k Factorial Analysis and Design of Experiments for the critical electrolyte boundary conditions which affect the mechanical properties of electrodeposited $Ni_{80}Fe_{20}$.
2) Conduct Regression Analyses to model the mechanical properties as a function of the critical electrolytes' boundary conditions.
3) Fabricate electrodeposited $Ni_{80}Fe_{20}$ test specimens for mechanical, magnetic, and composition testing.
4) Conduct experiments of test specimens to validate regression analysis models.

In Chapter 2, Literature Review, an investigation was conducted to determine critical variables that influence the mechanical properties of electrodeposited $Ni_{80}Fe_{20}$. Three critical variables were chosen: agitation of the electrolytes' solution; temperature of the electrolytes' solution; and the imposed current density.

In Chapter 3, Experimental Procedures, test specimens were fabricated and tested. Initially, the test specimens were used to identify the boundary conditions for the three critical variables chosen in Chapter 2. And lastly, the test specimens were used to describe the mechanical properties of $Ni_{80}Fe_{20}$ as a function of the critical values.

In Chapter 4; Statistical Analysis, a design of experiment (DOE) was established. Using 2^3 Factorial Design Analysis, a test matrix was established. The mechanical properties—Young Modulus and Ultimate Stress—were modeled as a function of the three critical values at two boundary conditions—lower bound and upper bound.

In Chapter 5, Discussion and Conclusion, the findings obtained in Chapter 4 will be analyzed and discussed. In addition, SEM surface grain pictures, and electrodeposition uniformity will be discussed.